DLR-IB-AE-GO-2026-72

DLR-IB-AE-GO-2026-72

Numerical Investigation of
Transonic Stall
Flutter Mechanisms of a NACA
3506 Rotor
(Masterarbeit)

Florian Resech
Institut für Aeroelastik

DLR

GEORG-AUGUST-UNIVERSITÄT
GÖTTINGEN

DLR

Master's Thesis

Numerical Investigation of Transonic Stall Flutter Mechanisms of a NACA 3506 Rotor

Numerische Untersuchung der transsonischen Abreiß-Flatter Mechanismen eines NACA 3506 Rotors

prepared by

Florian Resech

from Lüneburg

at the DLR Göttingen - Institute for Aeroelasticity

Thesis registered:	12th September 2025
Thesis submitted:	12th March 2026
Adviser:	Christoph Reiber
First Referee:	Dr.-Ing. Virginie Chenaux
Second Referee:	Prof. Dr. rer. nat. Dr. habil. Andreas Dillmann

Abstract

To improve jet engine efficiency, the loading of fans and compressors increases with every design iteration, while structural damping mostly decreases due to weight savings. This leads to an increased susceptibility to aeroelastic phenomena such as flutter, making flutter stability analysis more and more important during the early design phase. An improved understanding of the physical mechanisms causing flutter onset can help accelerate the development of more efficient and safe jet engines.

Within this thesis, flutter stability of a two-dimensional NACA3506 annular compressor cascade is analyzed. Unsteady simulations over the entire working range of the compressor were performed, employing a prescribed motion approach to enforce blade oscillations. Flutter onset was determined using the Energy Method. The Favre-averaged Navier-Stokes equations were solved using a linearized and a non-linear Harmonic Balance solver, implemented in the DLR TRACE code. Flutter stability was evaluated on the entire compressor map. Operating points in a transonic flow regime near stall were selected, to investigate the physical mechanisms causing flutter onset in this flow regime for the first bending and torsion mode.

On the suction side, the shock at the suction peak and its interaction with the boundary layer was identified as a key mechanism causing transonic stall flutter in both the bending and torsion mode. Flutter onset occurs only at operating points, where shock induced boundary layer separation and reattachment appears. The shock leads to an increased phase shift, that is locally excites the oscillation. While it is not the only mechanism increasing flutter instability, it is the common denominator between all investigated operating conditions that exhibit flutter instability.

Acknowledgments

The presented master's thesis results from my time in the turbomachinery group at the Institute of Aeroelasticity of the German Aerospace Center (DLR) in Göttingen. I would like to thank Dr.-Ing. Virginie Chenaux for this great opportunity and the guidance of my work. I am grateful for the thorough theoretical discussions, thoughtful feedback and continuous motivation by my supervisor Christoph Reiber. I would also like to thank Dr.-Ing. Joachim Belz and Patrick Hübert for our interesting discussions. Special thanks to Dr.-Ing. Mathias Schuff and Dr.-Ing. Michael Müller for their support with all my problems regarding TRACE. Also, I would like to thank all the people at the institute for the warm welcome and the nice working environment, especially the lunch group and the other interns.

At this point, I would like to express my thanks for all the people who shaped my academic career till now. I would especially like to thank Prof. Martin Rein and Prof. Andreas Dillmann for their most interesting lectures about fluid dynamics and aerodynamics as well as Dr.-Ing. Keith Weinman, who supervised my bachelor's thesis and introduced me into the world of computational fluid dynamics.

Lastly, I want to express my heartfelt thanks to my family and friends who always supported me in my somewhat long journey to graduation. When motivation ran low, time with you always recharged my inner batteries. Therefor, I hope to spend more time with you in the following months.

Contents

Nomenclature

Operators

Variable	Meaning	Units
$\frac{\partial}{\partial}$	Partial derivative	-
$\frac{\mathrm{D}}{\mathrm{D}t}$	material derivative	$\frac{1}{\mathrm{s}}$
∇	Nabla Operator	$\frac{1}{\mathrm{m}}$
Δ	Laplace Operator	$\frac{1}{\mathrm{m}^2}$
$\mathscr{F}$	Fourier transformation	-
$\Re$	Real part	-
$\overline{(.)}$	Time average	-
$\widetilde{(.)}$	Density-weighted time average	-
$(.)^H$	Hermitian	-

Subscripts and Superscripts

Variable	Meaning	Units
$(.)_{fl}$	Fluid	-
$(.)_i$, $(.)_j$, $(.)_k$	Index variables for Einstein notation	-
$(.)_r$	Eigenmode	-
$(.)_{st}$	Structure	-
$(.)_\Psi$	Traveling wave formulation	-
$(.)'$	Reynolds decomposed fluctuations	-
$(.)''$	Favre decomposed fluctuations	-
$(.)^r$	Eigenmode	-

Latin letters

Scalars

Variable	Meaning	Units
A	Surface Area	m^2
A_0	Aerodynamic damping	$\frac{\mathrm{kg}}{\mathrm{s}}$
A_1	Aerodynamic stiffness	$\frac{\mathrm{kg}}{\mathrm{s}^2}$
E_{tot}, E_{kin}, E_{pot}	Total, kinetic and potential Energy	$\frac{\mathrm{kg}\cdot\mathrm{m}^2}{\mathrm{s}^2}$
F_{Thrust}	Thrust	$\frac{\mathrm{kg}\cdot\mathrm{m}}{\mathrm{s}^2}$
F_A	Aerodynamic force	$\frac{\mathrm{kg}\cdot\mathrm{m}}{\mathrm{s}^2}$
G_{-1}, G_0, G_{+1}, G_{+2}	Coarsest to finest mesh	-
H	Number of considered harmonics	-
M	Molar mass	$\frac{\mathrm{kg}}{\mathrm{mol}}$
P	Power	$\frac{\mathrm{kg}\cdot\mathrm{m}^2}{\mathrm{s}^3}$
R	Universal gas constant	$\frac{\mathrm{kg}\cdot\mathrm{m}^2}{\mathrm{s}^2\cdot\mathrm{K}\cdot\mathrm{mol}}$
S	Sutherland constant	K
T	Period	s
T	Temperature	K
V	Volume	m^3
W	Work	$\frac{\mathrm{kg}\cdot\mathrm{m}^2}{\mathrm{s}^2}$
a	Speed of sound	$\frac{\mathrm{m}}{\mathrm{s}}$
c_p, c_V	Heat capacity at constant pressure and volume	$\frac{\mathrm{kg}\cdot\mathrm{m}^2}{\mathrm{s}^2\cdot\mathrm{K}}$
d	Damping	$\frac{\mathrm{kg}}{\mathrm{s}}$
e	Specific energy	$\frac{\mathrm{m}^2}{\mathrm{s}^2}$
h	Specific enthalpy	$\frac{\mathrm{m}^2}{\mathrm{s}^2}$
k	Turbulent kinetic energy	$\frac{\mathrm{m}^2}{\mathrm{s}^2}$
k	Stiffness	$\frac{\mathrm{kg}}{\mathrm{s}^2}$
$\widetilde{k}_r$	Modal stiffness	$\frac{\mathrm{kg}\cdot\mathrm{m}^2}{\mathrm{s}^2}$
l	Largest eddy length scale	m
m	Mass	kg
$\widetilde{m}_r$	Modal mass	$\mathrm{kg}\cdot\mathrm{m}^2$
$\dot{m}$	Mass flow rate	$\frac{\mathrm{kg}}{\mathrm{s}}$
p	Static pressure	$\frac{\mathrm{kg}}{\mathrm{m}\cdot\mathrm{s}^2}$

Variable	Meaning	Units
p_2	Static outlet pressure / Backpressure	$\frac{\mathrm{kg}}{\mathrm{m \cdot s^2}}$
p_t	Total pressure	$\frac{\mathrm{kg}}{\mathrm{m \cdot s^2}}$
r	Eigenmode	-
t	Time	s
u	Velocity	$\frac{\mathrm{m}}{\mathrm{s}}$
u^+	Dimensionless velocity	-
u_τ	Friction velocity	$\frac{\mathrm{m}}{\mathrm{s}}$
w	Specific work	$\frac{\mathrm{m^2}}{\mathrm{s^2}}$
x	Displacement or coordinate	m
$\dot{x}$	Displacement velocity	$\frac{\mathrm{m}}{\mathrm{s}}$
$\ddot{x}$	Displacement acceleration	$\frac{\mathrm{m}}{\mathrm{s^2}}$
y	Wall distance	m
y^+	Dimensionless wall distance	-

Vectors

Variable	Meaning	Units
$\vec{c}$	Velocity vector in an absolute frame of reference	$\frac{\mathrm{m}}{\mathrm{s}}$
$\vec{f}$	External force vector	$\frac{\mathrm{kg \cdot m}}{\mathrm{s^2}}$
$\vec{n}$	Surface normal	-
$\vec{q}$	Generalized coordinate vector	-
$\ddot{\vec{q}}$	Generalized acceleration vector	$\frac{1}{\mathrm{s^2}}$
$\vec{u}$	Velocity vector	$\frac{\mathrm{m}}{\mathrm{s}}$
$\vec{v}$	Velocity vector in a relative frame of reference	$\frac{\mathrm{m}}{\mathrm{s}}$
$\vec{x}$	Displacement or coordinate vector	m
$\dot{\vec{x}}$	Displacement velocity vector	$\frac{\mathrm{m}}{\mathrm{s}}$
$\ddot{\vec{x}}$	Displacement acceleration vector	$\frac{\mathrm{m}}{\mathrm{s^2}}$
$\vec{B}$	Body force acceleration	$\frac{\mathrm{m}}{\mathrm{s^2}}$
$\vec{F}$	Aerodynamic force vector	$\frac{\mathrm{kg \cdot m}}{\mathrm{s^2}}$
$\vec{Q}$	State vector	
$\vec{R}$	Residual vector	

Tensors

Variable	Meaning	Units
$[\boldsymbol{D}]$	Damping matrix	$\frac{\mathrm{kg}}{\mathrm{s}}$
$[\widetilde{\boldsymbol{F}}]$	Generalized aerodynamic influence coefficient matrix	$\frac{\mathrm{kg \cdot m^2}}{\mathrm{s^2}}$
$[\boldsymbol{K}]$	Stiffness matrix	$\frac{\mathrm{kg}}{\mathrm{s^2}}$
$[\widetilde{\boldsymbol{K}}]$	Generalized stiffness matrix	$\frac{\mathrm{kg \cdot m^2}}{\mathrm{s^2}}$
$[\boldsymbol{M}]$	Mass matrix	kg
$[\widetilde{\boldsymbol{M}}]$	Generalized mass matrix	$\mathrm{kg \cdot m^2}$
$[\boldsymbol{S}]$	Strain rate tensor	$\frac{1}{\mathrm{s}}$

Greek letters

Scalars, vectors and tensors

Variable	Meaning	Units
α	Angle of attack / Incidence angle	$\circ$
γ	Heat capacity	-
β	Stagger angle	$\circ$
δ	Damping coefficient	$\frac{\mathrm{rad}}{\mathrm{s}}$
η	Kolmogorov length	m
η_F	Propulsion efficiency	-
η_B	Brayton cycle efficiency	-
κ	Kármán constant	-
κ_θ	Heat conductivity	$\frac{\mathrm{kg \cdot m}}{\mathrm{s^3 \cdot K}}$
λ	Eigenvalue	$\frac{1}{\mathrm{s^2}}$
μ	Dynamic viscosity	$\frac{\mathrm{kg}}{\mathrm{m \cdot s}}$
μ_t	Turbulent viscosity	$\frac{\mathrm{kg}}{\mathrm{m \cdot s}}$
ν	Kinematic viscosity	$\frac{\mathrm{m^2}}{\mathrm{s}}$
ρ	Density	$\frac{\mathrm{kg}}{\mathrm{m^3}}$
σ_n	Inter-Blade Phase Angle	$\circ$
τ_{W}	Wall shear stress	$\frac{\mathrm{kg}}{\mathrm{m \cdot s^2}}$
φ	Phase angle	rad

Variable	Meaning	Units
ω_0	Undamped eigenfrequency	$\frac{\mathrm{rad}}{\mathrm{s}}$
ω	Eigenfrequency	$\frac{\mathrm{rad}}{\mathrm{s}}$
ω	Specific dissipation rate	Hz
Λ	Logarithmic decrement	-
$\vec{\theta}$	Heat flux vector	$\frac{\mathrm{kg}}{\mathrm{s}^3}$
$\vec{\phi}$	Eigenvector	m
$\vec{\psi}$	Eigenvector in traveling wave formulation	m
$\vec{\Omega}$	Angular frequency vector	$\frac{\mathrm{rad}}{\mathrm{s}}$
$[\boldsymbol{\tau}]$	Shear stress tensor	$\frac{\mathrm{kg}}{\mathrm{m \cdot s}^2}$
$[\mathbf{\Phi}]$	Modal matrix	m

Abbreviations

Abbreviation	Meaning
CFD	Computational Fluid Mechanics
CFRP	Carbon Fiber Reinforced Polymers
DNS	Direct Numerical Simulation
FANS	Favre-Averaged Navier Stokes
FDM	Finite Difference Method
FEA	Finite Element Analysis
FEM	Finite Element Method
FVM	Finite Volume Method
IBPA	Inter-Blade Phase Angle
LES	Large Eddy Simulation
ND	Nodal Diameter
PS	Pressure side
RANS	Reynolds-Averaged Navier Stokes
RCL	Relative chord length
RoR	Rate of Rotation
SS	Suction side

List of Figures

List of Tables

1. Motivation

The European Union under the European Green Deal is aiming to reduce greenhouse gas emissions by 55% until 2030 compared to 1990 and achieve a climate-neutral economy by 2050 [6]. In 2011, the aviation sector was responsible for about 3.5% of global net anthropogenic effective radiative forcing [7], while passenger flight numbers are forecast to triple by 2050 [8]. In order to accomplish these objectives, efficiency must be improved across all areas of aircraft flight, and long-term developments of novel, low emission propulsion technologies are necessary.
In order to increase overall aircraft efficiency, engineers and scientists work to lower aircraft drag, decrease weight and increase engine efficiency. To improve engine performance, modern turbofan engines employ increasingly larger fan diameters, enabling higher bypass ratios. To reduce the number of compressor stages, thus saving weight, pressure ratios in all compressor stages are increased with each new design iteration. Additionally, new materials and manufacturing methods, such as Carbon Fiber Reinforced Polymers (CFRP) for fan and front compressor stages, are introduced to further reduce weight. All these improvements increase the susceptibility to aeroelastic phenomena, which can lead to high-cycle fatigue or structural failure, resulting in reduced lifetimes of jet engines or even threatening the safety of the aircraft and its passengers. To mitigate these risks, a thorough understanding of aeroelasticity and prediction of unsteady phenomena, such as forced response and flutter, is necessary during the development of modern jet engines to ensure safe and efficient operation. In this work, the aerodynamic mechanisms of flutter, which describes self-excited vibrations of the blades, are investigated.

Investigations of aeroelastic phenomena in powered aircraft are as old as the first machines themselves. During their first flights in 1903, the Wright brothers noticed aeroelastic deformations of propellers that degraded performance [9]. Wing torsional divergence occurred in the first monoplanes, which is why biplanes initially prevailed due to their better stability. Early fighter airplanes during the world wars often encountered flutter and wing torsional divergence, leading to increasing interest in flutter research [10]. With the emergence of jet engines during the 1940s, aeroelastic phenomena, especially flutter in turbomachinery, became increasingly relevant [11, 12, 13]. Unlike wing flutter, turbomachinery blades are aerodynamically coupled with adjacent blades, introducing additional physical mechanisms to their aeroelastic behavior. Advancements in computer technology during the 1950s and 60s enabled the use of Finite Element Analysis (FEA) to solve structural and aerodynamic problems. Since the 1970s, Computational Fluid Dynamics (CFD) and Finite Element Methods (FEM) have been standard tools in aeroelastic investigations [10].

The focus of flutter research in turbomachines lies mainly in fans and compressor front stages. Flutter can occur at different operating points in a variety of flow regimes, due to different fluid-structure interactions. For sub- and transonic flow regimes, flutter occurs mostly in choked flows and near the stall line. For supersonic conditions, flutter prediction becomes more important due to the fact that it can occur near the working line. A qualitative mapping of the regions on a compressor map, where flutter is generally predicted to occur, is shown in figure 1.1. This general categorization was introduced as early as the 1970s [14] and still holds true for modern designs, indicating fundamental physical mechanisms causing flutter onset in each flow regime.
The investigations in this thesis will focus on transonic flutter in regions I and Ia, pictured in figure 1.1, and its physical mechanisms. The name Transonic Stall Flutter can be misleading, since rotor blades in fans and compressors do not necessarily have to be stalled for flutter to arise [14]. The name stems from the fact that flutter starts to arise near the stall line.
Numerous studies found the influence of shock oscillations as a primary driver of aeroelastic instability in transonic fans and compressors [15, 16, 17, 18, 19, 20, 21]. The first bending mode is more severely influenced compared to the first torsional mode [22]. While some researchers found the pressure oscillations of the shocks to be stabilizing and the separation region behind them to be destabilizing [16, 20, 21], others observed the contrary [15, 17, 18, 23]. Martin et al. observed opposite behavior for the first bending and first torsional mode [23]. Zhang et al. found the shock wave to be damping for positive inter-blade phase angles (IBPAs) and exciting for negative IBPAs [19]. The pressure side has only minor influence on flutter stability

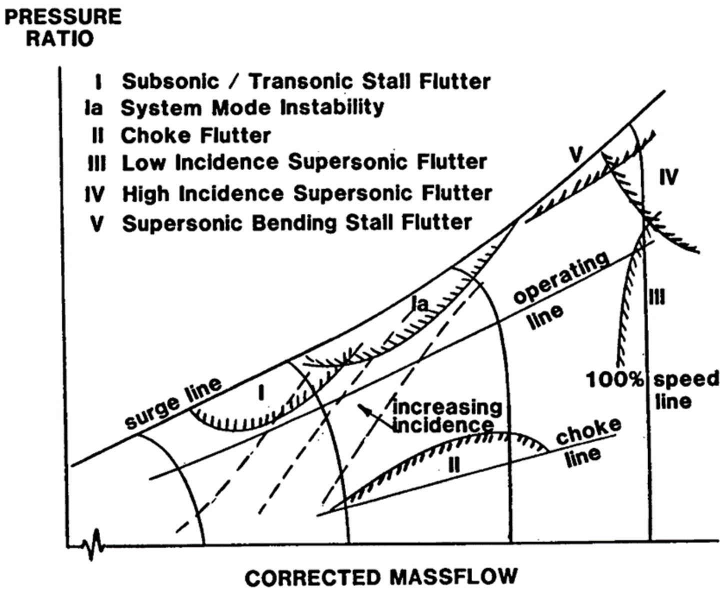

Figure 1.1.: Description of flutter regions on an exemplary compressor map [1].

[17, 18, 19, 20]. Vahdati et al. emphasized the impact of steady-state flow determination on flutter prediction and identified an additional type of flutter, caused by reflected pressure waves, that can occur near the working line [16, 24]. The plethora of studies indicates a high sensitivity of flutter stability to flow regimes and blade geometries.

While the flow structures are generally three-dimensional with tip vortices and radial secondary flow structures, in this work, a two-dimensional analysis will be conducted to investigate the mechanisms behind transonic stall flutter for multiple operating points and IBPAs for the first bending and first torsional modes. This allows to separate the influence of two- and three-dimensional phenomena to analyze them independently from each other; furthermore two-dimensional analysis reduces the needed computational resources and time drastically.

In the following, the theory behind aerodynamics, aeroelasticity and the used numerical methods for analysis of turbomachinery are described in chapter 2. The simulation workflow, setup and geometry are presented in chapter 3. A mesh sensitivity study is conducted and the evaluation is discussed in chapter 4. Unsteady flutter simulations are performed. The results are analyzed and discussed in chapter 5. The thesis concludes in chapter 6 and an outlook of possible future work is given.

2. Theory

2.1. Axial compressors

Turbomachines use rotating blades to extract or transfer kinetic energy from or to a flow [25]. Turbines extract energy and compressors transfer energy to the flow. Turbomachines can be classified according to their internal flow direction into radial-flow and axial-flow machines. In radial-flow turbomachines, the fluid flow is pushed outward, perpendicular to the axis of rotation. In axial-flow machines, the fluid flow is parallel to the axis of rotation. The basic principles of axial compressors and the aerodynamics of annular cascades are outlined in this section.

2.1.1. Basics of axial compressors

All jet engine designs use Newton's third law to generate thrust. Air at flight speed is accelerated by a Brayton cycle [26] to generate thrust. At the beginning of the Brayton cycle, air is compressed. In turbojet engines, this is done by a compressor. The efficiency of an ideal Brayton cycle is given by

$$\eta_B = 1 - \frac{T_1}{T_2} = 1 - \left(\frac{p_1}{p_2}\right)^{(\gamma-1)/\gamma}, \tag{2.1}$$

where p_1, T_1 and p_2, T_2 are the pressure and temperature at the beginning and the end of the cycle respectively and γ is the heat capacity ratio [3, p.494]. From equation (2.1) it is straightforward that an increase in compression ratio leads to an increase in efficiency. Thrust in a jet engine is proportional to the mass flow $\dot{m}$ and the difference in velocities of the jet u_{Jet} and the flight speed u_{Flight}

$$F_{\text{Thrust}} = \dot{m} \cdot (u_{\text{Jet}} - u_{\text{Flight}}), \tag{2.2}$$

while the propulsion efficiency η_{F} can be calculated by [3, p. 431]

$$\eta_F = \frac{2}{2 + \frac{u_{\mathrm{Jet}}}{u_{\mathrm{Flight}}}} \,. \tag{2.3}$$

Turbofan engines add a fan in front of a turbojet engine core that propels air, bypassing the core of the engine, to increase overall mass flow and engine efficiency, as follows from equations (2.2) and (2.3). A schematic overview of a turbofan engine is shown in figure 2.1.

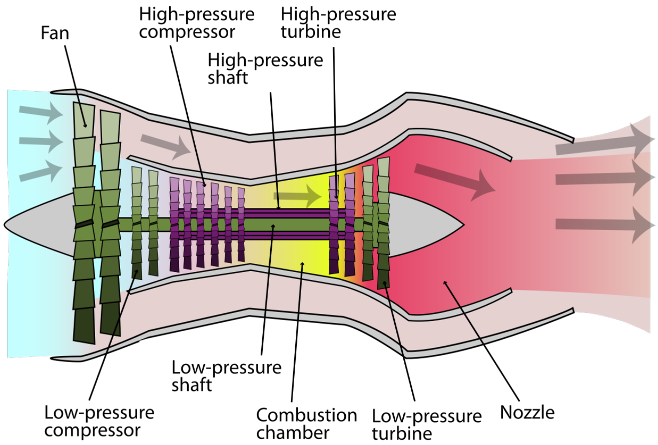

Figure 2.1.: Schematic of a turbofan engine [2].

Compressor and fan blades, as well as their disks, are commonly manufactured using titanium alloys. In the past, blades and disks were most often forged or cast separately. During the 1990s, so called blisks (from 'bladed disks'), in which the blades are integrated into the disks, were introduced in commercial turbo engines, reducing the number of parts and therefore saving weight. The use of CFRPs emerged for fan blades and recent studies are conducted on CFRP designs of front row compressor stages [27]. These improvements in materials and manufacturing techniques lead to efficiency increases of turbo engines from weight savings, higher blade loadings and bypass ratios, often at the cost of structural rigidity. The introduction of blisks reduces structural damping and higher blade loads can lead to increasing stresses. This makes accurate predictions of unsteady aeroelastic phenomena such as flutter during the design phase of compressors necessary to ensure safety and efficiency.

2.1.2. Aerodynamics of annular cascades

Axial compressors are rotating, airfoil shaped blades, that transfer kinetic energy to the incoming air, increasing its energy and static pressure. A schematic overview

of a compressor stage, comprising a rotor and stator row, is shown in figure 2.2. The pressure sides of blades in an axial compressor face in the direction of rotation. Their airfoil shape helps to efficiently turn the flow without separation. Blades often have a three-dimensional design, being twisted along their span to provide a nearly constant incidence angle across the whole span. To reduce the velocity and further increase static pressure, the blade passage has a slight diffuser shape.
Incoming air has a velocity vector $\vec{c}_1$, with an axial component c_{1ax} and a tangential component c_{1u}. The tangential component is also called swirl velocity. The tangential velocity of the reference frame in front of the rotor is u_1. The resulting relative velocity vector is $\vec{v}_1$. The rotating blades impart a tangential velocity component to the airflow, increasing c_{2u} compared to c_{1u}. This reduces the relative velocity vector $\vec{v}_2$ behind the rotor and would change the incidence angle of the flow on the next compressor stage. A stator row is positioned behind the rotor to reduce the swirl velocity c_{4u} and condition a nearly axial velocity vector $\vec{c}_4$ behind the compressor stage. Note that figure 2.2 does not use vector notation.

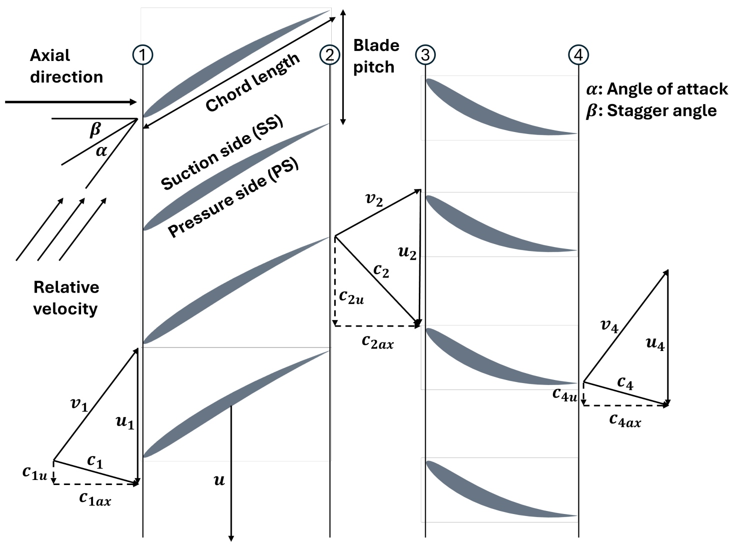

Figure 2.2.: Schematic overview of a rotor and stator passage with velocity vectors.

The power that is transferred from the compressor to the flow can be estimated using Euler's turbine equation [3, p. 710]

$$P = \dot{m} \cdot u \cdot (c_{2u} - c_{1u}) \,. \tag{2.4}$$

Here u is the circumferential velocity of the blade. It follows that higher mass flows, higher circumferential rotor velocities and higher increases in swirl velocity lead to increases in the pressure ratio of the compressor. Ideally, the swirl of the incoming flow is zero and the swirl imparted by the rotor is maximized. The increase in swirl of the flow is limited by a critical incidence angle at which the flow separates.

Flow fields in turbomachines are highly complex and three-dimensional in nature. They are characterized by strong pressure gradients, turbulence, rotation and compressibility. Flow regimes may be sub-, trans- or supersonic, depending on rotation rate and boundary conditions. In transonic and supersonic flows, shocks are present and interact with the boundary layer. This can lead to performance losses as well as stalling. Vortices form at the tip of blades and can interact with the shroud boundary layer, wakes and downstream blade rows. Pressure gradients exist in all directions and together with rotation, can lead to secondary flows.
In this work, a two-dimensional section of a NACA 3506 rotor is analyzed. In the following, the principal aerodynamics and most important phenomena regarding stall flutter that are present in two-dimensional flows will be described.

2.1.2.1. Boundary layers

At a solid boundary, the flow velocity is equal to the velocity of the boundary. This so called no-slip condition arises from the friction of fluid particles and the surface. In between the bulk flow and the surface, the boundary layer develops. It is a thin layer of fluid, where the velocity changes from the boundary velocity to the bulk velocity of the flow. Above a critical Reynolds number, the flow in the boundary layer transitions from a laminar into a turbulent flow. A turbulent boundary layer can be divided into three regions, according to the dimensionless distance to the wall [28, p.561]

$$y^+ = \frac{y u_\tau}{\nu}, \quad u_\tau = \sqrt{\frac{\tau_\mathrm{w}}{\rho}}, \quad \tau_\mathrm{w} = \mu \frac{\partial u}{\partial y}\bigg|_\mathrm{w}. \tag{2.5}$$

Here, y is the distance to the wall, ν is the kinematic viscosity, u_τ is the friction velocity, ρ is the density and τ_w is the wall shear stress, which is proportional to the velocity gradient at the wall. The dimensionless velocity is defined as

$$u^+ = \frac{u}{u_\tau}. \tag{2.6}$$

In the turbulent boundary layer, u^+ can be related to y^+. The region nearest to the wall at $y^+ < 5$ is called Viscous Sublayer, where viscous forces dominate. For

$30 < y^+ < 200$, inertial forces dominate over viscous forces. This region is called log-law region, because of a logarithmic relation between y^+ and u^+ applies. Between both regions, a buffer layer is located.
In the presence of adverse pressure gradients, the boundary layer separates if the kinetic flow energy cannot overcome the pressure gradient. At the separation point, the velocity gradient perpendicular to the wall and consequently, the wall shear stress vanishes. If the detached flow regains energy, it can reattach, which then forms a separation bubble.

2.1.2.2. Stall

On the suction side of an airfoil, the fluid flows against an adverse pressure gradient. With increasing incidence angles, the pressure gradient increases. At the critical incidence angle, the flow separates as described previously.
In turbomachines, the fluid flows around the rotor and stator with an incidence angle. This angle depends not only on the geometry, but also on the rotational rate and the span radius. If the incidence angle becomes too high, the flow separates locally in one passage. This effectively decreases the passage area between two blades, building up pressure in front of the passage. Subsequently, the incidence angle at the next blade in the direction against the rotational direction increases. This leads to flow separation in the next passage. Since overall mass flow reduces, the static pressure decreases and flow in the previously stalled passage recovers. This phenomenon is called rotating stall and is schematically depicted in figure 2.3.

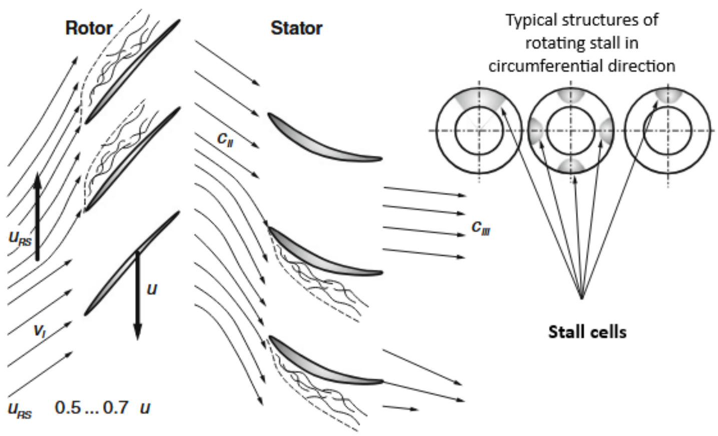

Figure 2.3.: Flow schematic of rotating stall (translated from [3]).

2.1.2.3. Shock waves

The Mach number

$$\mathrm{Ma} = \frac{u}{a}, \quad a_{\mathrm{ideal}} = \sqrt{\gamma \cdot \frac{p}{\rho}} = \sqrt{\gamma \cdot \frac{R \cdot T}{M}} \tag{2.7}$$

is a dimensionless parameter that compares the velocity u to the speed of sound a. It is not constant for a given flow, since both u and a vary in space and time. For ideal gases, the speed of sound varies with the pressure, density and temperature. Here R is the universal gas constant and M is the molar mass of the fluid.
The Mach number is used to describe the flow regime. At $Ma = 1$, discontinuities in pressure, temperature, and density occur, which are called shock waves (short: shocks). Flows with Mach numbers below unity are called subsonic flows. If shocks are present, but the general Mach number in the flow field is between $0.8 < \mathrm{Ma} < 1.2$, the flow is called transonic. Flows with general Mach numbers over $\mathrm{Ma} = 1.2$ are called supersonic. An example of flow field contour plots is shown in figure 2.4.

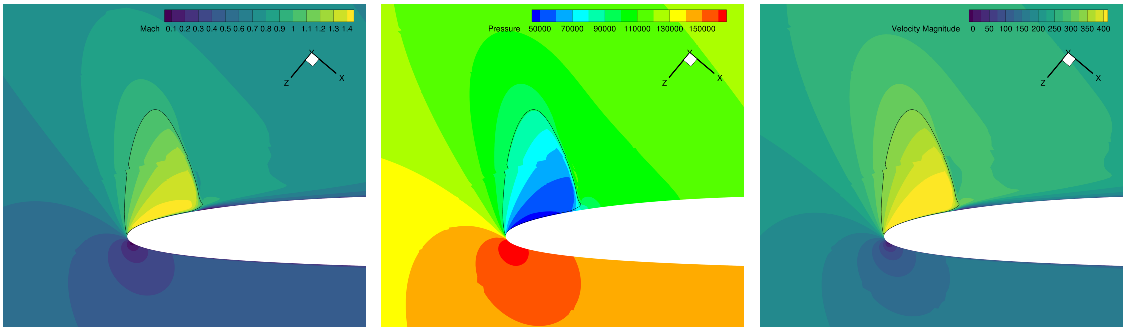

(a) Mach number. (b) Pressure. (c) Velocity magnitude

Figure 2.4.: Contour plots of Mach number, pressure and velocity magnitude for shock wave visualization.

Changes in fluid properties depend on the Mach number in front of the shock. The pressure rises according to the shock relations [29, p. 842]

$$\frac{p_2}{p_1} = 1 + \frac{2\gamma}{\gamma + 1}\left(\mathrm{Ma}_1^2 - 1\right) \tag{2.8}$$

where the index $(.)_1$ indicates the location in front and index $(.)_2$ behind the shock. This sudden rise in static pressure imposes an adverse pressure gradient downstream, thickening the boundary layer and increasing the risk of separation. Shocks can reflect at boundaries and interact with each other as well as influence other flow structure as already mentioned with boundary layers.

2.1.3. Compressor map

The performance of a compressor can be characterized by a compressor map. The pressure ratio is plotted against the mass flow. The operating condition of a compressor depends on the rotational rate of the rotor and the backpressure at the outlet. An example of a compressor map is shown in figure 2.5. Each speed line represents a constant rotational rate; speed lines of higher rotational rates are to the right. Increasing backpressure moves an operating point to the left on a speed line. The choke region is located on the right side of each speed line at low pressure ratios. It is the vertical part of each speed line. Here, the Mach number reaches unity in the passage and maximum mass flow rates are reached. The stall line lies on the left side of each speed line at high backpressure. There, the flow begins to separate and stalling occurs. These regions limit the operating range of a compressor. In practice, the operating range is further restricted because aeroelastic effects such as flutter often begin to arise earlier.

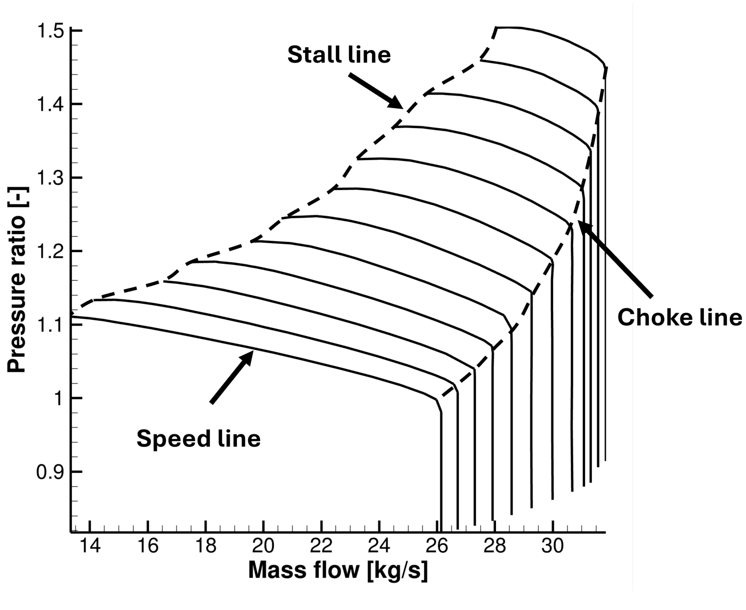

Figure 2.5.: Compressor map of the NACA 3506 airfoil analyzed in this work.

2.2. Aeroelasticity

Aeroelasticity is the study of inertial, elastic and aerodynamic forces and their interactions, that arise while an elastic body is exposed to an airflow. The interactions are depicted in the Collar triangle of forces [30], shown in figure 2.6.

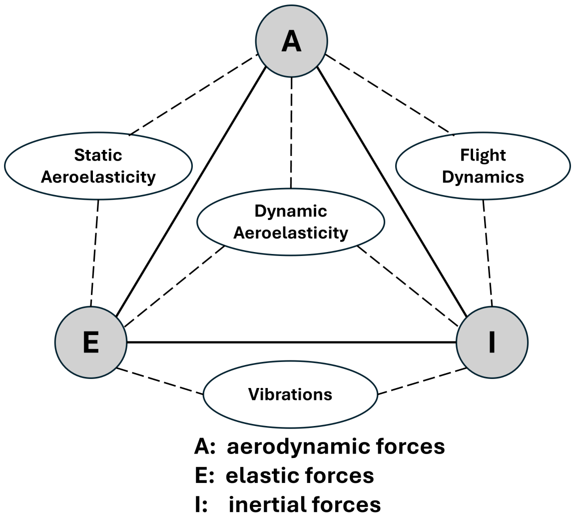

Figure 2.6.: Collar triangle of forces.

Aeroelasticity can be classified into static aeroelasticity, which deals with the interaction of aerodynamic and elastic forces; and into dynamic aeroelasticity, where all three forces of the Collar Triangle interact. Dynamic aeroelasticity in turbomachinery can be further divided.

Flutter is a self-excited aeroelastic instability of an elastic body in airflow, arising from the coupling between structural motion and unsteady aerodynamic forces. The aerodynamic forces, induced by the motion, will either dampen or excite the system. Flutter occurs, if the aerodynamic excitation exceeds the structural damping. Vibration amplitudes may grow exponentially, potentially leading to rapid structural failure, or if limited by nonlinear effects, resulting in limit-cycle oscillations that can cause high-cycle fatigue.

Forced response is a vibration phenomenon driven by externally imposed unsteady aerodynamic forces, such as those arising from wake and potential-field interactions with upstream blade rows or other flow-field disturbances. If frequencies of these forces are close to a structural natural frequency, they can induce large, finite vibration amplitudes, leading to increased blade fatigue.

To investigate flutter in turbomachinery, the interaction of structural and aerodynamic forces needs to be modeled. In this section, the mathematical description of flutter is introduced and the aeroelastic stability equation of an annular cascade is presented in traveling wave formulation.

2.2.1. Flutter

The equation of motion for a rigid wing with one degree of freedom, mass m, damping d and stiffness k, can be modeled as a spring-damper system

$$m\ddot{x}(t) + d\dot{x}(t) + kx(t) + F_A(t) = 0\,, \tag{2.9}$$

with external aerodynamic forces

$$F_A(t) = A_0\dot{x} + A_1 x\,, \tag{2.10}$$

that are proportional to the displacement x and the displacement velocity $\dot{x}$. Equation (2.9) can be solved using the Ansatz $x(t) = x_0 e^{\lambda t}$, with the solution

$$\lambda = -\frac{d + A_0}{2m} \pm \sqrt{\frac{k + A_1}{m} - \left(\frac{d + A_0}{2m}\right)^2}\,. \tag{2.11}$$

Comparing equation (2.11) to the general solution of an eigenvalue problem

$$\lambda = -\delta \pm i\omega\,, \tag{2.12}$$

the damping coefficient, undamped and damped natural frequency can be identified

$$\delta = \frac{d + A_0}{2m}\,, \quad \omega_0 = \sqrt{\frac{k + A_1}{m}} \quad \text{and} \quad \omega = \sqrt{\omega_0^2 - \delta^2} \tag{2.13}$$

The sign of the damping coefficient indicates if an oscillation decays or increases:

- $\delta > 0$: the oscillation is damped, amplitude decreases,
- $\delta = 0$: no damping nor excitation, amplitude stays constant,
- $\delta < 0$: the oscillation is excited, amplitude increases, flutter occurs.

The term $A_0\dot{x}$ can be identified as aerodynamic damping. For $A_0 < 0$, the fluid transfers energy to the wing. Since $d \geq 0$, for $A_0 < -d$ flutter occurs.

2.2.2. Aeroelastic stability of annular cascades

The aeroelastic stability of an annular cascade is analyzed using a similar approach to that outlined in section 2.2.1. A more general description is employed to accommodate more degrees of freedom, since a cascade comprises of multiple blades that interact aerodynamically and can oscillate in varying modes. For computations, the blades are discretized into finite elements. In the following, the formulation of the stability problem is introduced via purely structural dynamics. The problem is transformed into the traveling wave formulation due to the aerodynamic coupling between adjacent blades. Finally, the flutter equation for turbomachines is formulated.

2.2.2.1. Structural dynamics

To solve the equation of motion for an annular cascade using a Finite Element Solver solver, equation (2.9) has to be solved in its discretized form

$$[\boldsymbol{M}]\ddot{\vec{x}}(t) + [\boldsymbol{D}]\dot{\vec{x}}(t) + [\boldsymbol{K}]\vec{x}(t) = \vec{f}(t)\,, \tag{2.14}$$

where $[\boldsymbol{M}]$, $[\boldsymbol{D}]$ and $[\boldsymbol{K}]$ are the discrete mass, damping and stiffness matrix respectively [22, p.13-5]. The vectors $\vec{f}(t)$ and $\vec{x}(t)$, $\dot{\vec{x}}(t)$ and $\ddot{\vec{x}}(t)$ are the discrete external forcing and discrete displacement and it's time derivatives respectively. Without external forcing and neglecting the structural damping, equation (2.14) becomes

$$[\boldsymbol{M}]\ddot{\vec{x}}(t) + [\boldsymbol{K}]\vec{x}(t) = 0 \tag{2.15}$$

The neglection of $[\boldsymbol{D}]$ is justified by the low damping ratios of metals and blisk designs. The stiffness $[\boldsymbol{K}]$ of a rotor in operation is not a constant, but depends on the inertial load experienced by rotation and aerodynamic loads. In this work, the rotor stiffness is assumed to be constant. Using the Ansatz

$$\vec{x}(t) = \vec{\phi}\, e^{\lambda t} \tag{2.16}$$

to solve equation (2.15) yields

$$\Big([\boldsymbol{K}] + \lambda^2[\boldsymbol{M}]\Big)\vec{\phi} = 0\,, \tag{2.17}$$

which is an eigenvalue problem, whose solutions are the modeshapes $\vec{\phi}_r$ and eigenvalues λ_r for the eigenmode r. The displacement vector $\vec{x}(t)$ can be written as superposition of the eigenmode shapes in generalized coordinates $\vec{q}(t)$

$$\vec{x}(t) = [\mathbf{\Phi}]\,\vec{q}(t)\,. \tag{2.18}$$

The modal matrix $[\mathbf{\Phi}]$ consists of all eigenmode shapes. The generalized coordinates describe the contribution of each eigenmode to the overall deformation. Inserting equation (2.18) into equation (2.15) and multiplying the hermitian modal matrix $[\mathbf{\Phi}]^H$ yields [22, p.13-6]

$$\begin{aligned} [\mathbf{\Phi}]^H[\boldsymbol{M}][\mathbf{\Phi}]\,\ddot{\vec{q}}(t) \quad &+ \quad [\mathbf{\Phi}]^H[\boldsymbol{K}][\mathbf{\Phi}]\,\vec{q}(t) &= \quad 0\,,\\ [\widetilde{\boldsymbol{M}}]\,\ddot{\vec{q}}(t) \quad &+ \quad [\widetilde{\boldsymbol{K}}]\,\vec{q}(t) &= \quad 0\,, \end{aligned} \tag{2.19}$$

introducing the generalized mass $[\widetilde{\boldsymbol{M}}]$ and stiffness matrices $[\widetilde{\boldsymbol{K}}]$

$$[\widetilde{\boldsymbol{M}}] = \begin{bmatrix} \ddots & & \\ & \widetilde{m}_r & \\ & & \ddots \end{bmatrix} \quad \text{and} \quad [\widetilde{\boldsymbol{K}}] = \begin{bmatrix} \ddots & & \\ & \widetilde{k}_r & \\ & & \ddots \end{bmatrix}\,, \tag{2.20}$$

that contain the modal masses $\widetilde{m}_r$ and modal stiffnesses $\widetilde{k}_r$. Since the eigenmodes are decoupled, $[\widetilde{\boldsymbol{M}}]$ and $[\widetilde{\boldsymbol{K}}]$ are diagonal. For better comparability it is common practice to scale the eigenvectors $\vec{\phi}_r$ so that $\widetilde{m}_r = 1\,\mathrm{kg\,m^2}$ and $\widetilde{k}_r = \widetilde{m}_r\lambda_r^2$.

2.2.2.2. Traveling wave formulation and IBPAs

For an annulus with N coupled blades, the structural modeshapes $\vec{\phi}_r$ indicate the deformation of the blades. The modeshapes can be further divided into eigenvalues $\lambda_r^{\pm n}$ with corresponding eigenvectors $\vec{\phi}_r^{\pm n}$, with n ranging from 0 to $\frac{N}{2}$ for even N and 0 to $\frac{N-1}{2}$ for odd N. Following, the modeshapes $\vec{\phi}_r$ are called modeshape families. All blades experience the same physical deformation, with a phase shift between adjacent blades, caused by aerodynamic coupling. Considering only even values of N, for $n = 0$ and $n = \frac{N}{2}$, there exist a single eigenvalue λ_r^0 and $\lambda_r^{\frac{N}{2}}$ respectively. For λ_r^0, all blades deform in phase and for $\lambda_r^{\frac{N}{2}}$ all blades deform out of phase to each adjacent blade. These modeshapes manifest as standing waves. The remaining eigenvalues appear in pairs $\lambda_r^n = \lambda_r^{-n}$. The eigenmodes are categorized in analogy to circular plates as nodal diameters (ND) with ND $= n$, that describe the phase shift of adjacent blades. In figure 2.7 a selection of nodal diameters is visualized.

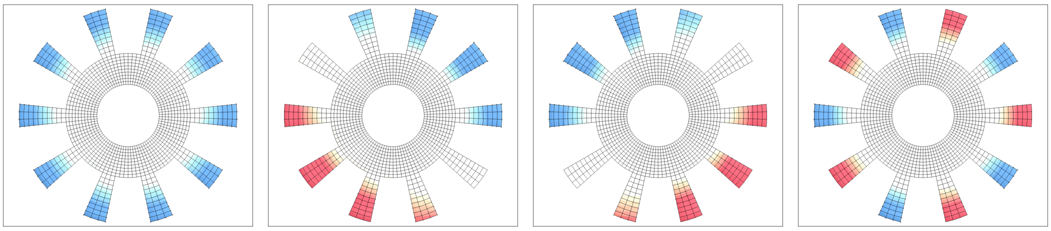

(a) ND $= 0\,,\ \phi^{n=0}$ (b) ND $= 1\,,\ \phi^{n=+1}$ (c) ND $= 1\,,\ \phi^{n=-1}$ (d) ND $= 5\,,\ \phi^{n=+5}$

Figure 2.7.: Modal analysis result of a simplified bladed disk (blue is into plane, red is out of plane) [4].

The eigenvalues $\lambda_r^n = \lambda_r^{-n}$ have the same deformation and phase shift, but are shifted by 180°. Their eigenvectors can be superimposed to

$$\begin{aligned} \vec{\psi}_r^{+n} &= \frac{1}{\sqrt{2}}\left(\vec{\phi}_r^{+n} + i\vec{\phi}_r^{-n}\right), \\ \vec{\psi}_r^{-n} &= \frac{1}{\sqrt{2}}\left(\vec{\phi}_r^{+n} - i\vec{\phi}_r^{-n}\right), \end{aligned} \tag{2.21}$$

which are also a solution to the eigenvalue problem of equation (2.19). These eigenvectors do not oscillate about their nodal diameter, but the maximum deflection travels as a wave about the axis of the rotor. Both $\vec{\psi}_r^{+n}$ and $\vec{\psi}_r^{-n}$ look the same, but travel in opposite directions. This formulation is called traveling wave formulation. It was first published by Lane in 1956 [31] and since then is a common method in flutter analysis. The phase shift of the deformation of blades can either be described using the nodal diameter or the inter-blade phase angle (IBPA)

$$\sigma_n = n \cdot \frac{2\pi}{N} \quad \text{with} \quad \left\{ -\frac{N}{2} < n \leq \frac{N}{2} \right\}. \tag{2.22}$$

Following this definition, nodal diameter and IBPA can be used interchangeably. Equation (2.19) can be written in traveling wave formulation, using similarly derived generalized mass and stiffness as

$$[\widetilde{\boldsymbol{M}}]_\Psi\, \ddot{\vec{q}}_\Psi(t) + [\widetilde{\boldsymbol{K}}]_\Psi\, \vec{q}_\Psi(t) = 0\,. \tag{2.23}$$

The factors $\frac{1}{\sqrt{2}}$ in equation (2.21) are chosen to yield

$$[\widetilde{\boldsymbol{M}}]_\Psi = [\widetilde{\boldsymbol{M}}] \qquad \text{and} \qquad [\widetilde{\boldsymbol{K}}_\Psi] = [\widetilde{\boldsymbol{K}}]\,. \tag{2.24}$$

2.2.2.3. Flutter equation

The complete discretized aeroelastic equation of motion reads

$$([\boldsymbol{M}]_{st} + [\boldsymbol{M}]_{fl})\,\ddot{\vec{x}}(t) + ([\boldsymbol{D}]_{st} + [\boldsymbol{D}]_{fl})\,\dot{\vec{x}}(t) + ([\boldsymbol{K}]_{st} + [\boldsymbol{K}]_{fl})\,\vec{x}(t) = \vec{f}_{st}(t) + \vec{f}_{fl}(t)\,. \tag{2.25}$$

The indices $(.)_{st}$ and $(.)_{fl}$ indicate properties of the structure and fluid respectively. With the assumption of a high mass ratio of blades to displaced fluid, the fluid mass can be neglected. As mentioned in section 2.2.2.1, it is commonly assumed that structural damping of turbomachinery blades is negligible. The structural stiffness is significantly higher than the fluid stiffness. Lastly, no external structural forces and for flutter, no external fluid forces, are applied. In summary, the assumptions

$$[\boldsymbol{M}]_{fl} = 0\,, \quad [\boldsymbol{D}]_{st} = 0\,, \quad [\boldsymbol{K}]_{fl} = 0\,, \quad \vec{f}_{st} = 0 \quad \text{and} \quad \vec{f}_{fl} = 0 \tag{2.26}$$

simplify equation (2.25) to

$$[\boldsymbol{M}]_{st}\,\ddot{\vec{x}}(t) + [\boldsymbol{D}]_{fl}\,\dot{\vec{x}}(t) + [\boldsymbol{K}]_{st}\,\vec{x}(t) = 0\,. \tag{2.27}$$

Similar to equation (2.23), equation (2.27) can be formulated in generalized traveling wave coordinates

$$[\widetilde{\boldsymbol{M}}]_{\Psi}\,\ddot{\vec{q}}_{\Psi}(t) + [\widetilde{\boldsymbol{K}}]_{\Psi}\,\vec{q}_{\Psi}(t) = [\widetilde{\boldsymbol{F}}]_{\Psi}\,\vec{q}_{\Psi}\,, \tag{2.28}$$

where on the right hand side of equation (2.28) are the generalized aerodynamic forces (GAF), that represent the fluid damping in equation (2.27). The matrix $[\widetilde{\boldsymbol{F}}]_{\Psi}$ contains the generalized aerodynamic influence coefficients in traveling mode formulation. Using the ansatz to solve equation (2.28)

$$\vec{q}_{\Psi} = \hat{\vec{q}}_{\Psi} e^{\lambda t} \tag{2.29}$$

yields the discretized flutter stability equation [32]

$$\left(\lambda^2[\widetilde{\boldsymbol{M}}]_{\Psi} + [\widetilde{\boldsymbol{K}}]_{\Psi} - [\widetilde{\boldsymbol{F}}]_{\Psi}\right) \cdot \hat{\vec{q}}_{\Psi} = 0\,. \tag{2.30}$$

To determine the flutter stability, equation (2.30) has to be solved or further assumptions must be applied, to simplify the investigation.

2.3. Numerical methods

To calculate the unsteady forces acting on the blades, the fluid flow through the blade passages must be determined. The principal governing equations for flows in turbomachines are the Navier-Stokes equations with accompanying equations of state. Due to their nonlinearity and coupling between velocity and pressure, there exist no general analytical solution for the Navier-Stokes equations. Simplifications and numerical methods must be applied to solve complex flows.
For the numerical solution of differential equations, the computational domain and the solved equations are discretized. Discretization transforms the system of differential equations into a system of algebraic equations. The most common method of discretization for CFD problems is the Finite-Volume Method (FVM), where the computational domain is divided into a finite number of control volumes (cells). The governing equations are expressed in their integral form and are applied to each control volume, ensuring that the flux of mass, momentum, and energy entering and leaving each cell balances the rate of change within. This ensures local and global conservation and is a key advantage of FVM compared to other methods such as Finite-Element or Finite-Difference Methods (FEM and FDM). Surface and volume integrals in the governing equations are discretized using numerical approximations. Fluxes across control volume faces are evaluated using interpolation schemes, while time derivatives are handled by explicit or implicit temporal discretizations. In most applications, simplifications or adaptations of the Navier-Stokes equations are performed. For turbulent and compressible flows, the Favre-Averaged Navier-Stokes equations together with a turbulence model are commonly utilized.

In the following, the governing equations describing the flow in turbomachinery are introduced. The methods to solve the differential equations of the unsteady flutter investigation in the frequency domain are described and the Energy Method, used to analyze the flutter stability, is presented.

2.3.1. Governing equations

The Navier-Stokes equations are the fundamental equations governing the flows of Newtonian fluids. They are a system of nonlinear partial differential equations, describing the conservation of mass, momentum, and energy. For compressible flows and heat transfer problems, they are accompanied by equations of state. Since resolving the turbulent length scales is not feasible, Favre-averaging is applied to derive the Favre-averaged Navier-Stokes equations, that are later numerically solved. The arising set of equations is closed by the $k-\omega$ turbulence model.

2.3.1.1. Navier-Stokes equations

The Navier-Stokes equations for compressible fluids are a system of five differential equations describing the conservation of mass, momentum and energy. Implemented in TRACE, in differential conservation form using index notation, they read [33]

$$\text{continuity} \quad \frac{\partial \rho}{\partial t} + \frac{\partial(\rho u_j)}{\partial x_i} = 0 \tag{2.31}$$

$$\text{momentum} \quad \frac{\partial(\rho u_i)}{\partial t} + \frac{\partial(\rho u_j u_i)}{\partial x_i} = -\frac{\partial p}{\partial x_i} + \frac{\partial \tau_{ij}}{\partial x_j} + \rho b_i \tag{2.32}$$

$$\text{energy} \quad \frac{\partial}{\partial t}\left[\rho\left(e + \frac{u_i u_j}{2}\right)\right] + \frac{\partial}{\partial x_j}\left[u_j \rho\left(h + \frac{u_i u_j}{2}\right)\right] = \frac{\partial}{\partial x_j}\left[-\theta_j + u_i \tau_{ij}\right] + \rho b_i u_i \tag{2.33}$$

with density ρ, velocity components u_i, static pressure p, specific energy e, specific enthalpy $h = e + \frac{p}{\rho}$, dynamic viscosity μ, temperature T and heat flux vector

$$\vec{\theta} = -\kappa_\theta \nabla T \,, \tag{2.34}$$

where κ_θ is the heat conductivity of the fluid. The elements of the shear stress tensor $[\boldsymbol{\tau}]$ and the strain rate tensor $[\boldsymbol{S}]$ are defined as

$$\tau_{ij} = 2\mu\left(S_{ij} - \frac{1}{3}\frac{\partial u_i}{\partial x_i}\right) \,, \quad S_{ij} = \frac{1}{2}\left(\frac{\partial u_i}{\partial x_j} + \frac{\partial u_j}{\partial x_i}\right) \,. \tag{2.35}$$

In a rotating reference frame with angular velocity $\vec{\Omega}$, the body force term $\vec{B}$ reads

$$\vec{B} = 2\vec{\Omega} \times \vec{u} + \vec{\Omega} \times (\vec{\Omega} \times \vec{x}) + \frac{\partial \vec{\Omega}}{\partial t} \times \vec{x} \,. \tag{2.36}$$

2.3.1.2. Thermodynamic equations of state

In the five equations, a total of eight variables were introduced: three velocities components u_i, the state variables p, ρ, e and T and the viscosity μ. To close the system of differential equations, additional equations of state and models, relating the state variables and fluid properties with each other, are introduced. For a perfect gas, the equations of state for the internal energy e and pressure p are [29, p.822]

$$e = c_V T\,, \quad p = \rho R T \tag{2.37}$$

To model the viscosity of perfect gases accurately, Sutherland's law [34] is applied

$$\mu = \mu_0 \frac{T_0 + S}{T + S} \left(\frac{T}{T_0}\right)^{3/2}, \tag{2.38}$$

with μ_0 and T_0 being the reference viscosity and temperature respectively, S is the Sutherland constant of the gas.

2.3.1.3. Favre averaged Navier Stokes equations

Turbulent flows are three-dimensional, unsteady and dominated by vortices. In addition to the mean flow velocity, fluctuations in all spatial directions are present. Vortices are formed using energy from the mean flow. Large eddies break down into smaller ones, transferring energy from the mean flow into the turbulent vortices. The smallest eddies dissipate their energy via viscous processes. This phenomenon is called Energy Cascade [35]. The size of the largest eddies l and the length scale of the smallest ones, called Kolmogorov length [36], can be related via

$$\frac{\eta}{l} \sim \left(\frac{\eta^3}{u^3 l^3}\right)^{1/4} = Re_l^{-3/4}\,. \tag{2.39}$$

The relative difference between the length scales of the smallest and largest vortices scales with the Reynolds number of the mean flow. This poses a major challenge in simulations of turbulent flows, since grids for direct numerical simulations (DNS) of the Navier-Stokes equations must be fine enough to resolve all length scales. This makes DNS practically impossible for most applications. Consequently, methods modeling the effects of turbulence are applied. Common approaches are the Reynolds- or Favre-averaged Navier-Stokes equations (RANS and FANS), where the flow variables are decomposed and the equations averaged; the mean flow is solved and turbulence is modeled. Other methods are Large Eddy simulations (LES), which resolve the largest eddies in the flow and model the smallest scales. This makes it a more accurate but much more computationally costly method for simulations of turbulent flows. Hybrid methods of RANS and LES exist, that behave as RANS methods near walls and further away as LES.

Favre-averaging

FANS methods are most commonly used for the simulation of turbulent, compressible flows and therefore standard practice for turbomachinery analysis. In the derivation of the FANS equations, all dynamical variables except the static pressure and density are Favre-decomposed. A variable $\xi(\vec{x},t)$ is Favre-decomposed as

$$\xi(\vec{x},t) = \widetilde{\xi(\vec{x})} + \xi''(\vec{x},t)\,, \tag{2.40}$$

into the Favre-mean $\widetilde{\xi(\vec{x})}$ and a fluctuating part $\xi''(\vec{x},t)$. The Favre-average $\widetilde{\xi(\vec{x},t)}$ is defined as the density weighted Reynolds-average $\overline{\xi(\vec{x},t)}$

$$\widetilde{\xi(\vec{x},t)} = \frac{\overline{\rho\xi}}{\overline{\rho}} \quad \text{with} \quad \overline{\xi(\vec{x},t)} = \overline{\overline{\xi(\vec{x})} + \xi'(\vec{x},t)} = \overline{\xi(\vec{x})}\,. \tag{2.41}$$

Here, $\xi'(\vec{x},t)$ is the fluctuating part of the Reynolds-decomposition. The fluctuating parts satisfy

$$\overline{\xi'(\vec{x},t)} = 0 \quad \text{and} \quad \widetilde{\xi''(\vec{x},t)} = 0 \quad \Leftrightarrow \quad \overline{\rho\xi''} = 0\,. \tag{2.42}$$

Favre-decomposition and averaging the compressible Navier-Stokes equations yields the FANS equations. Implemented in TRACE, they read [33]

$$\text{continuity} \quad \frac{\partial\overline{\rho}}{\partial t} + \frac{\partial}{\partial x_i}\left(\overline{\rho}\widetilde{u}_i\right) = 0 \tag{2.43}$$

$$\text{momentum} \quad \frac{\partial}{\partial t}\left(\overline{\rho}\widetilde{u}_i\right) + \frac{\partial}{\partial x_j}\left(\overline{\rho}\widetilde{u}_j\widetilde{u}_i\right) = - - \frac{\partial\overline{p}}{\partial x_i} + \frac{\partial}{\partial x_j}\left[\overline{\tau_{ij}} - \overline{\rho u_i'' u_j''}\right] + \overline{\rho}\widetilde{b}_i \tag{2.44}$$

$$\begin{aligned} \text{energy} \quad & \frac{\partial}{\partial t}\left[\overline{\rho}\left(\widetilde{e} + \frac{\widetilde{u}_i\widetilde{u}_i}{2} + \frac{\widetilde{u_i''u_i''}}{2}\right)\right] + \frac{\partial}{\partial x_j}\left[\widetilde{u}_j\overline{\rho}\left(\widetilde{h} + \frac{\widetilde{u}_i\widetilde{u}_i}{2} + \frac{\widetilde{u_i''u_i''}}{2}\right)\right] = \\ & \frac{\partial}{\partial x_j}\left[-\overline{q_j} - \overline{\rho}\widetilde{u_j''h''} + \widetilde{\tau_{ij}u_i''} - \frac{1}{2}\overline{\rho}\widetilde{u_j''u_i''u_i''}\right] + \\ & \frac{\partial}{\partial x_j}\left[\widetilde{u}_i\left(\overline{\tau_{ij}} - \overline{\rho u_i''u_j''}\right)\right] + \overline{\rho}\widetilde{b}_i\widetilde{u}_i \end{aligned} \tag{2.45}$$

$k-\omega$ turbulence model

Compared to the Navier-Stokes equations, additional terms $\overline{\rho u_i'' u_j''}$, $\widetilde{u_i''u_i''}$, $\overline{\rho}\widetilde{u_j''h''}$, $\widetilde{\tau_{ij}u_i''}$ and $\overline{\rho}\widetilde{u_j''u_i''u_i''}$ arise. These terms depend on the fluctuating variables and incorporate the effects of turbulence. Additional relations must be utilized to close the system of equations. The turbulence terms are modeled using mean flow quantities. Most commonly used methods rely on the concept of eddy viscosity, relating the turbulence stresses in the first term to the mean flow [37]

$$\overline{\rho u_i'' u_j''} = \mu_t \left(\frac{\partial \widetilde{u_i}}{\partial x_j} + \frac{\partial \widetilde{u_j}}{\partial x_i} \right) - \frac{2}{3} \overline{\rho} k \,, \tag{2.46}$$

introducing the turbulent eddy viscosity μ_t and the turbulent kinetic energy

$$k = \frac{1}{2} \Big(\sum \widetilde{u_i'' u_i''} \Big) \,. \tag{2.47}$$

The $k - \omega$ turbulence model [38] relates μ_t and k via the specific dissipation rate ω

$$\mu_t = \rho \frac{k}{\omega} \,. \tag{2.48}$$

The variables k and ω are calculated using transport equations

$$\frac{\partial (\overline{\rho} k)}{\partial t} + \frac{\partial (\overline{\rho} k \widetilde{u_j})}{\partial x_j} = \overline{\tau}_{ij} \frac{\partial \widetilde{u_i}}{\partial x_j} - \beta_k \overline{\rho} k \omega + \frac{\partial}{\partial x_j} \left((\mu + \sigma_k \mu_t) \frac{\partial k}{\partial x_j} \right) \tag{2.49}$$

$$\frac{\partial (\overline{\rho} \omega)}{\partial t} + \frac{\partial (\overline{\rho} \omega \widetilde{u_j})}{\partial x_j} = \alpha \frac{\omega}{k} \overline{\tau}_{ij} \frac{\partial \widetilde{u_i}}{\partial x_j} - \beta_\omega \omega^2 + \frac{\partial}{\partial x_j} \left((\mu + \sigma_\omega \mu_t) \frac{\partial w}{\partial x_j} \right) \tag{2.50}$$

with $\alpha = \frac{5}{9}$, $\beta_k = 0.075$, $\beta_\omega = 0.09$, $\sigma_k = 0.5$ and $\sigma_\omega = 0.5$ as closure coefficients. The term $\overline{\rho} \widetilde{u_j'' h''}$ is related to the turbulent heat flux and the term $\frac{1}{2} \overline{\rho} \widetilde{u_j'' u_i'' u_i''} - \widetilde{\tau_{ij} u_i''}$ equals the diffusion term in equation 2.49. There exist various modifications for the turbulence models to incorporate the effects of rotation and compressibility as well as a fix for the stagnation point anomaly. For brevity, they are not described here.

2.3.2. Frequency domain methods

Unsteady periodic flows can be solved in the time domain as well as in the frequency domain. Frequency domain methods allow to transfer an unsteady periodic problem into the frequency domain, greatly reducing computational effort, while maintaining accuracy. The derivation of the discretized equations for both time and frequency domain methods starts with the rewritten form of the FANS equations

$$\frac{\mathrm{D} \vec{\boldsymbol{Q}}}{\mathrm{D} t} + \vec{\boldsymbol{R}} \Big(\vec{\boldsymbol{Q}}, \vec{x}, \dot{\vec{x}} \Big) = 0 \,, \tag{2.51}$$

where $\vec{\boldsymbol{Q}}$ represents the state vector and $\vec{\boldsymbol{R}}$ sums up the fluxes and source terms. Under the assumption that the unsteady aerodynamics are periodic with a frequency ω, the state space vector can be expressed as a Fourier series [39]

$$\vec{\boldsymbol{Q}}\left(t, \vec{x}\right) = \mathrm{Re}\left(\sum_{g=0}^{H} \hat{\vec{\boldsymbol{Q}}}_h\left(\vec{x}\right) e^{ih\omega t}\right), \tag{2.52}$$

with H being the number of harmonics used to construct the state space vector. For $H \rightarrow \infty$, the Fourier series converges toward the time domain solution. As the number of included harmonics increases, the computational costs grow. Often a small number of harmonics is sufficient to resolve all relevant physics, greatly reducing computational effort. Inserting equation (2.52) into equation (2.51) yields

$$ih\omega\hat{\vec{\boldsymbol{Q}}}_h + \vec{\boldsymbol{R}}_h\left(\vec{\boldsymbol{Q}}, \vec{x}, \dot{\vec{x}}\right) = 0\,. \tag{2.53}$$

Note that $\vec{\boldsymbol{R}}_h$ depends not only on the h-th harmonic of $\vec{\boldsymbol{Q}}$, but on all harmonics $\vec{\boldsymbol{Q}}_h$ due to the nonlinearity of the Navier-Stokes equations [39].

Linear methods

For small amplitudes, the displacement $\vec{x}$ and the state space vector $\vec{\boldsymbol{Q}}$ can be linearized. The variables are separated into a steady mean value $\bar{\vec{x}}$ or $\bar{\vec{\boldsymbol{Q}}}$ and a small time dependent disturbance $\delta\vec{x}$ or $\delta\vec{\boldsymbol{Q}}$

$$\vec{x} = \bar{\vec{x}} + \delta\vec{x}(t, \bar{\vec{x}}) \quad \text{and} \quad \vec{\boldsymbol{Q}} = \bar{\vec{\boldsymbol{Q}}} + \delta\vec{\boldsymbol{Q}}(t, \bar{\vec{\boldsymbol{Q}}})\,. \tag{2.54}$$

Only the first harmonic is considered in the unsteady disturbance terms $\delta\vec{x}$ or $\delta\vec{\boldsymbol{Q}}$ and $\vec{\boldsymbol{R}}\left(\vec{\boldsymbol{Q}}, \vec{x}, \dot{\vec{x}}\right)$ is approximated by a Taylor series of first order. This yields the linearized unsteady representation of the FANS equations in the frequency domain [40]

$$i\omega\hat{\vec{\boldsymbol{Q}}} + \left.\frac{\partial\vec{\boldsymbol{R}}}{\partial\vec{\boldsymbol{Q}}}\right|_{\bar{\vec{\boldsymbol{Q}}}} \cdot \hat{\vec{\boldsymbol{Q}}} + \left.\frac{\partial\vec{\boldsymbol{R}}}{\partial\vec{x}}\right|_{\bar{\vec{x}}} \cdot \hat{\vec{x}} + i\omega\left.\frac{\partial\vec{\boldsymbol{R}}}{\partial\dot{\vec{x}}}\right|_{\dot{\bar{\vec{x}}}} \cdot \hat{\vec{x}} = 0\,. \tag{2.55}$$

This approach was first introduced by Hall and Clark for the analysis of flutter in turbomachinery [41]. The linearization makes this approach computational efficient, but it is only valid for small displacements and linear physics, because no higher harmonics are resolved.

Harmonic Balance methods

To retain nonlinear physics, the term $\vec{\boldsymbol{R}}_h\left(\vec{\boldsymbol{Q}}, \vec{x}, \dot{\vec{x}}\right)$ in equation (2.53) must not be linearized. Kersken et al. use

$$\vec{\boldsymbol{R}}_h\left(\vec{\boldsymbol{Q}}, \vec{x}, \dot{\vec{x}}\right) = \mathscr{F}\left(\vec{\boldsymbol{R}}_h\left(\mathscr{F}^{-1}\left(\vec{\boldsymbol{Q}}, \vec{x}, \dot{\vec{x}}\right)\right)\right) \tag{2.56}$$

in their implementation in TRACE [39]. Here, $\mathscr{F}$ denotes the Discrete Fourier Transformation and $\mathscr{F}^{-1}$ its inverse operation. While equation (2.56) is solved in the frequency domain, the harmonics of $\hat{\vec{\boldsymbol{Q}}}_h$ are reconstructed in the time domain. This makes it a hybrid time- and frequency-domain method, which takes advantage of nonlinear time-domain flux functions without the need to explicitly model the coupling terms between the harmonics, as well as the highly accurate nonreflecting boundary conditions formulated in the frequency domain.

2.3.3. Energy Method

For flutter analysis of turbomachinery there exist many different methods, varying in complexity and fidelity. Most methods can be grouped into two main approaches, modeling the interaction between fluid and structure [42]

Classical Methods where fluid and structural domain remain uncoupled. The structural eigenmodes are computed and used as boundary conditions of the fluid domain. This is called Prescribed Motion Approach. The aerodynamic forces do not influence the structural behavior.

Integrated Methods where fluid and structure domain are coupled. In Partially Integrated Methods both domains are solved separately, but information of each domain is exchanged between both domains at each time step and used as boundary conditions. Fully Integrated Methods combine structural and fluid domain to solve them together at each time step.

Classical methods remain the most commonly used approach due to their computational efficiency. For most traditional compressor and fan blades, manufactured from metals, structural damping is low and a high mass ratio of structural mass and displaced fluid mass leads to decoupling of eigenmodes, as described in section 2.2.2.3. Note that modern lightweight designs increasingly require a coupled approach for accurate flutter prediction, as aerodynamic forces can significantly alter the structural eigenmodes and frequencies [43].

The most commonly used classical method is the Energy Method introduced by Carta in 1967 [44]. The aeroelastic stability of each undamped structural eigenmode shape is analyzed by computing the aerodynamic work performed by the unsteady aerodynamic forces that are excited due to the harmonic oscillation.
Modern flutter analysis uses FEA and CFD tools to compute the eigenmodes and the aerodynamic forces. First, a modal analysis using FEA is conducted to find the structural eigenmodes and eigenfrequencies of the blade. Second, the eigenmodes and eigenfrequencies of the structure are used as boundary conditions in an unsteady CFD simulation. The solution of the CFD simulation is used to calculate the aerodynamic work transferred from fluid to blade or vice versa. If the fluid imparts work on the structure, flutter occurs. For one modeshape r, the aerodynamic work over one oscillation period T_r can be calculated as the time integral of the real valued aerodynamic power

$$W_r = \int_0^{T_r} \Re\Big(P_r(t)\Big)\,\mathrm{d}t = \int_0^{T_r} \Re\Big(\dot{\vec{x}}_r(t)\Big) \cdot \Re\Big(\vec{F}_r(t)\Big)\,\mathrm{d}t\,. \tag{2.57}$$

Since the deformation vector as well as its velocity are harmonic, the aerodynamic response $\vec{F}_r$ is also assumed to be harmonic. For eigenmode r with phase angles φ_{st} and φ_{fl}, the velocity and aerodynamic forces can be expressed as

$$\dot{\vec{x}}_r = i\omega_r|\hat{\vec{\psi}}_r|\, e^{i\varphi_{st}}\, e^{i\omega_r t} \quad \text{and} \quad \vec{F}_r = |\hat{\vec{F}}_r|\, e^{i\varphi_{fl}}\, e^{i\omega_r t}\,. \tag{2.58}$$

Inserting equation (2.58) into equation (2.57), and calculating the real parts using the complex conjugate, yields

$$W_r = \pi|\hat{\vec{\psi}}_r|\,|\hat{\vec{F}}_r|\sin\left(\Delta\varphi\right), \tag{2.59}$$

with the difference between the phase angles $\Delta\varphi = \varphi_{fl} - \varphi_{st}$. The TRACE code used for all simulations in this thesis, determines the displacement by the time integration of the displacement velocity of the blade. Following, it the phase angle of the displacement velocity $\varphi_{st,vel.}$, that is 90° shifted from φ_{st}, will be used. TRACE calculates the aerodynamic work as

$$W_r = \pi|\hat{\vec{\psi}}_r|\,|\hat{\vec{F}}_r|\cos\left(\Delta\varphi_{vel.}\right). \tag{2.60}$$

The aerodynamic forces $\hat{\vec{F}}_r$ are calculated via CFD simulation as integration of the unsteady pressure forces p_η over each finite element η of the blade

$$\hat{\vec{F}}_r = \int_\eta \left(p_\eta \, \vec{n}_\eta\right)_r \, \mathrm{d}A_\eta \, . \tag{2.61}$$

Since $|\hat{\vec{\psi}}_r|$ and $|\hat{\vec{F}}_r|$ are magnitudes of their corresponding complex functions, the sign of the aerodynamic work, and thus the sign of the aerodynamic damping, only depends on the phase difference between both displacement and aerodynamic forces.

For comparability between different analyses with varying initial and boundary conditions, the logarithmic decrement of the blade oscillations is used. The logarithmic decrement of the oscillation amplitudes over one period is defined as

$$\Lambda_r = \ln\left(\frac{q_r(t)}{q_r(t+T)}\right) . \tag{2.62}$$

The total energy in the system is the sum of kinetic and potential energy

$$E^r_{\text{tot}} = E^r_{\text{kin}} + E^r_{\text{pot}} = E^r_{\text{pot, max}} = \frac{1}{2}\widetilde{k}_r \, q_r^2 \, . \tag{2.63}$$

Over one period, the energy of the system changes due to the aerodynamic work W_r. The ratio of displacement amplitudes is equal to the square root of the ratio of total energy over one period, following equation (2.63). With the assumption of small aerodynamic work compared to the total energy, the displacement ratio can be related to the energy as

$$\frac{E_{\text{tot}}(t)}{E_{\text{tot}}(t+T)} = \left(\frac{q_r(t)}{q_r(t+T)}\right)^2 = \frac{E_{\text{tot}}(t)}{E_{\text{tot}}(t) + W_r} \approx \left(1 + \frac{W_r}{E_{\text{tot}}(t)}\right)^{-1} . \tag{2.64}$$

The logarithmic decrement can be computed using the energy in the system and the aerodynamic work that adds or subtracts energy over one period as

$$\Lambda_r \approx -\frac{W_r}{\widetilde{m}_r \, \omega_r^2 \left(q_r(t)\right)^2} \, . \tag{2.65}$$

3. Simulations

The simulations and their analysis will focus on the physical mechanisms causing transonic stall flutter in a two-dimensional NACA3506 cascade. A two-dimensional analysis is performed to analyze many more operating points than would be possible using a three-dimensional setup. Also, the analysis is simplified since no three-dimensional effects are present. These effects on flutter onset can be incorporated and studied in future works.
The work in this thesis can be divided into four steps:

1. **Mesh generation and sensitivity study**: Four meshes (G_{-1}, G_0, G_{+1}, G_{+2}) with halved grid spacings between refinement levels are created. A mesh sensitivity study on multiple operating points is conducted, where steady-state and unsteady flutter simulations are performed on all four grids using non-linear (steady simulations), linearized and Harmonic Balance (unsteady simulations) solvers. Following, the meshes for further simulations are chosen.
2. **Compressor map**: Non-linear steady-state simulations on mesh G_{+1} are performed to generate the compressor map.
3. **Flutter map** The linearized solver is used to run unsteady flutter simulations on mesh G_{+1} over the entire compressor map to create a map of flutter stability overlaid on the compressor map. This is further called flutter map.
4. **Detailed flutter investigation** The Harmonic Balance solver is used to perform unsteady flutter simulations on mesh G_{+2} at a selection of operating points in the transonic regime, near stall. The physical mechanisms causing transonic stall flutter are investigated.

All simulations as well as pre- and postprocessing for this thesis are performed using the DLR in-house simulation system TRACE (Turbomachinery Research Aerodynamic Computational Environment), developed at the DLR Institute of Propulsion Technology [33]. TRACE consists of the modules PREP, TRACE and POST

for preprocessing, solving and postprocessing respectively. PREP maps the blade eigenmodes onto a CFD grid for aeroelastic analysis. The TRACE module includes nonlinear CFD solvers in the time and frequency domain and a linearized solver in the frequency domain. POST can be used as analysis tool for all TRACE simulations. Meshes are created with the DLR in-house code PyMesh [45]. It generates structured multiblock meshes for use in turbomachinery flow analysis.
Steady-state simulations and most flutter analyses, using the linearized solver on grids G_{-1}, G_0 and G_{+1}, are performed on local workstations with 10 CPU cores. The more computationally expensive flutter simulations on G_{+2}, as well as all simulations using the non-linear Harmonic Balance solver, are performed on the CARO cluster, utilizing 52 cores for each simulation.

The geometry and simulation domain are described in section 3.1. The numerical setup, including meshing, is detailed in section 3.2 and the results of the mesh sensitivity study are presented in chapter 4.

3.1. Geometry and domain

Table 3.1.: Geometry dimensions.

Geometry	NACA3506; linear cascade; N=20 blades
Chord length	$c_B = 77\,\mathrm{mm}$
Stagger angle LE-TE	$\beta = 40°$
Pitch	$\tau = 56.55\,\mathrm{mm}$

A NACA3506 blade profile was selected from an existing compressor annular cascade, the 'Ringgitterprüfstand' of the DLR Institute of Aeroelasticity. The model has 20 prismatic blades and was subject of several experimental and numerical aeroelastic investigations [5, 46, 47, 48]. The two-dimensional geometry was extracted as a slice at 50 % span of a three-dimensional annulus with an 18 m radius. This ensures an easy translation of the three-dimensional geometry into two dimensions. The radius is 100 times larger compared to the original geometry. Consequently, the rotational rates are scaled by $\frac{1}{100}$. A close-up view of the three-dimensional numerical model is presented in figure 3.1. The geometrical parameters are given in table 3.1. The two-dimensional cascade and the simulation domain are shown in figure 3.2a. Only one blade is included in the simulation domain and the axial symmetry is utilized as periodic boundary condition.

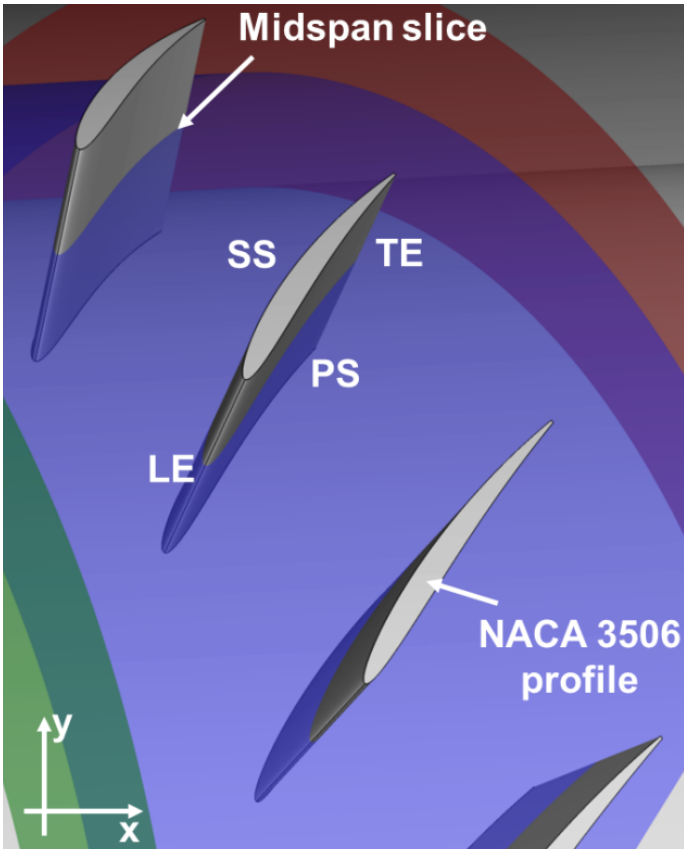

Figure 3.1.: Three-dimensional geometry with midspan slice (purple) for extraction of two-dimensional linear cascade geometry [5].

3.2. Numerical setup

The single-passage cascade is shown in figure 3.2a. The mesh setup is described in 3.2.1. FANS equations are employed for all CFD simulations. Turbulence is modeled using the $k-\omega$ turbulence model [38] with modifications for compressible flows [49], rotational effects (Bardina) [50] and the stagnation point anomaly fix (Kato Launder) [51]. The near-wall mesh is finely resolved with $y^+ < 1$ for the first cell height. At the inlet, total pressure and total temperature as well as turbulence levels are prescribed, whereas at the outlet, the static pressure is defined for every operating point. Rotational rates and eigenmode motions (for unsteady simulations) are prescribed as boundary conditions for the blades. Axial symmetry is exploited to simplify the setup into a single passage with periodic boundaries. In subsections 3.2.2 and 3.2.3, the simulation setup and boundary conditions for steady-state and unsteady simulations are discussed.

3.2.1. Meshes

All meshes are constructed as a structured mesh with an O-C-H topology. The boundary layer is resolved with the O-grid constructed as an inflation layer. Around the O-grid, the C-grid connects the boundary layer mesh with the bulk mesh, which is resolved using three H-grids for the inlet, passage and outlet. The meshing blocks are depicted in figure 3.2a.

To quantify the mesh sensitivity for steady-state and unsteady flutter simulations and to choose a suitable grid for the investigations in this thesis, four meshes G_{-1}, G_0, G_{+1}, G_{+2} are generated, where grid spacing halves for each refinement level. In figure 3.2b, the base mesh G_0 is depicted.
First, grid G_0 was created, based on the grid used in a previous investigation on the two-dimensional NACA3506 cascade [5]. With this grid, preliminary simulations are performed to choose boundary layer resolutions and the numerical setup. These simulations reproduced findings of Mueller et al. [52], who reported mesh sensitivity of unsteady flutter simulations for y^+ values below $y^+ \approx 1$ and mesh independence for $y^+ \approx 0.1$. As a result, a non-dimensional wall distance of $y^+ \approx 0.1$ is chosen. O-grids for all four meshes G_{-1}, G_0, G_{+1}, G_{+2} have the same first cell height. Meshes G_{-1}, G_0 and G_{+1} have the same number of layers and use the same expansion ratio. They only differ by their chordwise resolution, that doubles with each refinement

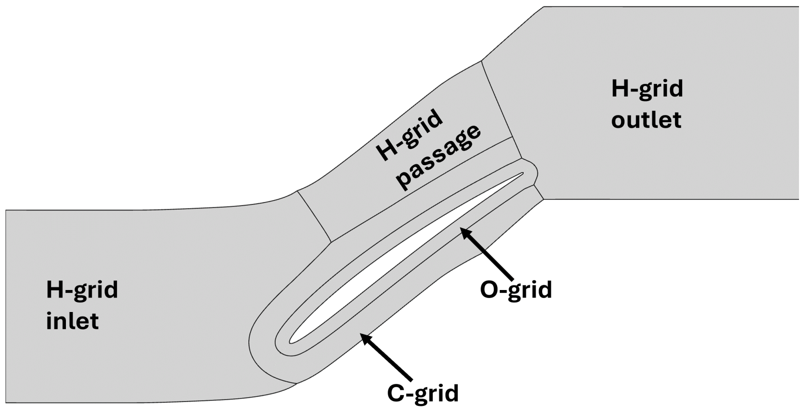

(a) Simulation domain with meshing blocks.

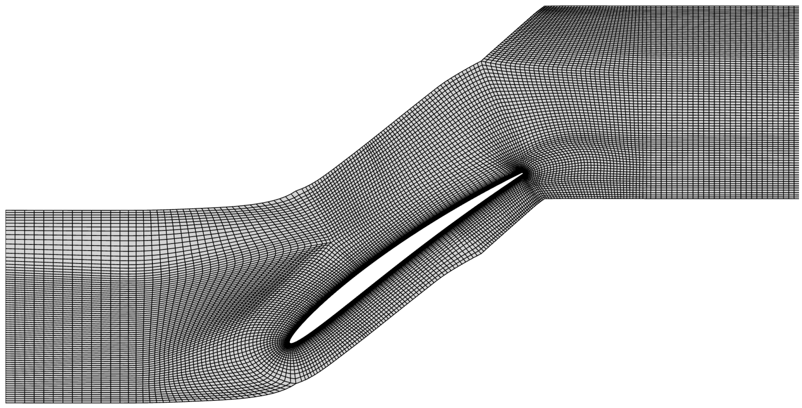

(b) Base mesh, G_0.

Figure 3.2.: Simulation domain and base mesh.

level. O-grid G_{+2} has a lower expansion ratio and double the number of layers to achieve a lower cell height for the last layer. This ensures a smooth transition to the C-grid. The cell counts are given in table 3.2 and detailed grid resolutions can be looked up in the appendix A.1. More pictures of the grids are placed in the appendix in figures A.1 and A.2.

Table 3.2.: Mesh cell counts.

Grid	G_{-1}	G_0	G_{+1}	G_{+2}
Cell count	8992	23568	71280	273804

For the simulations, grids G_{-1}, G_0 and G_{+1} are divided into 17 sections (O-grid 8, C-grid 2, H-inlet 2, H-passage 1, H-outlet 4) and G_{+2} is divided into 52 sections (O-grid 16, C-grid 8, H-inlet 8, H-passage 4, H-outlet 16) for parallelization.

3.2.2. Steady-state simulations

The steady-state simulations are computed using the non-linear formulation of the FANS equations. Turbulence modeling is applied as described in section 3.2. For spatial discretization, the Fromm scheme is combined with the van Albada Sqr limiter to obtain second-order accuracy. The CFL number starts at 1 and ramps up to 4 during the first 1000 iterations. The pseudo-time scheme is solved via a predictor-corrector method. All TRACE solver settings are shown in figure A.3 in the appendix. Inlet and outlet boundary conditions use a nonreflecting formulation for aeroelastic analysis [53]. The blades use the rotational rate, scaled by the factor $\frac{1}{100}$ as described in section 3.1, as no-slip boundary condition. No wall modeling is applied. The operating points are defined by the rate of rotation (RoR) and the backpressure at the outlet. The range of boundary conditions is given in table 3.3. Convergence is defined as changes of mass flow, pressure ratio and efficiency of less than 0.01 % and a residual L1 of less than 10^{-5} over 100 iterations.

Table 3.3.: Boundary conditions for steady-state simulations.

Rotational rate	$69.2 - 145.32\,\frac{\text{rev}}{\text{min}}$
	$50 - 105\,\%$
Inlet total pressure	137500 Pa
Inlet total temperature	295 K
Inlet turbulence intensity	1 %
Inlet eddy length scale	$9 \cdot 10^{-5}$ m
Outlet static pressure	$80000 - 163500$ Pa

3.2.3. Flutter simulations

Unsteady flutter simulations are performed using the time-linearized solver and Harmonic Balance solver. Both use the solution of the steady-state simulations as initialization. A prescribed motion method applies an eigenmode and an IBPA as boundary condition for the harmonic motion of the blade. No coupling between fluid and structure is assumed in the simulations. Flutter stability is evaluated using the Energy Method, introduced in section 2.3.3. The periodicity of the blade oscillations is exploited to solve the problem in the frequency domain.

In the following, the eigenmode shape are described and the simulation setups for the linearized solver and the Harmonic Balance solver are presented.

3.2.3.1. Eigenmodes and modeshapes

Table 3.4.: Mode shape parameters.

Name	Frequency	Amplitude
1B	100 Hz	$x_0 = \pm 0.035\,\%$
1T	200 Hz	$\alpha_0 = \pm 0.07°$

The eigenmodes of the blades are not derived using FEM simulations, but are synthetically produced. They are similar to other blades and past investigations of the NACA3506 cascade [5, 54]. Two eigenmode shapes are investigated independently, the first bending mode (1B) and the first torsion mode (1T). Their frequency and amplitude are given in table 3.4. The amplitudes were chosen to be small enough to not cause non-linear effects, following the results of an analysis of the influence of oscillation amplitude on the aerodynamic damping [5]. The first bending mode oscillates perpendicular to the stagger angle; the first torsion mode pitches around the midpoint of the camber line. The mode shapes are schematically depicted in figure 3.3. Eigenfrequencies are assumed to be constant.

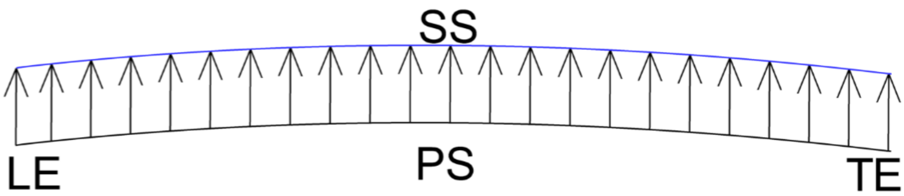

(a) Bending mode 1B perpendicular to stagger angle.

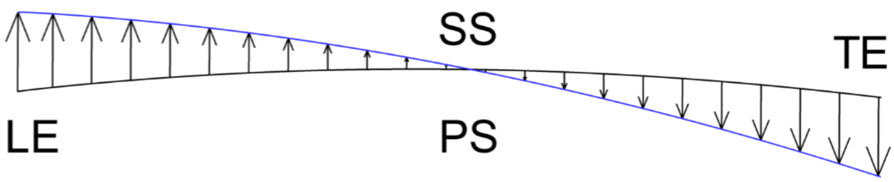

(b) Torsion mode 1T pitching around an axis at 50 % length of the camber line.

Figure 3.3.: Mode shapes projected on camber line [5].

3.2.3.2. Time-linearized simulations

The flutter map is created using the time-linearized solver in TRACE. The steady-state mean flow is first computed using non-linear FANS equations and the linearized solver predicts the unsteady harmonic perturbations. Exploiting the harmonic nature, the unsteady simulation is solved in the frequency domain. The linearized solver does not compute the turbulence variations, they stay constant at the value of the steady-state flow field during the unsteady simulations. This is called Frozen ν approach. The governing equations are solved by a parallel generalized minimal residual solver (GMRES). The linear equation system is preconditioned by a m-step successive overrelaxation scheme (SSOR). The algorithm is restarted every 500 iterations. For spatial discretizations, the limiter is turned off for the linearized simulations. All solver settings are given in figure A.4 in the appendix. Simulations are converged if global aerodynamic work changes less than 0.01 % and residual L2 is lower than 10^{-4} over 250 iterations.

3.2.3.3. Harmonic Balance simulations

The investigations of flutter mechanisms are carried out with the Harmonic Balance module of TRACE. The Harmonic Balance solver is a hybrid frequency-time-domain approach as introduced in section 2.3.2. Flow solutions are reconstructed from the harmonics at discrete time steps to evaluate the non-linear state space function in the time domain. A Discrete Fourier Transformation transforms the residual function to solve the system of equations in the frequency domain.
The physical models and spatial discretization used in the non-linear steady-state simulations are retained in the Harmonic Balance simulations. Following the findings of Chenaux et al. [55], five harmonics are included with a sampling rate of five points for the highest harmonic. The 0th harmonic corresponds to the steady mean flow. Turbulence transport equations are not solved in higher harmonics to help achieve convergence, since no significant influence on the results was found in preliminary simulations. The CFL number ramps up from 0.4 to 2 after 10000 iterations. All solver settings are shown in figure A.5 in the appendix. For the finer meshes G_{+1} and G_{+2}, the strict convergence criteria for global aerodynamic work of less than 0.01 % over 250 iterations, used for the time-linearized simulations, can not be met. In fact, for some mode and IBPA combinations, global aerodynamic work diverges. Consequently, convergence for the Harmonic Balance simulations is defined as changes of less than 0.5 % of global aerodynamic work and residual L1 under 10^{-5} over 250 iterations. This increases the possible uncertainties of the results, but does not change the qualitative statements of the results.

4. Mesh sensitivity study

Mesh sensitivity studies on meshes G_{-1}, G_0, G_{+1} and G_{+2} are performed for steady-state simulations using the non-linear solver and unsteady flutter simulations using the linear and Harmonic Balance solvers.

4.1. Mesh sensitivity for steady-state simulations

Mesh sensitivity for the non-linear steady-state FANS calculations is evaluated for speed lines of 65 %, 85 %, 95 % and 105 % rate of rotation. They are plotted in figure 4.1. For most portions of the speed lines, overall differences between the four meshes in mass flow and pressure ratio are below 1 %. Differences increase for higher rotational rates, near stall and in the choke region. Increasing refinement levels lead to stalling at higher backpressures, as can be seen in figure 4.1. Steady-state simulations are computed on the local workstation utilizing 10 CPU cores. Typical run times for all grids are given in table 4.1.

Table 4.1.: Simulation run times for steady-state simulations (on workstation).

Grid	G_{-1}	G_0	G_{+1}	G_{+2}
Cell count	8992	23568	71280	273804
Typical run time [min]	3	6.5	20	80

Due to the diminishing increase in accuracy of simulations on G_{+1} compared to G_{+2}, but quadrupling of runtime, G_{+1} is chosen for steady-state simulations to create the flutter map. With a typical run time of 20 min and approximately 240 simulations, this will take 80 h on one workstation. Since 4 workstations are available, overall runtime is about one day.

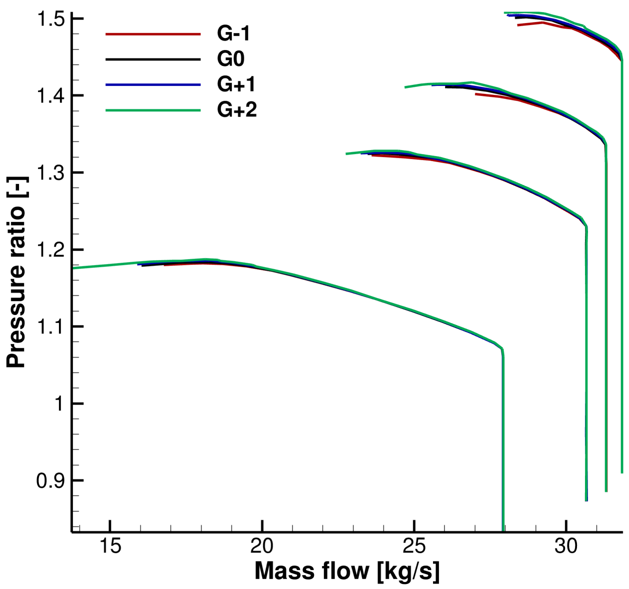

(a) Speed lines 65 %, 85 %, 95 % and 105 %.

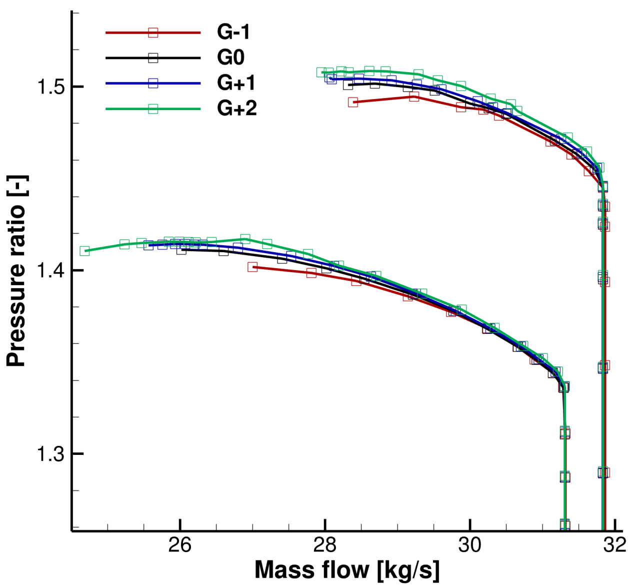

(b) Speed lines 95 % and 105 %.

Figure 4.1.: Mesh sensitivity of pressure ratio and mass flow in steady-state simulations.

4.2. Mesh sensitivity for flutter simulations

Mesh sensitivity for unsteady flutter simulations is evaluated for the operating points marked in figure 4.2. In this work, plots for four points RoR = 65 %, $p_2 = 138000$ Pa, RoR = 75 %, $p_2 = 149000$ Pa, RoR = 75 %, $p_2 = 150500$ Pa and RoR = 95 %, $p_2 = 154500$ Pa are shown and discussed. They are chosen to display the general results and lessons learned from the mesh sensitivity study and preliminary simulations. Aerodynamic damping as logarithmic decrement is plotted against the IBPAs for unsteady simulations using the linear and Harmonic Balance solver in figures A.6, 4.3, 4.4 and A.7. For brevity, only 4.3 and 4.4 are displayed in this section, A.6 and A.7 can be seen in the appendix A.4.

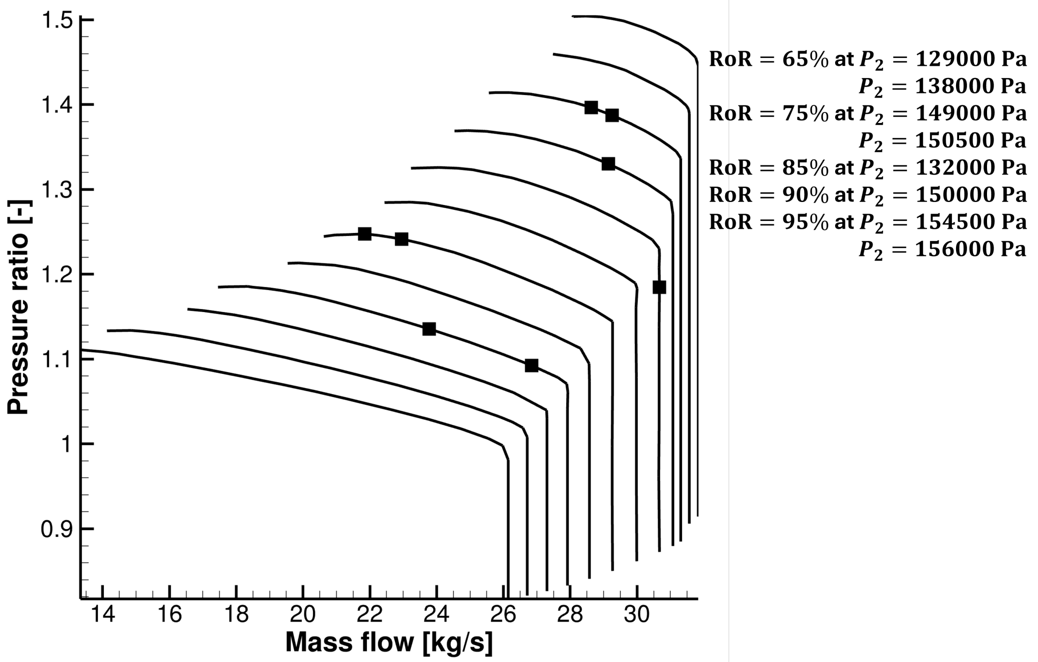

Figure 4.2.: Selection of operating points for the mesh sensitivity study of aerodynamic damping for unsteady flutter simulations.

Flutter prediction and forecast of the most unstable IBPA is dependent on the solver and mesh resolution. Higher rotational rates, more complex flow regimes and increasing aeroelastic instability increase the sensitivity of flutter prediction to mesh refinement and solvers.

For the operating point of $p_2 = 138000$ Pa on the 65 % speed line, plotted in figure A.6, flutter prediction shows little mesh sensitivity and the results using the linear

and Harmonic Balance solver show no significant differences. This indicates that little to no non-linearities are present.
For the operating point of $p_2 = 149000\,\mathrm{Pa}$ on the $75\,\%$ speed line in mode 1B (figures 4.3a and 4.3c), both solvers predict no flutter and lowest aeroelastic stability for $\sigma_n = 0°$ on all four meshes. Aerodynamic damping for $\sigma_n \neq 0, +18°, +36°$ differ between all meshes. Using both solvers, mesh convergence cannot be identified. While aerodynamic damping increases for most IBPAs from G_0 to G_{+1} and to G_{+2}, the changes from G_0 to G_{+1} are approximately the same compared to G_{+1} and G_{+2}. Mesh G_{-1} stands out, in that the aerodynamic damping is highest using the Harmonic Balance solver and lies between G_0 and G_{+1} using the linear solver. This may indicate insufficient mesh resolution to accurately capture all relevant physics. In mode 1T, the Harmonic Balance solver predicts unstable behavior for all meshes at $\sigma_n = -126°$. The linear solver predicts instability for meshes G_{-1}, G_0 and G_{+1} with lowest damping at IBPAs $-126°$, $-144°$ and $-126°$ respectively. For the finest mesh, the lowest aerodynamic damping is at $\sigma_n = -108°$, but still positive. The flutter stability shows significant sensitivity to the mesh refinement. For the Harmonic Balance solver, mesh convergence between meshes G_0, G_{+1} and G_{+2} can be observed in figure 4.3b, but again G_{-1} stands out. For the linear solver, no mesh convergence occurs; also G_{-1} stands out as previously observed. Since flutter predictions using the linear and Harmonic Balance solver show only small qualitative and quantitative variations, the problem can be assumed to contain only minor non-linearities.
For the operating point of $p_2 = 150500\,\mathrm{Pa}$ on the $75\,\%$ speed line, shown in figure 4.4, both solvers predict different flutter stability for mode 1B on G_{+1} and G_{+2}. Results on G_0 using Harmonic Balance and on G_{-1} and G_0 using the linear solver show large differences to those on the finer meshes. Comparing aerodynamic damping, significant variations between the meshes can be seen for most IBPAs. Moreover, highest and lowest damping is at different IBPAs compared to G_{+1} and G_{+2}. Note that simulations for $\sigma_n = +36°$ and $\sigma_n = +126°$ for G_0 using Harmonic Balance are not converged. Comparing flutter predictions between both solver on meshes G_{+1} and G_{+2}, qualitative differences can be seen. While the Harmonic Balance solver predicts instability, the linear solver predicts stabile behavior. The linear solver shows little sensitivity between G_{+1} and G_{+2}, while the Harmonic Balance solver predicts different IBPAs with lowest damping ($\sigma_n = +90°$ for G_{+1} and $\sigma_n = +72°$ for G_{+2}). For mode 1T, the Harmonic Solver shows mesh convergence between G_0,

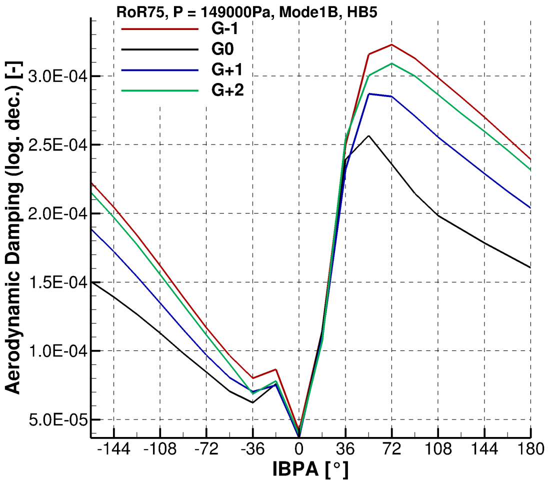

(a) Mode 1B, HB5 solver.

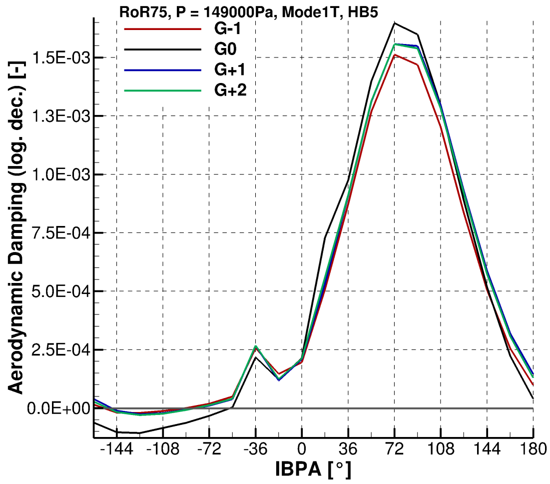

(b) Mode 1T, HB5 solver.

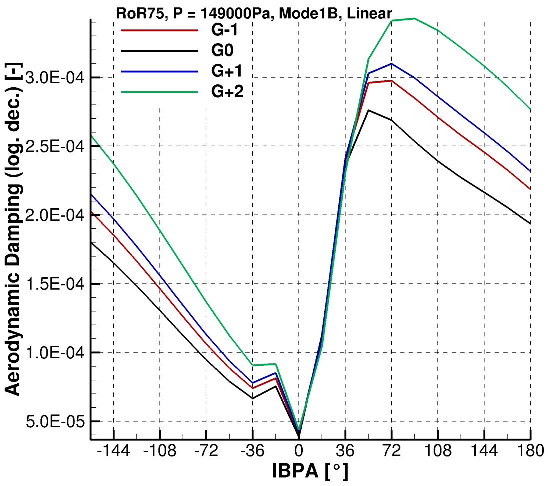

(c) Mode 1B, linear solver.

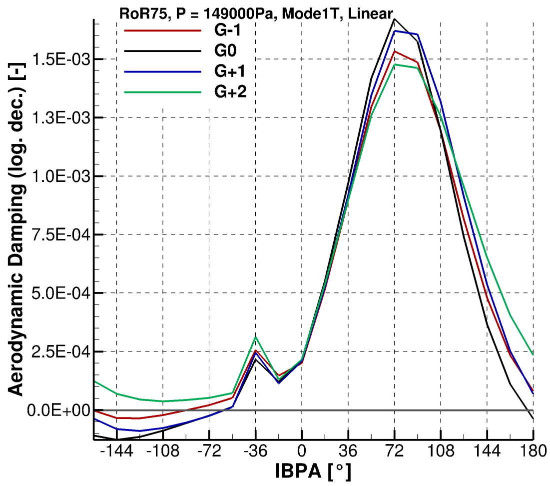

(d) Mode 1T, linear solver.

Figure 4.3.: Mesh sensitivity of aerodynamic damping for unsteady flutter simulations; RoR 75 %, $p_2 = 149000\,\mathrm{Pa}$.

G_{+1} and G_{+2}. On all meshes, instability is predicted. The aerodynamic damping plot calculated via the linear solver on G_0 shows differences to those on other meshes, similarly to mode 1B. Results on G_{+1} and G_{+2} show convergence. Smaller non-linearities seem to be present in the flow in mode 1T compared to mode 1B.

All flutter simulations for the mesh sensitivity study are computed on the CARO cluster, due to the number of simulations (40 per operating point) and simulation

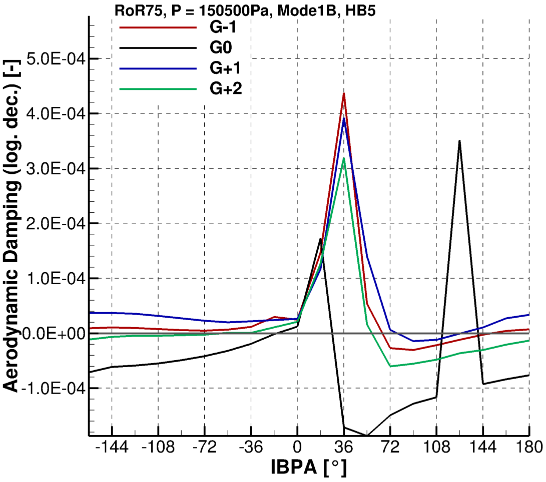

(a) Mode 1B, HB5 solver.

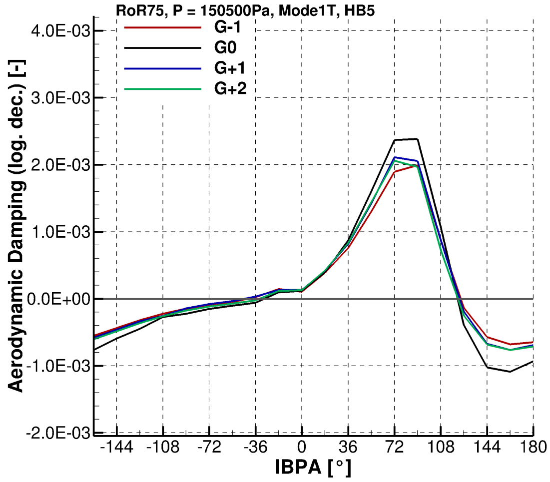

(b) Mode 1T, HB5 solver.

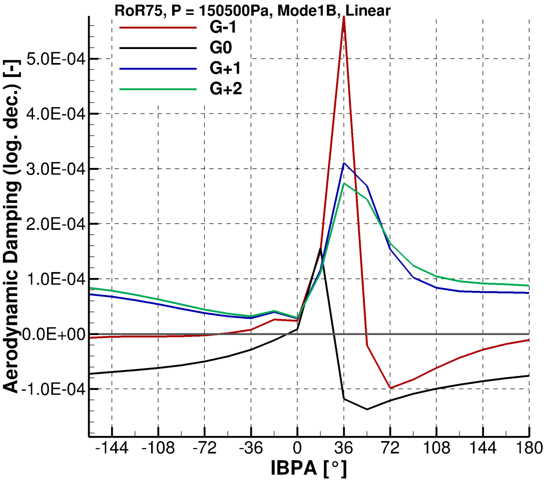

(c) Mode 1B, linear solver.

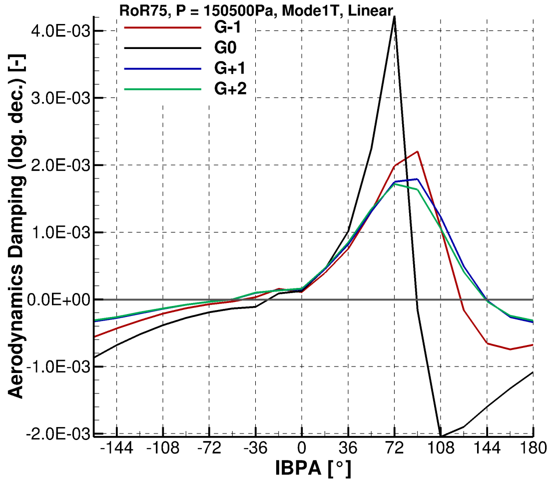

(d) Mode 1T, linear solver.

Figure 4.4.: Mesh sensitivity of aerodynamic damping for unsteady flutter simulations; RoR 75 %, $p_2 = 150500\,\mathrm{Pa}$.

time of each individual simulation. Typical simulation run times for each individual simulation are given in table 4.2.

The results in general show good agreement for aerodynamic damping prediction between meshes G_{+1} and G_{+2} using both solvers. Significant variations are present for complex flow regimes (see figures 4.4a, A.7a, A.7c, A.7d). On meshes G_{-1} and G_0 in some cases, physics are not captured accurately (see figures 4.4a, 4.4c, 4.4d). This rules both meshes out for detailed investigations.

For the creation of the flutter map, the linear solver is chosen with mesh G_{+1}. This is a good compromise between accuracy and speed. Additionally, these simulations are able to be run locally on the workstations, with no time consuming data transfer between workstation and HPC needed. For the detailed investigation, mesh G_{+2} and the Harmonic Balance solver are preferred, because fewer simulations are performed, but accuracy is needed for physical analysis. Since larger meshes benefit more from parallelization, the difference in simulation run time between Harmonic Balance simulations on G_{+1} compared to G_{+2} is small.

Table 4.2.: Simulation run times for unsteady flutter simulations.

Grid	G_{-1}	G_0	G_{+1}	G_{+2}
Cell count	8992	23568	71280	273804
Typical workstation run time, linear solver [h]	0.03	0.12	0.5	2.5
CPU cores used on HPC	16	16	16	52
Typical HPC run time, linear solver [h]	0.02	0.08	0.3	0.4
Typical HPC run time, HB5 solver [h]	1	5	21	27

5. Flutter analysis

For the flutter analysis, first, in section 5.1, the flutter stability over the working range of the compressor is computed and analyzed. Second, in section 5.2, operating points of interest in the transonic stall flutter regime are chosen, to investigate the flutter stability and physical mechanisms of flutter onset in detail. This analysis is performed for the first bending (1B) and first torsion (1T) mode.

5.1. Flutter map

Steady-state simulations using the non-linear CFD solver and unsteady flutter simulations using the linearized solver are performed on mesh G_{+1} to generate a compressor map and display the flutter stability regions over the working range of the compressor in figure 5.1. The speed lines from 50 % to 105 % rotational rate are plotted in 5 % increments. On each speed line, the flutter stability for mode 1B and mode 1T is given.

The torsion mode appears to be more susceptible to flutter onset compared to the bending mode. Near stall, the 1T mode starts to become unstable at lower back-pressures compared to the 1B mode on nearly all speed lines. This is in agreement with the literature [1, 23]. Exceptions are the speed lines 100 % and 105 % (the two lines on the right of the flutter map), where bending flutter occurs first. This may indicate the supersonic bending stall flutter regime mentioned in [1]. In the choked region of the compressor map, flutter in the torsion mode starts to occur at higher compression ratios compared to the bending mode. For rotational rates lower than 70 %, the torsional flutter region extends into the non-choked parts of the compressor map, close to the working line.

For the investigation of flutter mechanisms using the Harmonic Balance solver, the 75 % speed line near stall is chosen. It lies in the transonic stall flutter region.

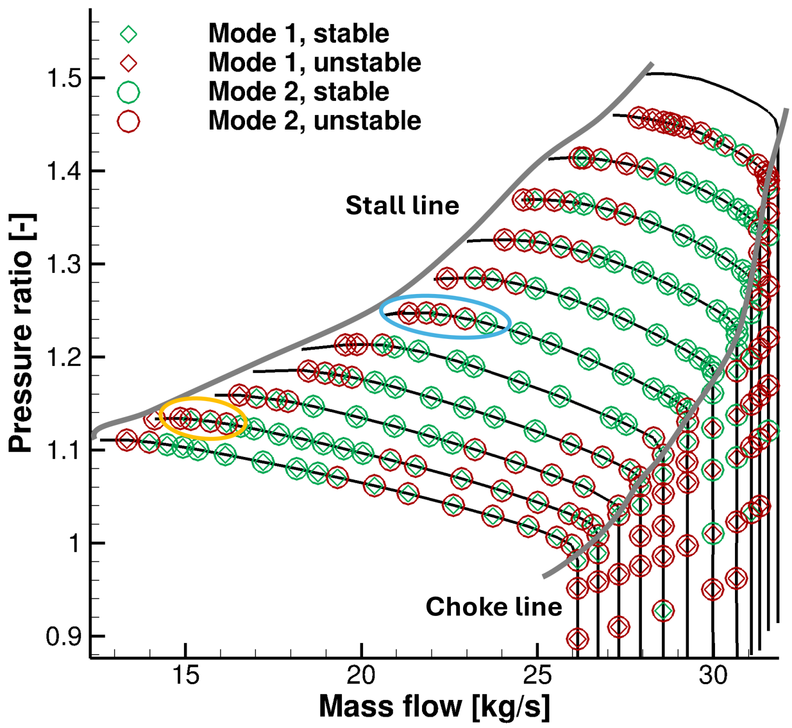

Figure 5.1.: Fluttermap computed with the linear solver on mesh G_{+1}.

The 55 % speed line is used as a comparison with a mainly subsonic flow regime to investigate the effect of the shock. The operating points are marked (blue on the 75 % speed line, yellow on the 55 % speed line) in figure 5.1. The linear solver predicts flutter onset in mode 1B for backpressures starting at 145250 Pa on the 55 % speed line and at 150750 Pa on the 75 % speed line. Flutter in mode 1T starts to arise earlier at 144000 Pa on the 55 % and at 148500 Pa on the 75 % speed line.

5.2. Transonic stall flutter

In figure 5.2, the logarithmic decrement of aerodynamic damping is shown over a range of investigated operating points on the 75 % speed line near stall. The aerodynamic damping decreases with increasing backpressure. For mode 1B, the linear solver predicts flutter onset later at $p_2 = 150750\,\mathrm{Pa}$ compared to $p_2 = 150500\,\mathrm{Pa}$ predicted by the Harmonic Balance solver. For mode 1T, instability is predicted earlier by the linear solver at $p_2 = 148500\,\mathrm{Pa}$ compared to $p_2 = 149000\,\mathrm{Pa}$ by the Harmonic Balance solver.

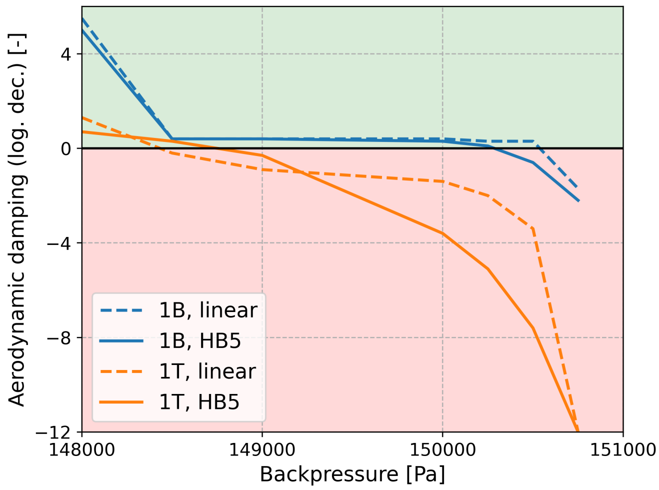

Figure 5.2.: Comparison of flutter stability between linear and Harmonic Balance solver depending on the backpressure on the 75% speed line.

The flutter analysis will focus on operating points around $p_2 = 149000 - 150500\,\mathrm{Pa}$ for mode 1B and around $p_2 = 148000 - 150000\,\mathrm{Pa}$ for mode 1T. For a better understanding of the flow field during flutter onset, a steady-state flow field analysis predates the flutter analysis. This helps linking the regions of flutter (in-)stability to aerodynamic phenomena.

5.2.1. Steady-state flow field

The incidence angle of the flow increases with increasing backpressure, leading to larger blade loads. In figure 5.3, mach contour plots for $p_2 = 148000\,\mathrm{Pa}$ and $p_2 = 150500\,\mathrm{Pa}$ are shown to visualize the steady-state flow field. On the suction side near the leading edge at the suction peak, mach numbers reach 1.3 to 1.5 depending on the backpressure. This results in a local shock that interacts with the boundary layer. For $p_2 \geq 148500\,\mathrm{Pa}$, the boundary layer separates and a recirculation region forms behind the shock. This region grows with increasing backpressure, as indicated by the wall shear stress plotted in figure 5.4a.

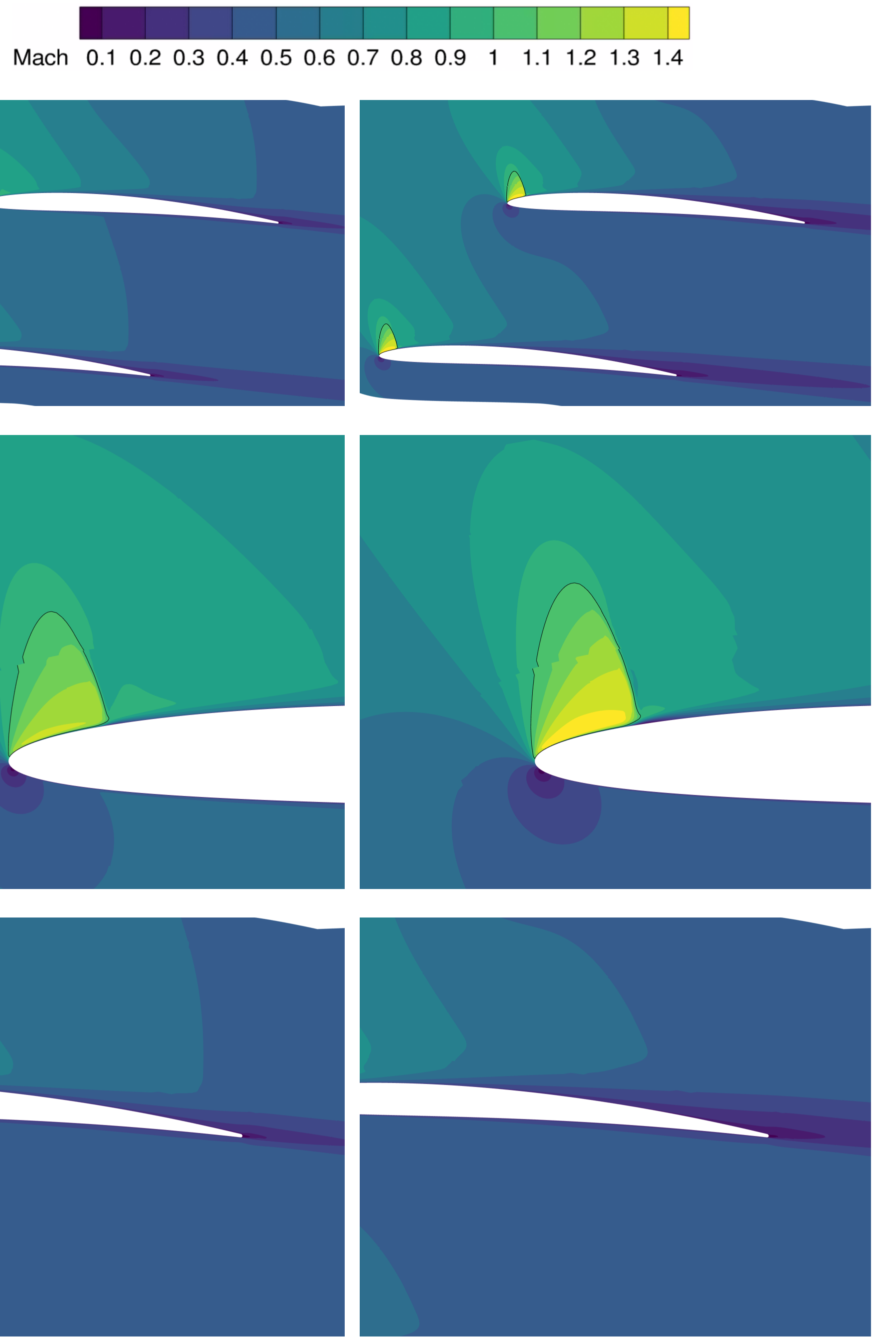

$p_2 = 148000\,\mathrm{Pa}$. $p_2 = 150500\,\mathrm{Pa}$.

Figure 5.3.: Mach contours plots for RoR 75% at $p_2 = 148000\,\mathrm{Pa}$ and $p_2 = 150500\,\mathrm{Pa}$.

A major difference between the two operating points is the velocity profile in the rotor passage. For increasing backpressure, the velocity reduces. This effect is strongest near the blade surfaces. At around 50 % chord length, the boundary layer on the suction side starts to grow and the velocity reduces downstream. With increasing backpressure, the boundary layer grows and velocity in the passage reduces; but for no investigated operating point does the flow separate prematurely upstream of the trailing edge. This is confirmed by the steady-state wall shear stresses on the suction side, plotted in figure 5.4b.

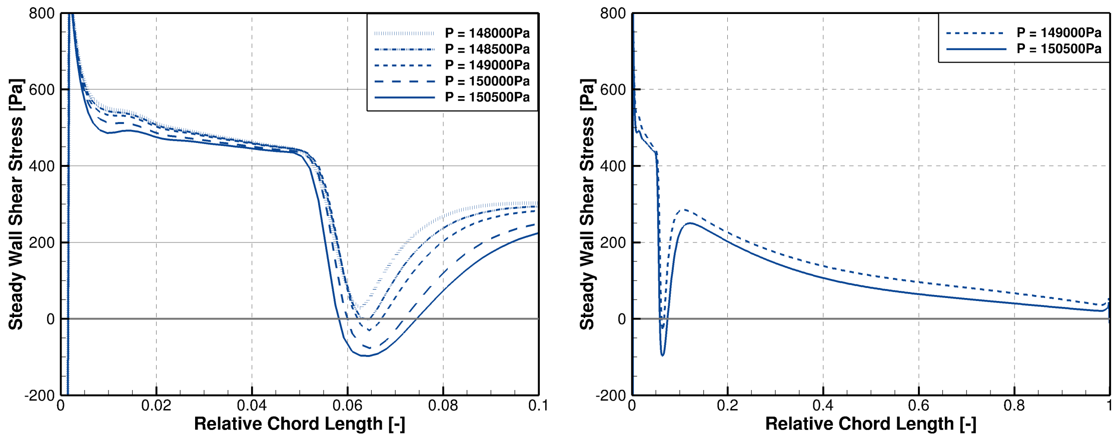

(a) Zoomed in view on the first 10% RCL.

(b) Wall shear stress over the suction side.

Figure 5.4.: Steady-state wall shear stress over the suction side for varying operating points on the 75% speed line.

5.2.2. Mode 1B

In figure 5.5, the aerodynamic damping is plotted against the IBPA over the range of investigated backpressures. Note that all converged simulations are marked by squares in figure 5.5. Some simulations, mainly for IBPAs $\sigma_n = +18°, -18°, -36°$, are not converged with respect to the criteria set in section 3.2.3.3.

For backpressures below 150000 Pa, the aerodynamic damping curve has a sinusoidal shape with the lowest aerodynamic damping at $\sigma_n = 0°$. With increasing backpressure, a maximum at $\sigma_n = +36°$ emerges for operating points with $p_2 > 150000$ Pa. On each side of the maximum, the aerodynamic damping decreases rapidly. For operating points with $p_2 > 150400$ Pa, the mode becomes unstable with the IBPA with lowest damping for $p_2 = 150400$ Pa being $\sigma_n = +108°$. Increasing backpressure moves the minimum of aerodynamic damping to $\sigma_n = +72°$ for $p_2 = 150500$ Pa and $\sigma_n = +54°$ for $p_2 = 150750$ Pa.

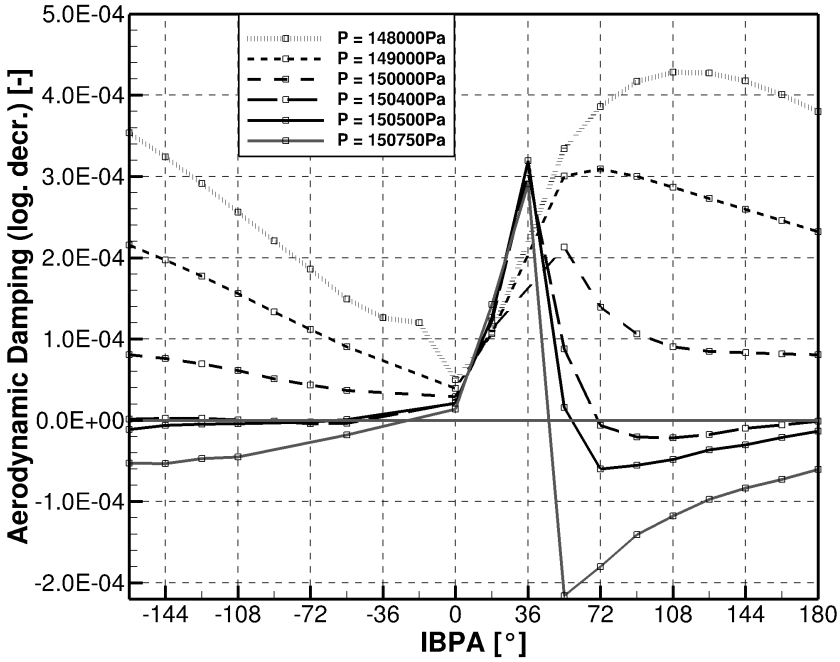

Figure 5.5.: Aerodynamic damping against IBPAs for mode 1B for varying operating points on the 75 % speed line.

5.2.2.1. Analysis of aerodynamic work

The IBPA of $\sigma_n = +72°$ is chosen to analyze the flutter mechanisms in the transonic stall flutter regime. It is the most unstable IBPA for $p_2 = 150500$ Pa and stable for $p_2 = 149000$ Pa. The first step is to investigate on which parts of the blade aerodynamic work excites or damps the oscillations. As described in section 2.3.3, the sign of the real part of the aerodynamic work indicates whether the aerodynamic work is stabilizing or destabilizing. In figure 5.6, the real part of the aerodynamic work is plotted over the relative chord length (RCL) of the pressure and suction side of the blade for $p_2 = 149000$ Pa and $p_2 = 150500$ Pa.

Pressure side

Analyzing the aerodynamic work on the pressure side, plotted in figure 5.6, no qualitative differences are present between both operating points. At the leading edge,

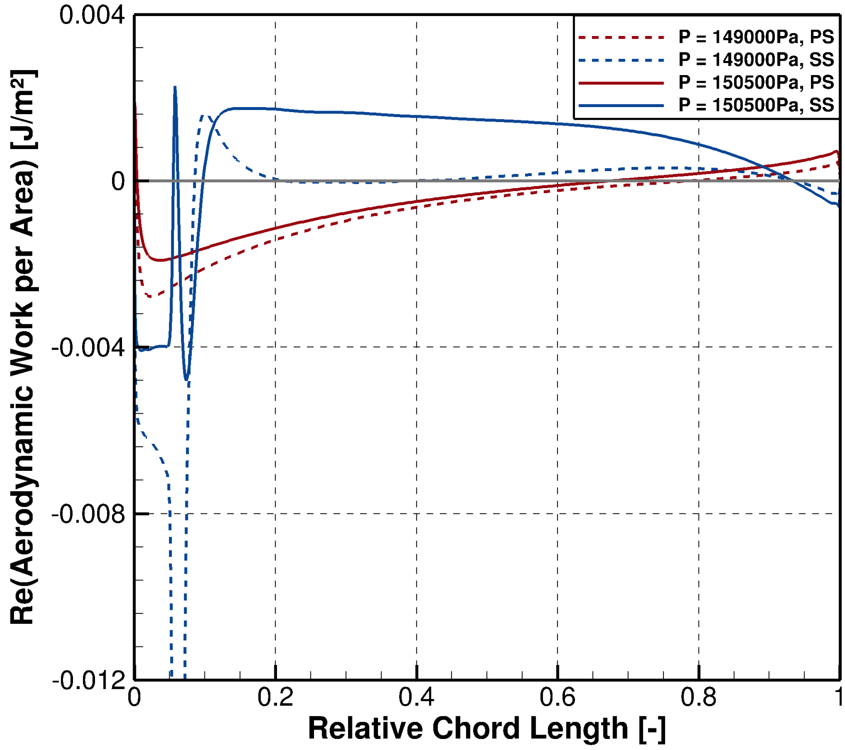

Figure 5.6.: Real part of aerodynamic work for $p_2 = 149000$ Pa and $p_2 = 150500$ Pa; RoR 75 %, mode 1B, $\sigma_n = +72°$.

the aerodynamic work is positive for a short section (around 1 % RCL) and sharply turns negative for both operating points, with a minimum at $2 - 4$ % RCL. This matches the stagnation point of the flow and its migration downstream for increasing incidence angles caused by higher backpressures. For operating points with higher backpressure, the minimum is located further downstream and its magnitude decreases. Following the minimum, the aerodynamic work increases almost linearly to the trailing edge, becoming positive at around 70 % RCL. For all investigated operating points on the 75 % speed line, the pressure side is stabilizing. The stabilizing effect slightly decreases for increasing backpressure.

Suction side

On the suction side, the behavior of aerodynamic work over the whole chord length and for different backpressures is more complex compared to the pressure side of the blade due to the shock at the suction peak and its interaction with the boundary layer. There are three distinct regions, out of which two play a significant role in the determination of the aeroelastic stability. Complementary to figure 5.6, aerodynamic work is also plotted over the suction side for $p_2 = 149000\,\text{Pa}$, $p_2 = 150000\,\text{Pa}$, $p_2 = 150400\,\text{Pa}$ and $p_2 = 150500\,\text{Pa}$ in figure 5.7 and the three regions are marked.

The first region begins at the leading edge and extends till 10 % RCL. For operating points at lower backpressures, this region is strongly stabilizing with a sharp minimum of aerodynamic work around the shock at 6 % RCL. Downstream, the aerodynamic work increases till the end of region 1 at 10 % RCL, where aerodynamic work becomes positive for all shown operating points. With increasing backpressure, the magnitude of the minimum at 6 % RCL decreases and for $p_2 = 150500\,\text{Pa}$ there is a small local maximum at the shock instead of the minimum. For the rest of region 1, the behavior is similar to the other operating points. Overall, the first region on the suction side has a stabilizing influence for lower backpressures and becomes slightly destabilizing for $p_2 > 150400\,\text{Pa}$.

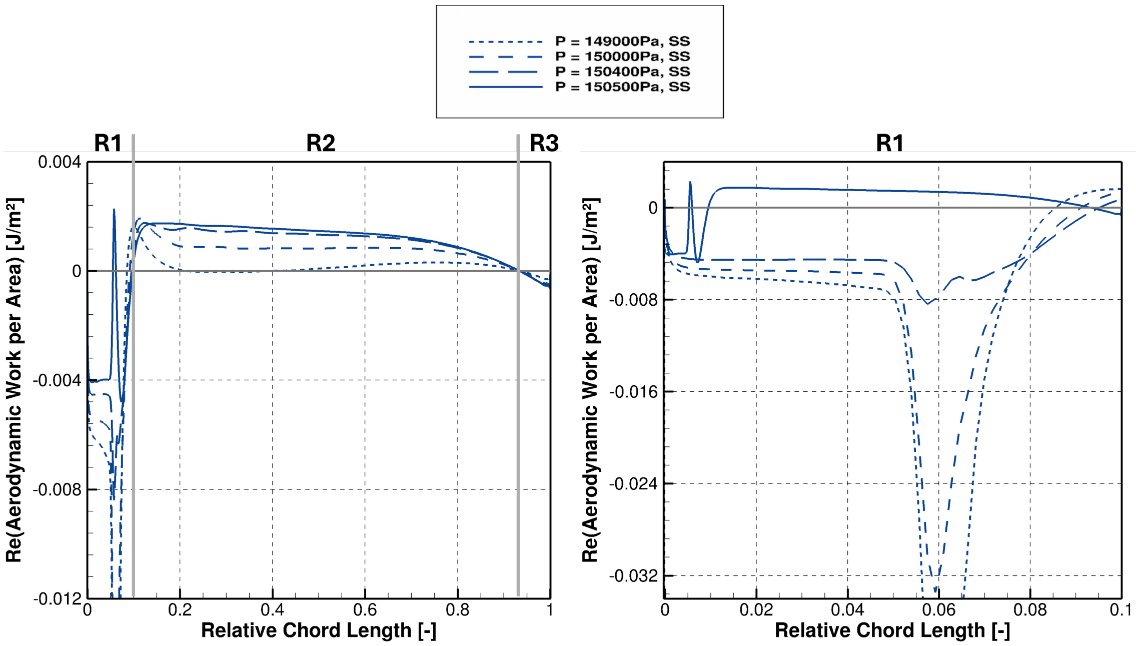

Figure 5.7.: Real part of aerodynamic work on the suction side (zoomed in view on the first 10 % RCL on the right) for varying backpressures; RoR 75 %, mode 1B, $\sigma_n = +72°$.

The second region on the suction side stretches from 10% to 94% RCL. It is the main destabilizing contributor for $p_2 = 150500\,\text{Pa}$. Following region 1, the aerodynamic work increases until 12% RCL and stays nearly constant up to 80% RCL. From 80% to 94% RCL, aerodynamic work falls off to 0. For $p_2 = 149000\,\text{Pa}$, this region is only minimally destabilizing. While the aerodynamic work also rises until 10%

RCL, it does not stay constant, but decreases to 0 at 20% RCL and only increases marginally until about 80% RCL. A comparison of the aerodynamic work with other operating points, plotted in figure 5.7, shows similar behavior, with a maximum at around $10-12\,\%$ RCL and nearly constant aerodynamic work from $20-80\,\%$ RCL, with the value of aerodynamic work increasing with increasing backpressure.

The last region on the suction side ranges from 94%-100% RCL. Here, the aerodynamic work turns negative for all investigated operating points. From the beginning of the region to the trailing edge, the work decreases linearly. There are only small variations between different operating conditions. Since this region is small, has only a small stabilizing effect and this effect does not change for varying backpressures, it will be ignored in the detailed investigation.

5.2.2.2. Analysis of magnitude and phase of aerodynamic work

The aerodynamic work, defined in equation (2.60), can be expressed using its magnitude and its phase angle. The phase angle determines the sign of the aerodynamic work and modulates how strongly the magnitude impacts the flutter stability. Thus, the analysis of phase and magnitude can give greater insights on the most influential parts of the blade. The analysis is focused on the three main regions responsible for flutter instability, which where identified to contribute to the flutter stability.

The pressure side experiences negative aerodynamic work from 0% to around 70% RCL, depending on backpressure, and from around 70% RCL to the trailing edge slightly positive aerodynamic work. Overall, the pressure side has a damping influence, but the effect decreases with increasing backpressure.

Region 1 on the suction side begins at the leading edge and extends to 10% RCL. It is defined by a minimum in negative aerodynamic work around the shock at the suction peak. The magnitude of this minimum decreases with increasing backpressure and for $p_2 \geq 150500\,\mathrm{Pa}$ the minimum becomes a positive maximum. Region 1 on the suction side is stabilizing, but for increasing backpressure, the effect diminishes.

Region 2 on the suction side follows region 1 and extends from 10%-90% RCL. It is characterized by nearly constant positive aerodynamic work for $p_2 \geq 149000\,\mathrm{Pa}$, that increases with increasing backpressure. Overall, this region is the main region driving the excitation of vibrations.

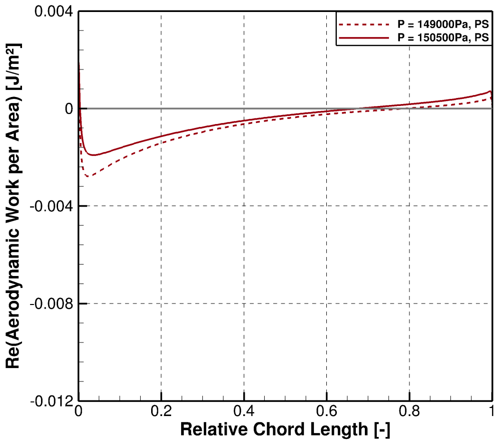

(a) Real part.

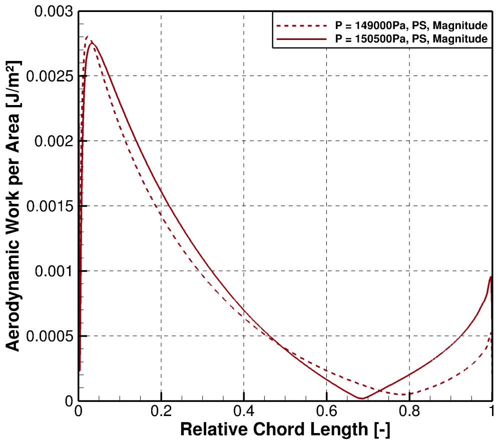

(b) Magnitude.

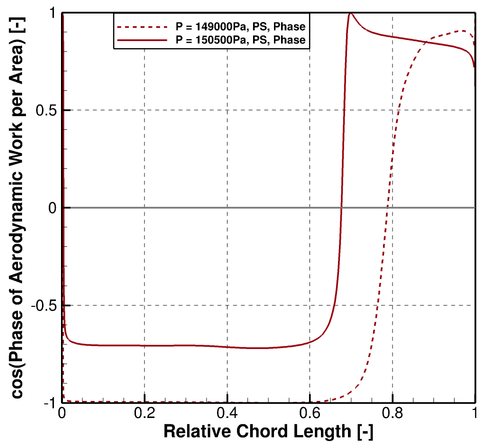

(c) Cosine of phase.

Figure 5.8.: Complex aerodynamic work on the pressure side for RoR 75%, mode 1B, $\sigma_n = +72°$.

Pressure side

The complex aerodynamic work on the pressure side is plotted in figures 5.8. In figures 5.8a, 5.8b and 5.8c the real part, magnitude and cosine of the phase are shown respectively.

The magnitude of aerodynamic work has a maximum around $2 - 4\%$ RCL. The value is nearly identical for both operating points. Subsequently, the magnitude decreases until 80% RCL for $p_2 = 149000\,\text{Pa}$ and 70% RCL for $p_2 = 150500\,\text{Pa}$, where the magnitude becomes 0. Downstream of the minimum, the magnitude increases until the trailing edge. Overall, the magnitude of aerodynamic work for $p_2 = 149000\,\text{Pa}$ and $p_2 = 150500\,\text{Pa}$ behave nearly identically.

The cosine of the phase is $+1$ at the leading edge for both cases and sharply decreases to -1 for $p_2 = 149000\,\text{Pa}$ and to -0.7 for $p_2 = 150500\,\text{Pa}$ at $1\,\%$ RCL. The phase stays nearly constant until 60% RCL for $p_2 = 150500\,\text{Pa}$ and 70% RCL for $p_2 = 149000\,\text{Pa}$. At these points, the phase jumps from -0.7 to $+1$ and from -1 to $+0.9$ respectively, resulting in the change of sign in the aerodynamic work.

The lower stabilizing influence of the pressure side on the overall flutter stability for $p_2 = 150500\,\text{Pa}$ compared to $p_2 = 149000\,\text{Pa}$ mainly stems from a difference in phase angle, since the magnitude in aerodynamic work does not change significantly.

Suction side - Region 1

The complex aerodynamic work in region 1 on the suction side is plotted in figure 5.9. In figures 5.9a, 5.9b and 5.9c the real part, magnitude and cosine of the phase are shown respectively.

The behavior of the magnitude of aerodynamic work in this region is very similar between $p_2 = 149000\,\text{Pa}$ and $p_2 = 150500\,\text{Pa}$. It has a strong maximum around the shock at 6% RCL. The exact location varies, as it moves forward for increasing backpressures. The magnitude is the same for both operating points.

The difference in aerodynamic work in region 1 between $p_2 = 149000\,\text{Pa}$ and $p_2 = 150500\,\text{Pa}$ lies in different phase angles. The cosine of the phase starts at -1 for $p_2 = 149000\,\text{Pa}$ and stays nearly constant until 8% RCL, where it rises to $+0.9$. At this point, the magnitude of aerodynamic work has already dropped. In contrast, for $p_2 = 150500\,\text{Pa}$ the phase starts at -0.7 and rises only to slightly above 0 at 6% RCL, to drop to -1 at 9% RCL and rise to $+1$ at 10% RCL.

The phase for $p_2 = 149000\,\text{Pa}$ explains the large stabilizing contribution of region 1 for $p_2 = 149000\,\text{Pa}$. For $p_2 = 150500\,\text{Pa}$, the phase lets the maximum in aerodynamic work magnitude contribute little to the overall aerodynamic stability, leading to only a slightly stabilizing effect of region 1 for $p_2 = 150500\,\text{Pa}$.

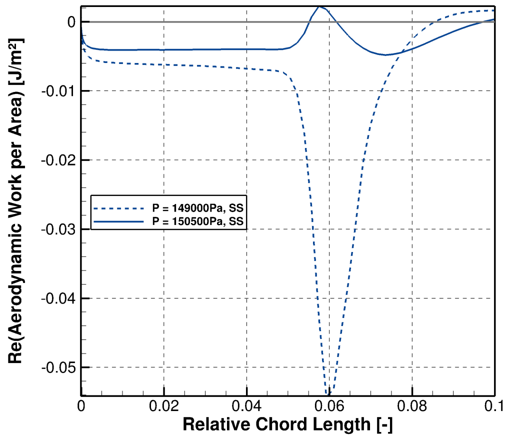

(a) Real part in region 1.

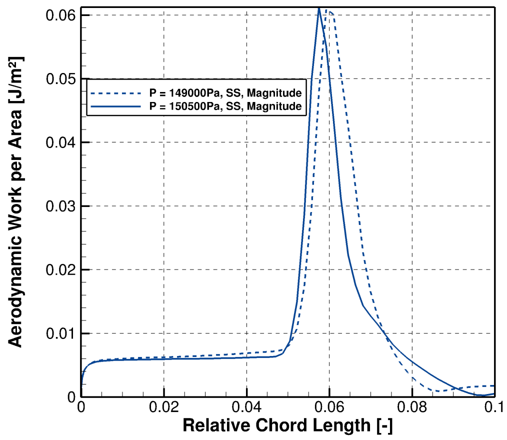

(b) Magnitude in region 1.

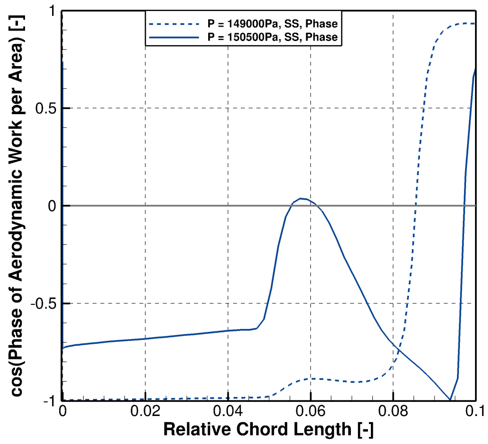

(c) Cosine of phase in region 1.

Figure 5.9.: Complex aerodynamic work in region 1 on the suction side for RoR 75%, mode 1B, $\sigma_n = +72°$.

Shock - boundary layer interaction

Regions 1 and 2 on the suction side are identified to feature the aerodynamic mechanisms for flutter to arise. The shock around 6% RCL has a strong influence on the magnitude and phase angle of aerodynamic work and the phase angle shows strong variations between different operating conditions. In the following, the position of the shock wave, the interaction with the boundary layer and the influence of the blade oscillation are further investigated.

Through shock - boundary layer interactions, the boundary layer detaches at the shock location for backpressures $p_2 > 148000\,\mathrm{Pa}$. The separation region grows for increasing backpressures, as identified in figure 5.4a. Because of the oscillation of the blade, the separation point moves periodically.
For $p_2 = 149000\,\mathrm{Pa}$ and $p_2 = 150500\,\mathrm{Pa}$, the RCL of the separation point over one oscillation period is normalized and plotted in figure 5.10a. The phase is expressed in degrees to analyze the phase of the oscillations, which shifts from $p_2 = 149000\,\mathrm{Pa}$ to $p_2 = 150500\,\mathrm{Pa}$ by about 65°. The same phase shift can be observed in figure 5.10c, where the unsteady pressure oscillations at the separation point is plotted over one period. Unsteady pressure oscillations are shifted by 180° relative to the separation point oscillations.
The phase shift of 65° in unsteady pressure integrates to a 65° phase shift in aerodynamic work. This leads to the local maximum in cosine of the phase of aerodynamic work for $p_2 = 150500\,\mathrm{Pa}$ at 6 % RCL, shown in figure 5.10d, which matches the local maximum in magnitude and leads to less stabilization in region 1.
For operating points where no separation occurs ($p_2 < 148500\,\mathrm{Pa}$), the phase of aerodynamic work stays constant, with the cosine of the phase of -1 around the shock location. This can also be seen in figure 5.10d, where the phases of aerodynamic work for $p_2 = 147000\,\mathrm{Pa}$ and $p_2 = 148000\,\mathrm{Pa}$ are plotted. This further underlines the importance of the influence of the interaction of blade oscillations and shock induced boundary layer separation.

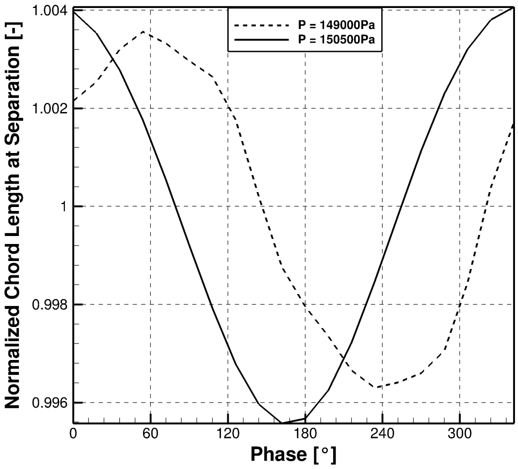

(a) Normalized RCL at Separation.

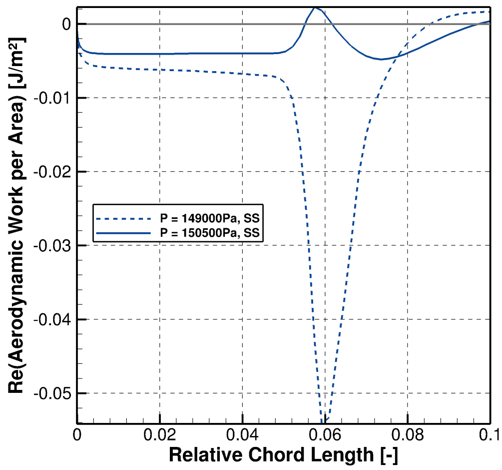

(b) Real part of aerodynamic work in region 1.

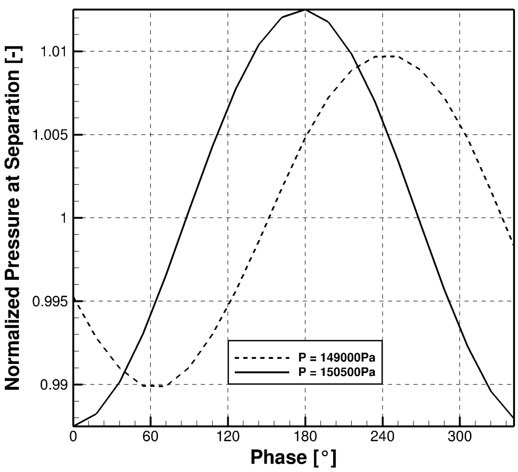

(c) Normalized pressure at separation.

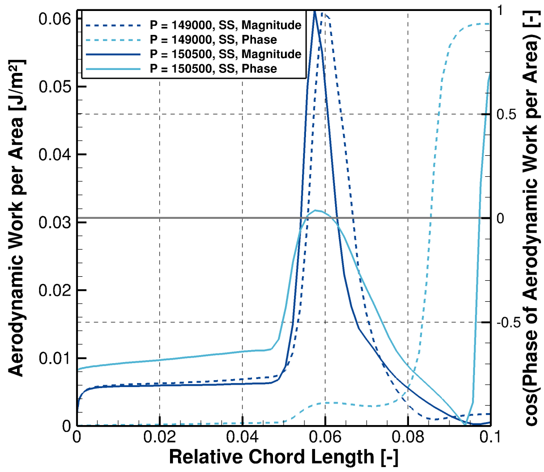

(d) Magnitude and cosine of phase of aerodynamic work in region 1.

Figure 5.10.: Normalized RCL and unsteady pressure at separation and complex aerodynamic work in region 1 on the suction side for $p_2 = 149000\,\mathrm{Pa}$ and $p_2 = 150500\,\mathrm{Pa}$, RoR 75%, mode 1B, $\sigma_n = +72°$.

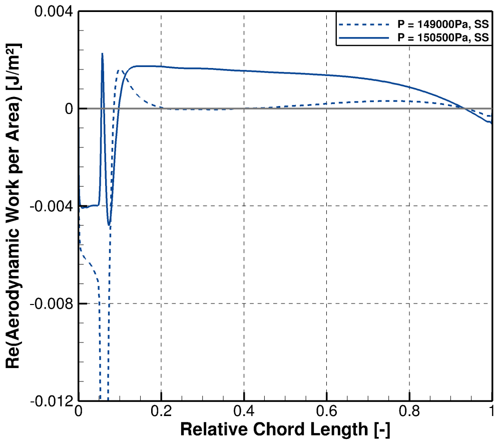

(a) Real part.

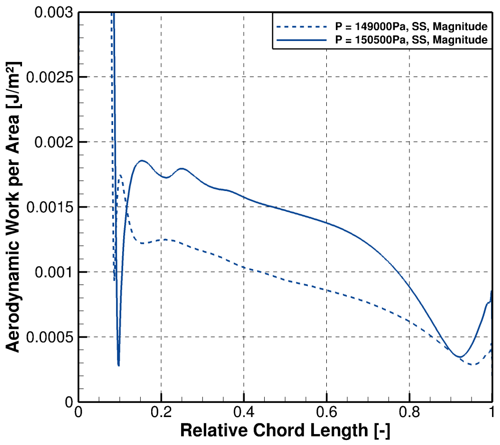

(b) Magnitude.

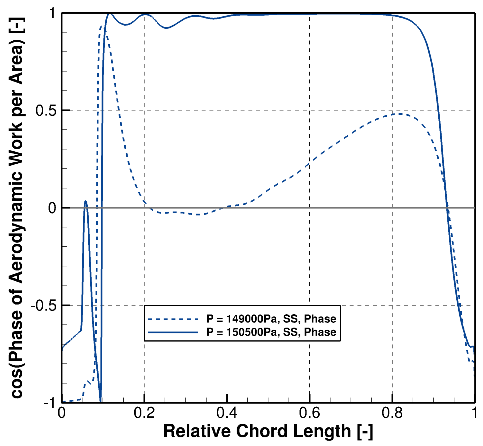

(c) Cosine of phase.

Figure 5.11.: Complex aerodynamic work on the suction side for RoR 75%, mode 1B, $\sigma_n = +72°$.

Suction side - Region 2

Region 2 on the suction side starts at a minimum in aerodynamic work magnitude at 10% RCL for both operating points. Downstream, the magnitude increases until 11 % RCL for $p_2 = 149000\,\text{Pa}$ and until 15 % for $p_2 = 150500\,\text{Pa}$. From there, the magnitude decreases nearly linearly to 70% RCL. In the region between 15 % and 70 % RCL, the magnitude for $p_2 = 150500\,\text{Pa}$ is around 30 % greater compared to $p_2 = 149000\,\text{Pa}$.

For $p_2 = 149000\,\text{Pa}$, the cosine of phase starts at +0.9 at 10% RCL and decreases to 0 after 20% RCL, stays nearly constant until 40% RCL and linearly increases to +0.5 at 80% RCL, to then decrease to −0.9 at the trailing edge. The cosine of phase of $p_2 = 150500\,\text{Pa}$ behaves much more simple. It rises to +1 at 10% RCL and stays nearly constant until about 85% RCL, where it decreases to about −0.7 at the trailing edge.

The mostly neutral to only slightly destabilizing characteristic of region 2 for $p_2 = 149000\,\text{Pa}$ lies in its phase angle, that lies between 0 and +0.5, together with a lower magnitude compared to $p_2 = 150500\,\text{Pa}$. In contrast, the strongly destabilizing phase angle in region 2 leads to a strongly destabilizing entry of aerodynamic work over the whole of region 2 for $p_2 = 150500\,\text{Pa}$.

Phase of (re-)attached boundary layer

While the separation and reattachment of the flow around the shock is the key mechanism of aeroelastic stability in region 1, downstream in region 2, the phase of aerodynamic work significantly shifts for operating points with and without flow separation. This is shown in figure 5.12, where the phase of aerodynamic work is plotted over the relative chord length for $p_2 = 147000\,\mathrm{Pa}$, $p_2 = 148000\,\mathrm{Pa}$, $p_2 = 149000\,\mathrm{Pa}$ and $p_2 = 150500\,\mathrm{PaL}$. For all operating points, the phase of aerodynamic work has a maximum at the beginning of region 2 at around 10 % RCL. For operating points without shock induced separation, the value of the maximum is approximately $-0.5\,\mathrm{rad}$, while for operating points where the flow separates, higher values are reached. Until 20 % RCL, the phase decreases to different values for all operating conditions. From there to around $80 - 90\,\%$ RCL, the phase increases slightly, to then fall off to about $-2.5\,\mathrm{rad}$ downstream near the trailing edge.

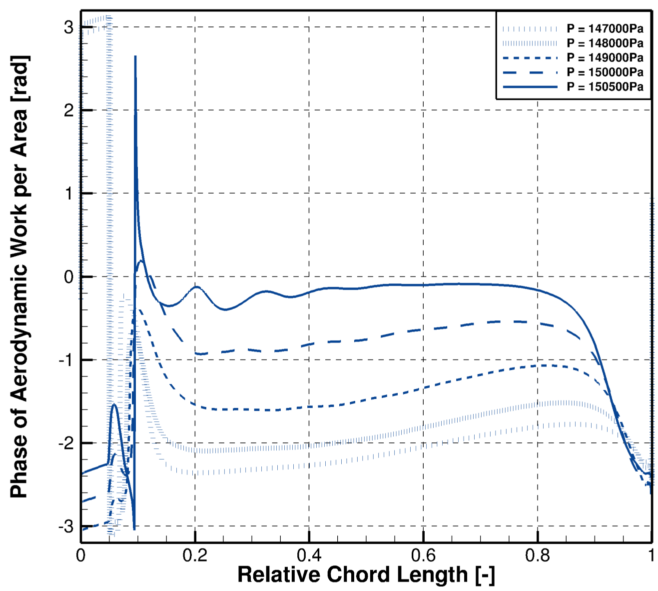

Figure 5.12.: Phase of aerodynamic work for $p_2 = 147000\,\mathrm{Pa}$, $p_2 = 148000\,\mathrm{Pa}$, $p_2 = 149000\,\mathrm{Pa}$ and $p_2 = 150500\,\mathrm{Pa}$, RoR 75%, mode 1B, $\sigma_n = +72°$.

While flutter stability in region 1 on the suction side is mainly influenced by the shock - boundary layer interaction and in region 3 near the trailing edge, the phases for varying operating conditions show little difference; the findings are inconclusive about the mechanisms causing different phases of unsteady pressure and thus aerodynamic work in region 2. The reattachment of the flow influences the phase between $10 - 20\,\%$ RCL. However it is unclear how far downstream this effect persists, since differences in phase are also present for operating conditions without separation and reattachment between $20 - 80\,\%$ RCL.

To further investigate the mechanisms influencing flutter stability in region 2 on the suction side, an analysis on the $55\,\%$ speed line near stall is conducted. On that speed line, shocks are only present for high backpressures and are significantly weaker compared to the $75\,\%$ speed line.

Comparison with operating points on the $55\,\%$ speed line

For the comparison of flutter stability effects between the $55\,\%$ and $75\,\%$ speed lines, operating points from $p_2 = 143000\,\mathrm{Pa}$ to $p_2 = 145000\,\mathrm{Pa}$ are chosen on the $55\,\%$ speed line. The aerodynamic damping is plotted against the IBPA for the investigated operating points in figure 5.13. Similar to the $75\,\%$ speed line, for lower backpressures, the curve has a sinusoidal shape with lowest damping at $\sigma_n = 0°$. For $p_2 = 145000\,\mathrm{Pa}$, a sharp maximum in aerodynamic damping at $\sigma_n = +54°$ and a negative minimum at $\sigma_n = +108°$ emerge. The IBPA of the minimum is used for the investigation. This IBPA is shifted compared to the IBPA of $\sigma_n = +72°$ for $p_2 = 150500\,\mathrm{Pa}$ on the $75\,\%$ speed line.

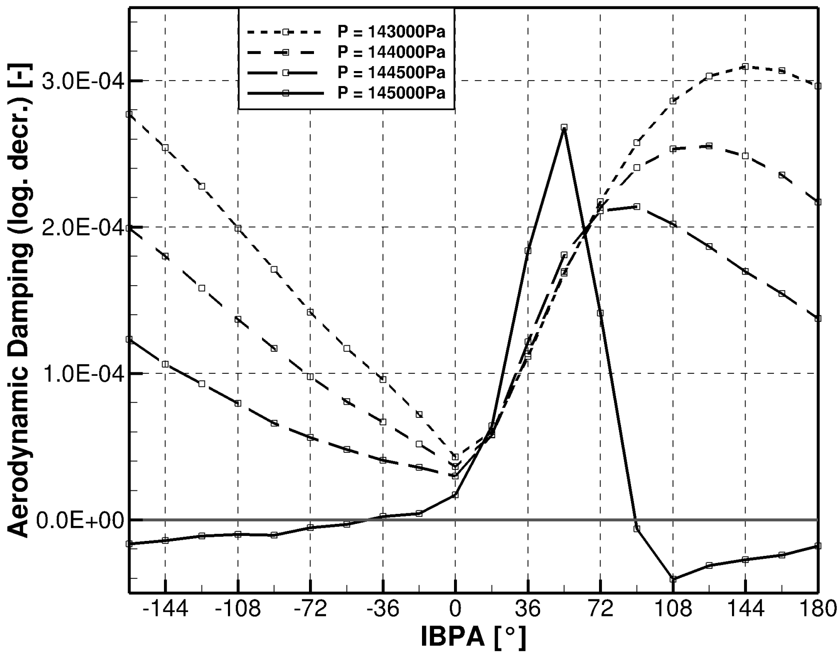

Figure 5.13.: Aerodynamic damping against IBPAs for mode 1B for varying operating points on the $55\,\%$ speed line.

A steady-state mach contour plot for $p_2 = 145000\,\mathrm{Pa}$ is displayed in figure 5.14a. Mach numbers are lower compared to the 75 % speed line and only a minor shock is present. The shock is located nearer the leading edge. The flow separates for back pressures $p_2 > 143000\,\mathrm{Pa}$, as shown in figure 5.14b, where the wall shear stress is plotted over the first 10 % RCL.

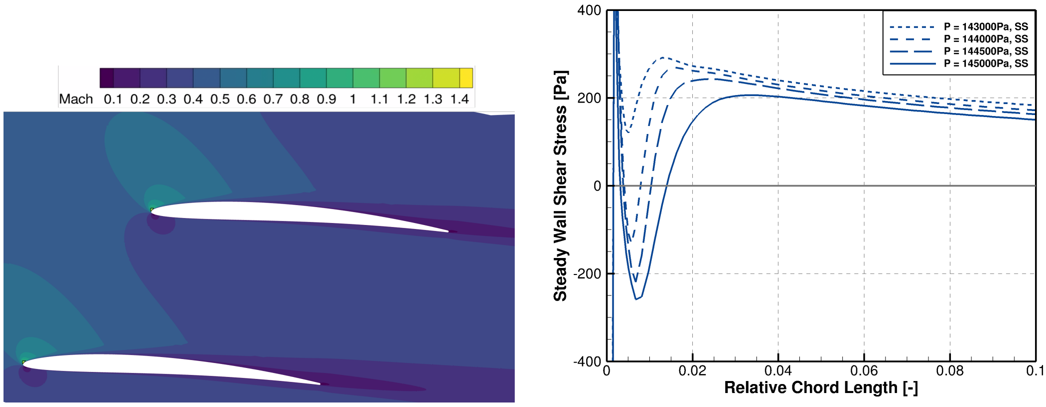

(a) Mach contour plot for $p_2 = 145000\,\mathrm{Pa}$.

(b) Wall shear stress at 0% − 10% RCL.

Figure 5.14.: steady-state flow field for operating points on the 55% speed line.

In figure 5.15a, the real part of aerodynamic work for the investigated operating points on the 55 % speed line is plotted over the suction side. Similarly to the 75 % speed line, the region near the leading edge is strongly stabilizing, but for $p_2 = 145000\,\mathrm{Pa}$, around the shock, a small, destabilizing maximum is present. Further downstream, the aerodynamic work becomes less stabilizing or even destabilizing for $p_2 = 145000\,\mathrm{Pa}$. From $20 - 80$ % RCL, the aerodynamic work stays nearly constant. The magnitude of aerodynamic work varies only slightly for different backpressures on the 55 % speed line, but the phase shows a strong dependence on backpressure, which can be deduced from figure 5.15b, where the cosine of the phase is plotted over the suction side for the 55 % speed line. For $p_2 = 143000\,\mathrm{Pa}$, the phase is strongly stabilizing with values below -0.7. For increasing backpressure, the cosine of the phase increases, but only for $p_2 = 145000\,\mathrm{Pa}$ it becomes positive. The shock shows a small local effect on the phase for $p_2 = 144500\,\mathrm{Pa}$ and a strong local effect for $p_2 = 145000\,\mathrm{Pa}$, where the cosine of the phase becomes $+1$, but decreases sharply to -0.5 when the flow reattaches.

In figure 5.15d, the cosine of the phase of aerodynamic work for the 75 % speed line is plotted over the suction side as comparison to figure 5.15b. On both speed lines, the influence of the shock on the phase increases with increasing backpressure. This influence is minimal for operating conditions without boundary layer separation. Boundary layer separation alone is neither locally nor globally a guarantee for destabilizing behavior, as seen in figures 5.15b and 5.15d, where aerodynamic work only excites the oscillation for $p_2 = 145000\,\mathrm{Pa}$ (55 % speed line) and $p_2 = 150500\,\mathrm{Pa}$ (75 % speed line). Nonetheless, shock induced boundary layer separation is present in all investigated cases where flutter in the first bending mode occurs. Additionally, the steady-state flow field further downstream is influenced by the boundary layer thickening introduced by the separation and reattachment. This seems to be another main driver of flutter instability.

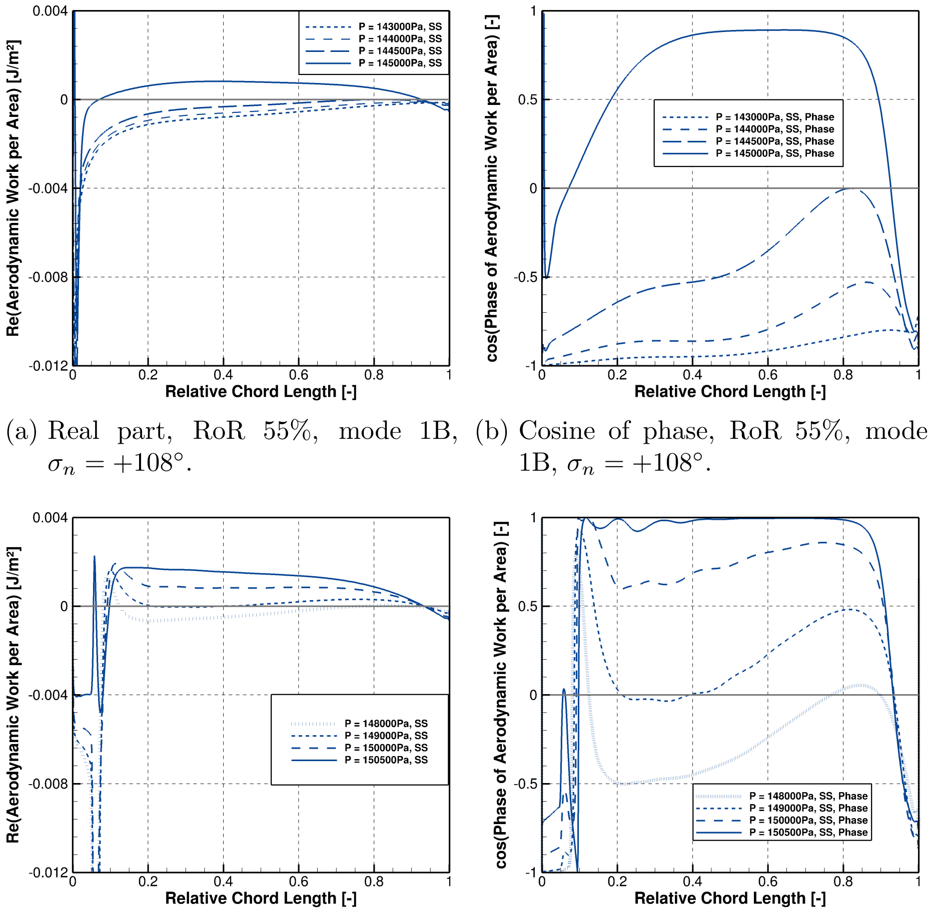

(a) Real part, RoR 55%, mode 1B, $\sigma_n = +108°$.

(b) Cosine of phase, RoR 55%, mode 1B, $\sigma_n = +108°$.

(c) Real part, RoR 75%, mode 1B, $\sigma_n = +72°$.

(d) Cosine of phase, RoR 75%, mode 1B, $\sigma_n = +72°$.

Figure 5.15.: Aerodynamic work on the suction side for: RoR 55%, mode 1B, $\sigma_n = +108°$ (top) and RoR 75%, mode 1B, $\sigma_n = +72°$ (bottom).

5.2.3. Mode 1T

In figure 5.16, the aerodynamic damping is plotted against the IBPA over the range of investigated backpressures. Compared to the first bending mode, all simulations are converged. This is a general trend that was observed for most operating points on all speed lines.

For the first three operating points, the aerodynamic damping curve has a sinusoidal shape, with the lowest damping for IBPAs between $\sigma_n = -126$ and $\sigma_n = -72°$. For $p_2 = 149000\,\text{Pa}$, the aerodynamic damping becomes negative. The highest damping occurs for $\sigma_n = +72°$ and $\sigma_n = +90°$. The local maximum at $\sigma_n = -36°$ interrupts the sinusoidal shape. Aerodynamic damping decreases in nearly all IBPAs with increasing backpressure. For $p_2 = 150000\,\text{Pa}$, the aerodynamic damping becomes negative between $+144°$ and $-54°$ with a minimum at $\sigma_n = +180°$.

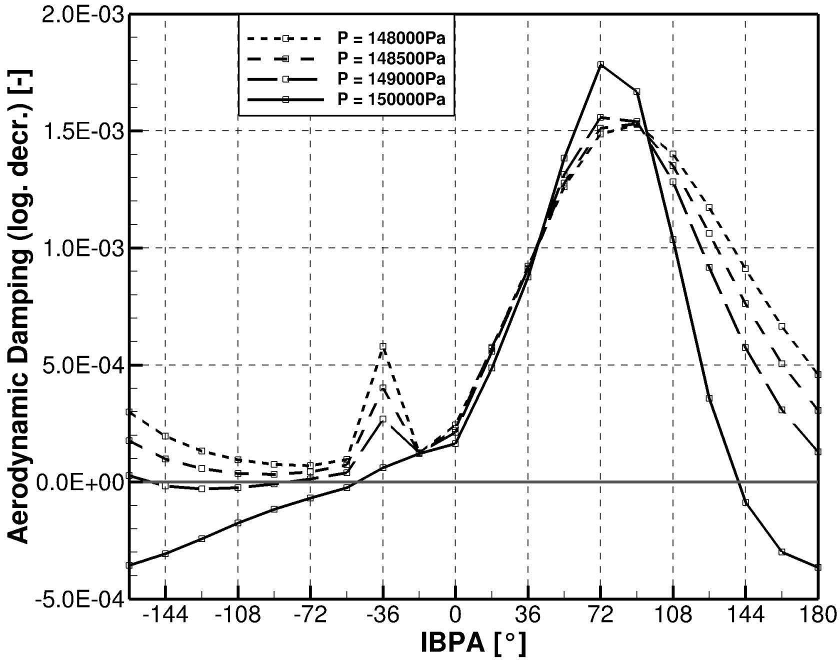

Figure 5.16.: Aerodynamic damping against IBPAs for mode 1T for varying operating points on the 75 % speed line.

The investigation follows the same pattern as for the bending mode. First, the regions that are responsible for changes in flutter stability are identified. Second, the complex aerodynamic work in these regions is investigated. Last, a comparison with the 55 % speed line is done to investigate the influence of the shock and its interaction with the boundary layer on flutter stability.

5.2.3.1. Analysis of aerodynamic work

In the following, the flutter mechanisms for $\sigma_n = 180°$ will be analyzed and discussed. This is the most unstable IBPA for $p_2 = 150000\,\text{Pa}$ with negative aerodynamic damping, while the aerodynamic damping for the other operating points is positive. In figure 5.17, the real part of the aerodynamic work is plotted over the relative chord length of the blade for backpressures $p_2 = 148000\,\text{Pa}$ and $p_2 = 150000\,\text{Pa}$.

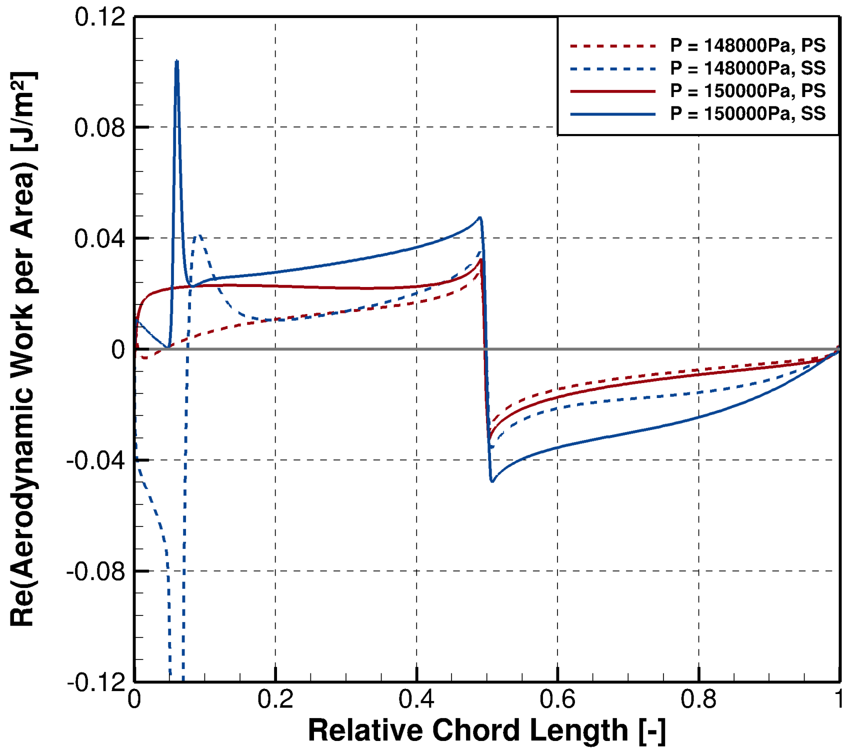

Figure 5.17.: Real part of aerodynamic work for $p_2 = 148000\,\text{Pa}$ and $p_2 = 150000\,\text{Pa}$, 55 % RoR, mode 1T, $\sigma_n = +180°$.

The behavior of aerodynamic work over the chord length of the blade has a significant difference to the bending mode. The torsion over the midpoint results in opposite displacements of the surface in the first and second halves of the blade, as depicted in figure 3.3. This results in opposite signs of aerodynamic work for both halves.

Pressure side

Aerodynamic work on the pressure side, plotted in figure 5.17, shows qualitative differences between the two investigated operating points on the first half of the blade. For $p_2 = 148000\,\mathrm{Pa}$, a local minimum in aerodynamic work is present at 2 % RCL. From there, aerodynamic work increases nearly linearly until the midpoint. For $p_2 = 150000\,\mathrm{Pa}$, no peak at the leading edge is present. The aerodynamic work increases from 0 % to 3 % RCL and stays approximately constant until shortly before the midpoint of the chord length, where it increases again. Around the rotational midpoint, for all operating points, the sign of aerodynamic work changes, but the magnitude stays constant. Subsequently, aerodynamic work increases towards the trailing edge. On the second half of the pressure side, there are no significant differences in aerodynamic work between the different operating points.

For $p_2 = 148000\,\mathrm{Pa}$, the pressure side is neither stabilizing nor destabilizing because both halves cancel each other out. For $p_2 = 150000\,\mathrm{Pa}$, the pressure side is slightly destabilizing, due to the stronger positive aerodynamic work on the first half. This effect increases with increasing backpressures.

Suction side

Similar to mode 1B, the analysis of aerodynamic work on the suction side is more complex compared to the pressure side, due to the shock on the suction side and its interaction with the boundary layer. The suction side can be divided into three regions with distinct behavior of aerodynamic work. In figure 5.18 aerodynamic work is plotted over the suction side for multiple operating points and the regions are marked.

The first region extends from the leading edge to 10 % RCL. For operating points at lower backpressure, this region is strongly stabilizing with a sharp minimum of aerodynamic work around the shock at 6 % RCL. For increasing backpressure, the minimum decreases in magnitude and for $p_2 = 150000\,\mathrm{Pa}$ turns into a maximum with positive aerodynamic work. Downstream for $p_2 < 150000\,\mathrm{Pa}$, the aerodynamic work increases sharply at the end of region 1. For $p_2 \geq 150000\,\mathrm{Pa}$ the aerodynamic work reduces behind the shock. The first region on the suction side has a stabilizing influence for backpressures lower than 150000 Pa and a destabilizing influence above.

The second region lies between 10 % RCL and the midpoint at 50 % RCL. For $p_2 = 148000\,\text{Pa}$, it starts with a maximum of aerodynamic work, which reduces until 18 % RCL and then increases until the midpoint. For $p_2 = 150000\,\text{Pa}$ no local maximum is present. Aerodynamic work increases linearly to the midpoint. The second region is destabilizing for all investigated operating conditions. The exciting influence increases with increasing backpressure.

The last region is the second half of the suction side of the blade. At the beginning, aerodynamic work changes signs due to the rotation around the midpoint. The magnitude of aerodynamic work stays constant. For all operating points, the aerodynamic work increases to the trailing edge, where it becomes 0. The second half of the suction side has a stabilizing effect for all investigated operating points. The effect increases with increasing backpressure.

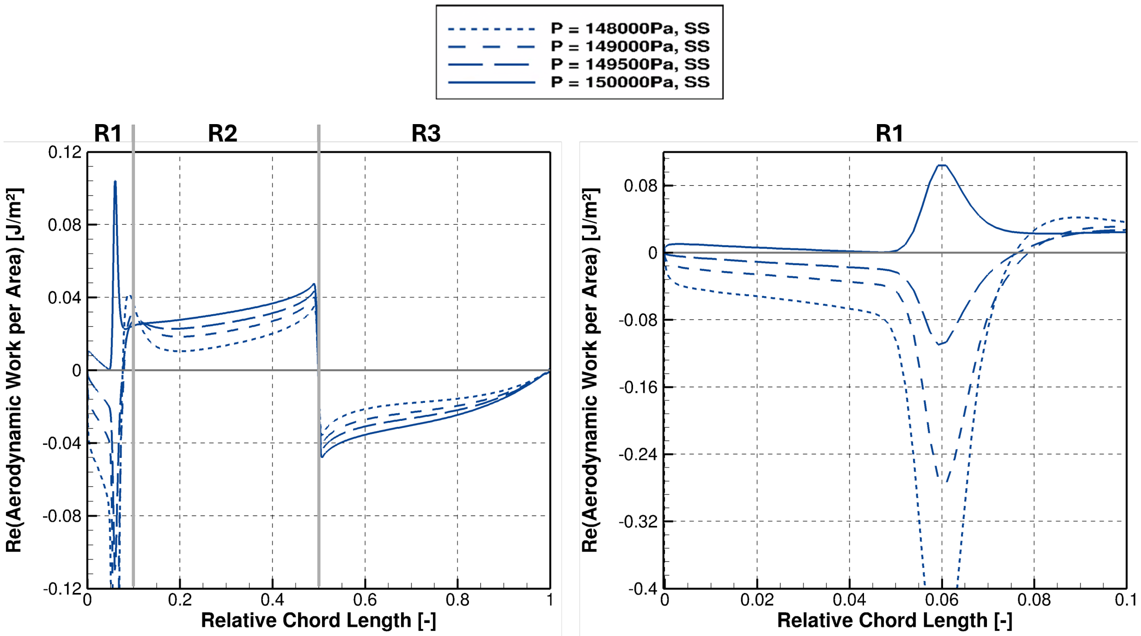

Figure 5.18.: Real part of aerodynamic work on the suction side (zoomed in view on the first 10 % RCL on the right) for varying backpressures; RoR 75 %, mode 1T, $\sigma_n = +180°$.

5.2.3.2. Analysis of magnitude and phase of aerodynamic work

Following the investigation of the real part of aerodynamic work, the magnitude and phase of the complex aerodynamic work is analyzed. The phase angle determines the sign of the aerodynamic work and modulates how strongly the magnitude impacts the flutter stability. The analysis is focused on the three main regions, responsible for aeroelastic instability, that were identified.

The first half on the pressure side experiences positive aerodynamic work. It has an exciting influence on flutter, which increases with increasing backpressure. For higher backpressures, this stabilizing effect is not canceled by the stabilizing second half of the pressure side.

Region 1 on the suction side begins at the leading edge and extends until 10 % RCL. It is defined by a minimum of negative aerodynamic work around the shock at the suction peak. This minimum decreases with increasing backpressure and for $p_2 \geq 150000\,\mathrm{Pa}$ the minimum becomes a positive maximum. Region 1 on the suction side is stabilizing for $p_2 > 150000\,\mathrm{Pa}$ and destabilizing for $p_2 < 150000\,\mathrm{Pa}$.

Region 2 on the suction side lies within 10 % and 50 % RCL. The aerodynamic work is positive for all investigated operating points and increases with increasing backpressure. It is similarly strong with opposite sign to the second half on the suction side.

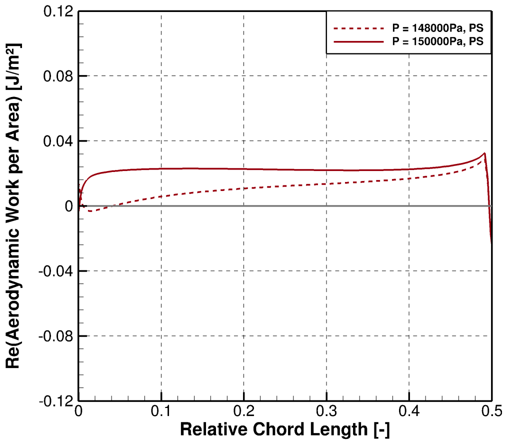

(a) Real part.

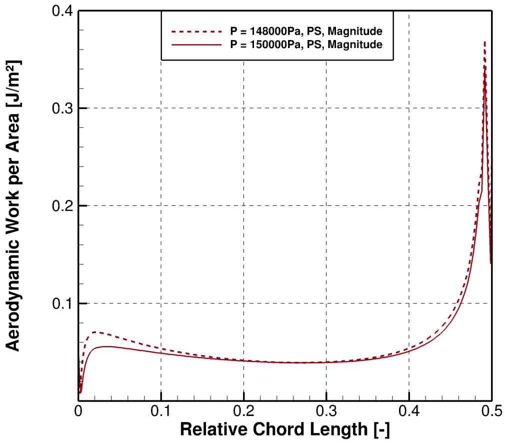

(b) Magnitude.

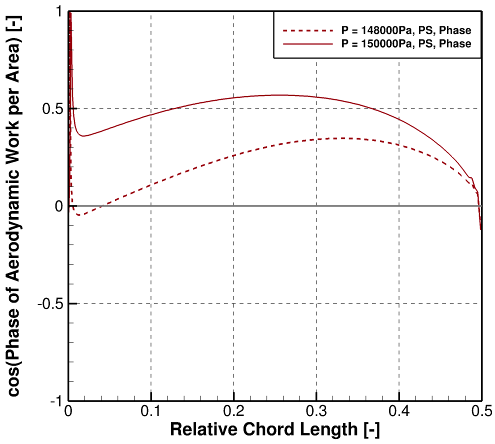

(c) Cosine of phase.

Figure 5.19.: Complex aerodynamic work on the pressure side for RoR 75%, mode 1T, $\sigma_n = +180°$.

Pressure side - First half

The complex aerodynamic work on the pressure side is plotted in figure 5.19. In figures 5.19a, 5.19b and 5.19c the real part, magnitude and cosine of phase are shown respectively.

The magnitude of aerodynamic work has a small local maximum around $2 - 4\,\%$, matching the location of the stagnation point. The magnitude increases for lower backpressures. Following the local maximum, for both operating points, the magnitude decreases until $30\,\%$ RCL. From there, it rises to shortly upstream of the midpoint, where the maximum is reached. The magnitude shows little difference between the operating points.

The cosine of the phase shows sinusoidal behavior over the pressure side, with a local minimum at the stagnation point. For $p_2 = 150000\,\mathrm{Pa}$ the phase over the first half of the pressure side is constantly destabilizing. At the stagnation point, it is around $+0.4$ for $p_2 = 150000\,\mathrm{Pa}$ and 0 for $p_2 = 148000\,\mathrm{Pa}$. For $p_2 = 148000\,\mathrm{Pa}$, the cosine becomes positive downstream of the stagnation point. Overall, the phase is more destabilizing for higher backpressures.

The slightly destabilizing influence of the pressure side for $p_2 = 150000\,\mathrm{Pa}$ compared to the neutral behavior for $p_2 = 148000\,\mathrm{Pa}$ stems from a difference in phase angle. For the torsional mode, the stagnation point influences both the magnitude and phase.

Suction side, first half - Region 1

The complex aerodynamic work in region 1 on the suction side is plotted in figure 5.20, with real part, magnitude and cosine of phase in figures 5.20a, 5.20b and 5.20c respectively.

The magnitude of aerodynamic work over the range if region 1 is similar for both operating points. The difference is a higher magnitude for $p_2 = 148000\,\mathrm{Pa}$ at the leading edge. Around the shock position a strong maximum is present.

For the first 6 % RCL, the phase stays nearly constant, with different values for both operating points. The phase is constantly destabilizing for $p_2 = 150000\,\mathrm{Pa}$ and stabilizing for $p_2 = 148000\,\mathrm{Pa}$ to 7 % RCL. At the shock location, only a small change in phase can be observed, compared to the bending mode. Following the boundary separation and reattachment, the phase increases, having a strong destabilizing influence at the end of region 1.

The difference in flutter stability between both operation points lies in the phase of aerodynamic work. Around the shock, where the magnitude has a maximum, for $p_2 = 148000\,\mathrm{Pa}$ phase phase is stabilizing, while for $p_2 = 150000\,\mathrm{Pa}$ the phase is slightly destabilizing. The influence of the shock - boundary layer interaction is weaker compared to the bending mode.

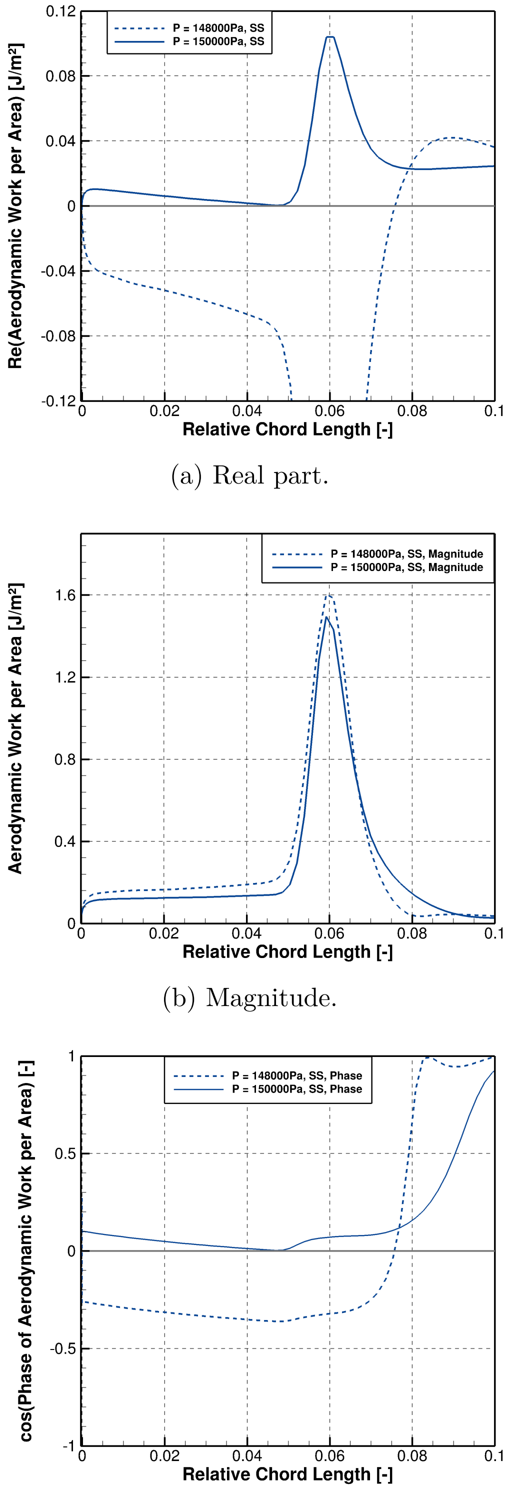

(a) Real part.

(b) Magnitude.

(c) Cosine of phase.

Figure 5.20.: Complex aerodynamic work on the pressure side for RoR 75%, mode 1T, $\sigma_n = +180°$.

Shock - boundary layer interaction

Similar to the bending mode, the suction side is identified as a main driver in flutter instability for increasing backpressures. The shock at 6 % RCL has a strong influence on the magnitude of aerodynamic work, but the influence on the phase is weaker compared to the bending mode. In the following, the position of the shock wave, the interaction with the boundary layer and the influence of the blade oscillation are further investigated.

The RCL of the separation point over one oscillation period is normalized and plotted in figure 5.21a for $p_2 = 149000\,\mathrm{Pa}$, $p_2 = 149500\,\mathrm{Pa}$ and $p_2 = 150000\,\mathrm{Pa}$. The phase shift at the separation point is around 10° for $p_2 = 149000\,\mathrm{Pa}$ and 15° for $p_2 = 149500\,\mathrm{Pa}$ compared to $p_2 = 150000\,\mathrm{Pa}$. This matches the phase shift in unsteady pressure at the separation point around 6 % RCL, as shown in figure 5.20c, where the phase of unsteady pressure is plotted over region 1.
While the phase of unsteady pressure is coupled with the unsteady separation shift over an oscillation period, for the torsion mode this does not seem to have a strong influence on the flutter stability. As depicted in figure 5.20c, the main difference in phase between $p_2 = 148000\,\mathrm{Pa}$ and $p_2 = 150000\,\mathrm{Pa}$ is present from the leading edge on and the increase in phase at the shock is small and also present for $p_2 = 148000\,\mathrm{Pa}$, where the boundary layer stays attached.

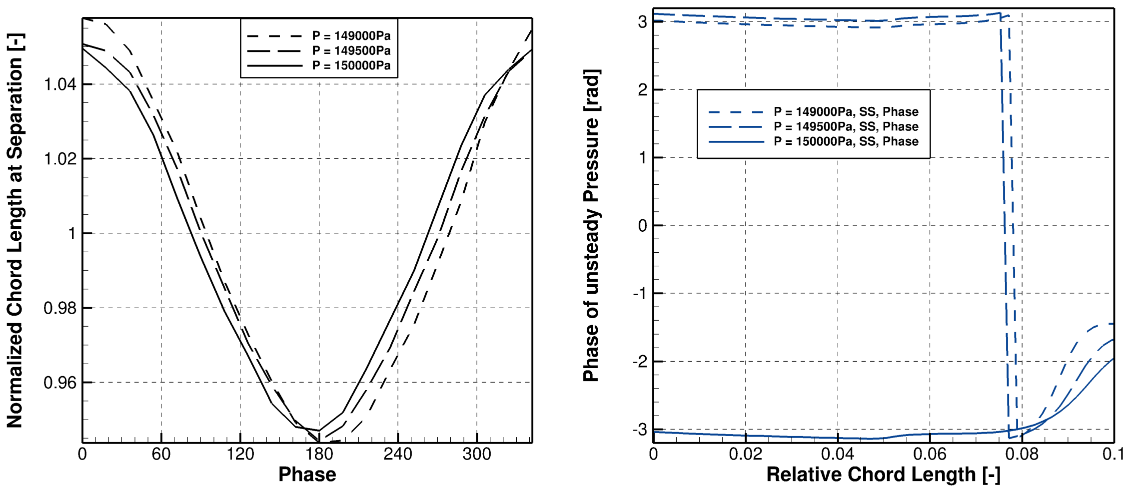

(a) Normalized RCL at separation.

(b) Phase of unsteady pressure.

Figure 5.21.: Normalized RCL at separation and complex aerodynamic work in region 1 on the suction side for RoR 75%, mode 1T, $\sigma_n = +180°$.

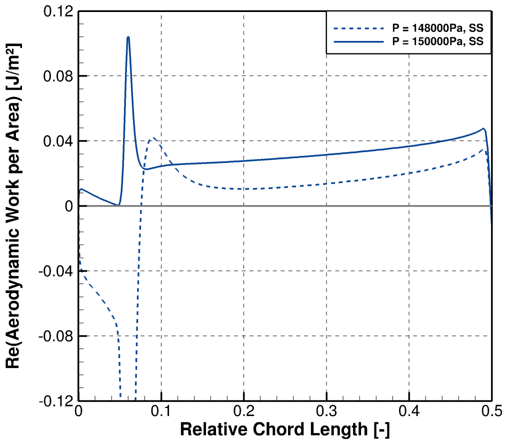

(a) Real part.

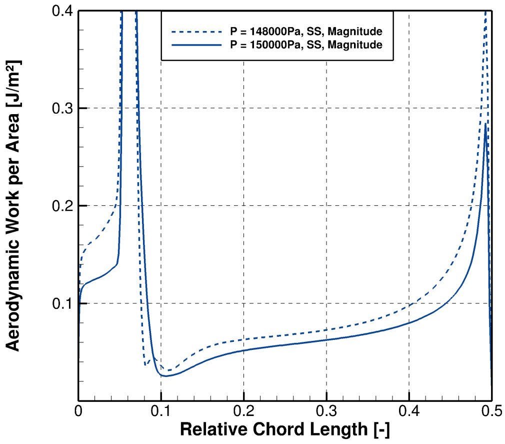

(b) Magnitude.

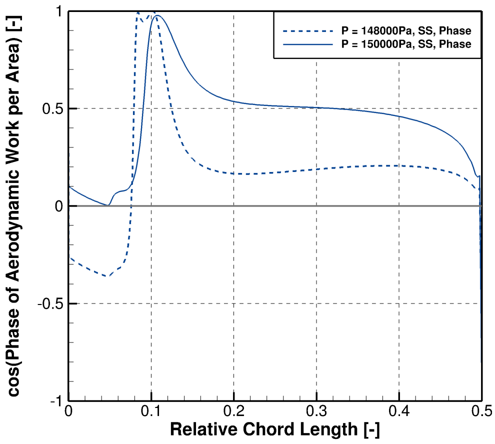

(c) Cosine of phase.

Figure 5.22.: Complex aerodynamic work on the suction side for RoR 75%, mode 1T, $\sigma_n = +180°$.

Suction side, first half - Region 2

Magnitude op aerodynamic work in region 2 on the suction side starts at a minimum at 10 % RCL for both operating points. The magnitude increases downstream and peaks shortly in front of the midpoint, where it drastically falls of. From 10 % RCL onward, magnitude is higher for $p_2 = 148000\,\text{Pa}$ compared to $p_2 = 150000\,\text{Pa}$, but overall, differences in are small for both operating points. This is opposite behavior to the bending mode, where magnitude in aerodynamic work increases for higher backpressures in this region.
At 10 % RCL, the cosine of the phase starts with +1 for both operating points and decreases to +0.2 for $p_2 = 148000\,\text{Pa}$ and +0.5 for $p_2 = 150000\,\text{Pa}$. Near the midpoint it decreases further and changes sign in region 3.

The difference in phase of aerodynamic work for both operating points leads to a more destabilizing influence of region 2 for increasing backpressures, that the higher magnitude for $p_2 = 148000\,\text{Pa}$ can not compensate.

Phase of (re-)attached boundary layer

In figure 5.23, the phase of aerodynamic work is plotted over the relative chord length. Similar to the bending mode, the influence of the shock on the phase shift in region 2 on the suction side diminishes downstream of 12 % RCL. The phase shift from slightly to moderately destabilizing for increasing backpressures is present for operating conditions with and without boundary layer separation, as evident from $p_2 = 147000\,\mathrm{Pa}$ and $p_2 = 148000\,\mathrm{Pa}$. Near the midpoint, for all operating points, a similar behavior is observed. There, the torsion is the dominant mechanism. As for the bending mode, a comparison with operating points on the 55 % speed line is conducted to analyze the behavior of aerodynamic work in region 2 with minimal effect of the shock.

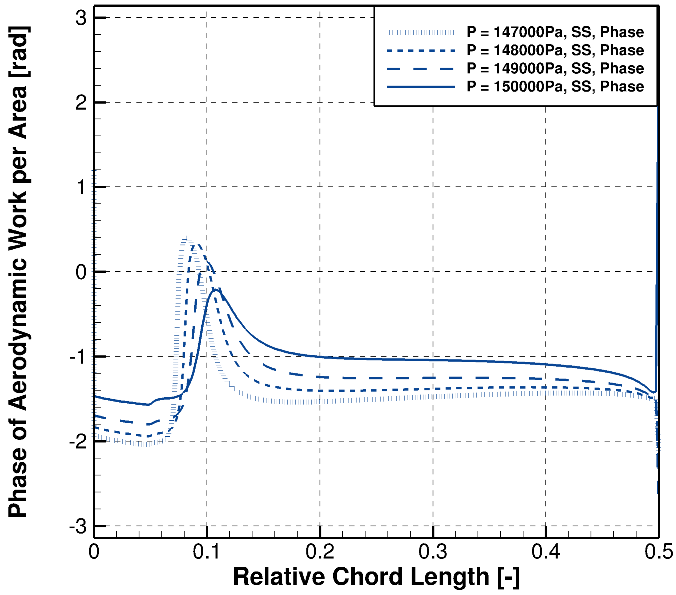

Figure 5.23.: Phase of aerodynamic work for $p_2 = 147000\,\mathrm{Pa}$, $p_2 = 148000\,\mathrm{Pa}$, $p_2 = 149000\,\mathrm{Pa}$ and $p_2 = 150000\,\mathrm{Pa}$, RoR 75%, mode 1T, $\sigma_n = +180°$.

5.2.3.3. Comparison with RoR 55 %

For the comparison of flutter stability effects between the 55 % and 75 % speed lines, operating points between $p_2 = 143000\,\mathrm{Pa}$ and $p_2 = 145000\,\mathrm{Pa}$ are chosen on the 55 % speed line. The decrement of aerodynamic damping is plotted against the IBPA for the investigated operating points in figure 5.24. Comparing figures 5.16 and 5.24, the curves for both speed lines are similar. For increasing backpressure, on both speed lines, the IBPA with lowest aerodynamic damping is $\sigma_n = +180°$. Therefore, this IBPA is chosen for the 55 % speed line for the comparison.

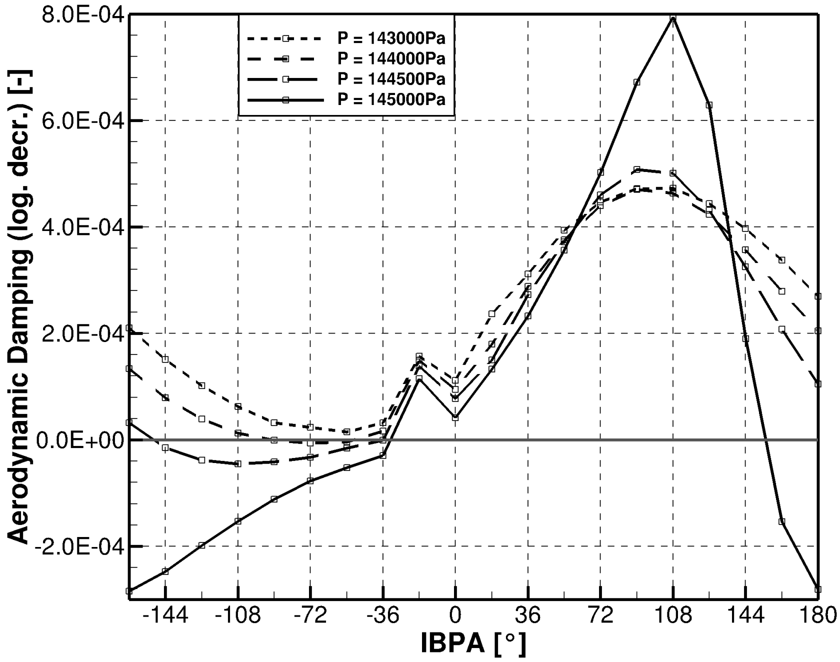

Figure 5.24.: Aerodynamic damping against IBPAs for mode 1T for varying operating points on the 55 % speed line.

The steady-state flow field is given in figure 5.14. The shock is minor compared to operating conditions on the 75 % speed line. The shock is located nearer the leading edge. The boundary layer starts to separate for backpressures between $p_2 = 143000\,\mathrm{Pa}$ and $p_2 = 144000\,\mathrm{Pa}$.

In figure 5.25a, the real part of aerodynamic work for the investigated operating points on the 55 % speed line is plotted over the suction side. Similarly to the 75 % speed line, the region near the leading edge is strongly stabilizing for lower backpressures and becomes destabilizing for increasing backpressures. This is mainly caused by an increase in cosine of aerodynamic work, which is influenced by the shock induced boundary layer separation, as seen in figures 5.25b and 5.25d, where the phase shift is strongest for $p_2 = 145000\,\mathrm{Pa}$ and nonexistent for backpressures lower than 144000 Pa.

Boundary layer separation is the driving mechanism in the phase shift, but it is not necessary for the phase of aerodynamic work to be destabilizing. Similar to the bending mode, shock induced boundary layer separation is present in all investigated cases where flutter occurs. Downstream, the cosine of phase increases for all operating points on the 55 % speed line to about 45 % RCL, where it falls off. Here, the torsion is the dominant mechanism, controlling the phase.

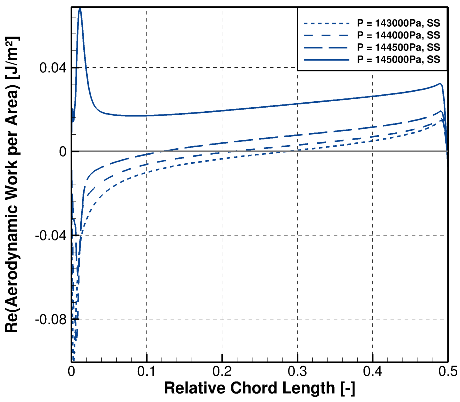

(a) Real part, RoR 55%, mode 1T, $\sigma_n = +180°$.

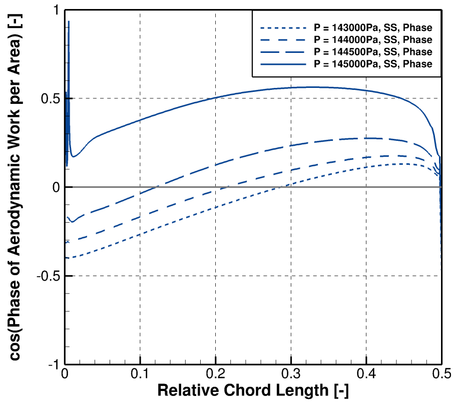

(b) Cosine of phase, RoR 55%, mode 1T, $\sigma_n = +180°$.

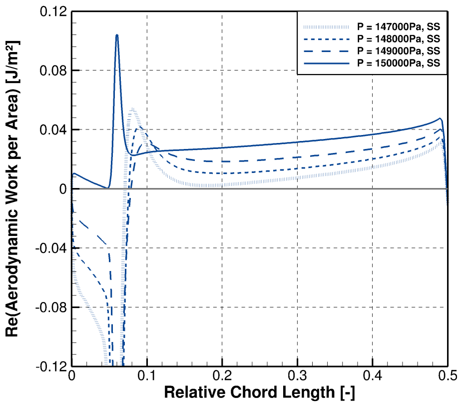

(c) Real part, RoR 75%, mode 1T, $\sigma_n = +180°$.

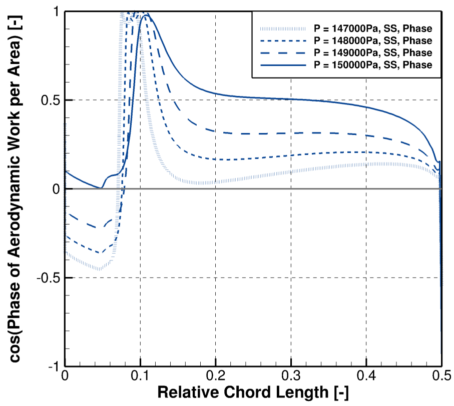

(d) Cosine of phase, RoR 75%, mode 1T, $\sigma_n = +180°$.

Figure 5.25.: Aerodynamic work on the suction side for RoR 55%, mode 1T, $\sigma_n = +180°$ (top) and RoR 75%, mode 1T, $\sigma_n = +180°$ (bottom).

6. Conclusion and Outlook

In this thesis, for a two-dimensional NACA3506 annular compressor cascade

- a mesh sensitivity study was performed for steady-state simulations (non-linear solver) and unsteady flutter simulations (linearized and Harmonic Balance solver);
- a compressor map was created and the flutter stability in the first bending and first torsion mode over the entire working range determined, creating a flutter map;
- unsteady flutter simulations employing the Harmonic Balance solver were conducted to investigate the physical mechanisms regarding stall flutter stability in a transonic flow regime.

Steady-state simulations showed increasing mesh sensitivity for higher rotational speeds and higher pressure ratios. Finer meshes could sustain mass flow for higher backpressures, before the flow stalls. Overall differences in mass flow and pressure ratio were under 1 % between all four tested meshes.
Unsteady flutter simulations showed varying degrees of mesh sensitivity across different operating conditions for both solvers. For some cases, the coarser meshes did not capture the physics accurately. While the two finest meshes produced quantitative different results for flutter stability, their qualitatively prediction was similar.
The second finest mesh G_{+1} with an average cell size of $5 \cdot 10^{-4}$ m was chosen for the calculations for the flutter map and the finest mesh G_{+2} with an average cell size of $2.5 \cdot 10^{-4}$ m was chosen for the investigation of flutter mechanisms. The sensitivity of wall resolution was not investigated. Following findings in the literature, a resolution of $y^+ \approx 0.1$ was used.

The flutter map, created with the linear solver, highlighted flutter instability near the stall and choke line. In the sub- and transonic regimes near stall, flutter in the first torsion mode occurs for lower backpressures compared to the first bending mode. Exceptions are the 100 % and 105 % speed lines in the supersonic regime, where the bending mode becomes unstable earlier. Both are in agreement with the literature. Similar behavior can be observed near the choke line, where torsional flutter occurs nearer the working line. Notably, for the 50 % to 65 % speed lines, the region of torsional flutter extends far in the working range of the compressor.

In the transonic regime near stall, the shock at the suction peak was identified as a key mechanism for flutter onset for both investigated modes. At the shock, the magnitude of aerodynamic work on the blade has a significant maximum. For increasing backpressure, the phase of aerodynamic work shifts to a less stabilizing or more destabilizing behavior. This phase shift is increased by the shock - boundary layer interaction causing flow separation and reattachment. This has a larger impact on the bending mode than on the torsion mode. The influence of the shock on flutter stability is not only local, but extends further downstream.
Other blade sections, such as the region between $20 - 80\,\%$ RCL on the suction side and for the torsion mode, also the first half of the pressure side, have a significant impact on flutter stability with less clear physical mechanisms. However, flutter onset occurs only at operating points, where shock induced boundary layer separation and reattachment appear. This holds true for operating points at lower rotational speeds with weaker shocks and thus less overall impact on flutter stability. This is an important finding for the selection of operating points to determine the flutter boundary of compressor cascades, because the steady-state flow can be used as a first estimation, where the investigation can start. Of course these results must be tested for other geometries and three-dimensional cases to verify the results of this thesis or improve the understanding of flutter mechanisms.

Outlook

The results of this thesis highlight the importance of the steady-state flow field on global flutter stability prediction. While the strength and position of shocks and their interaction with the boundary layer are key information for accurate flutter predictions in transonic flow regimes near stall, this study did not investigate the flutter mechanisms causing choke flutter or flutter instabilities in the supersonic regime. Further studies are needed to identify the mechanisms for flutter onset in other flow regimes.

The influence of blade geometry on flutter stability is a topic that lacks a deeper understanding. Using NACA profiles, the impact of thickness, camber and point of maximum camber on flutter stability and aerodynamic performance can be parametrically studied. In addition, the influence of shocks and shock - boundary layer interactions can be further investigated.

Comparisons with three-dimensional simulations and experiments should be conducted to verify the two-dimensional analysis and identify agreement as well as differences with real world applications of compressor blades. Additionally, three-dimensional effects such as tip vortices or secondary flows and their impact on flutter stability need to be studied.

To produce an analogous work to this thesis for three-dimensional analysis within a reasonable time frame, the existing workflows need to be improved. For this purpose, a detailed mesh sensitivity study, including analysis of y^+ values for the linear and Harmonic Balance solver, needs to be conducted for different operating conditions. An accurate, fast and robust simulation setup must be found.

Bibliography

[1] F. Sisto. *Introduction and Overview in AGARD Manual on Aeroelasticity in Axial-Flow Turbomachines*, volume 1. NATO Advisory Group for Aerospace Research & Development, 1987.

[2] K. Aainsqatsi Wikimedia Commons. *Turbofan operation lbp.* https://upload.wikimedia.org/wikipedia/commons/7/77/Turbofan_operation_lbp.svg, 2008. Online, accessed 21.09.2025, CC BY-SA 4.0.

[3] W.J.G. Bräunling. *Flugzeugtriebwerke*, volume 4. Springer-Verlag Vieweg, 2015.

[4] M. Schuff. *Evaluation of Numerical Modal Analysis with Cyclic Symmetry Boundaries and Complex Mode Shapes due to Structural Coupling in Turbomachinery.* Technical Report, DLR Institute for Aeroelasticity, 2018.

[5] M. Schuff and V. Chenaux. *Nonlinear Aerodynamic Damping in a highly Loaded Vibrating Compressor Cascade.* ASME Turbo Expo 2019: Turbomachinery Technical Conference and Exposition, 2019.

[6] European Commission. *The European Green Deal.* https://ec.europa.eu/commission/presscorner/detail/en/ip_20_17, 2020. Online, accessed 19.10.2025.

[7] D.S. Lee, D.W. Fahey, A. Skowron, M.R. Allen, U. Burkhardt, Q. Chen, S.J. Doherty, S. Freeman, P.M. Forster, J. Fuglestvedt, A. Gettelman, R.R. De León, L.L. Lim, M.T. Lund, R.J. Millar, B. Owen, J.E. Penner, G. Pitari, M.J. Prather, R. Sausen, and L.J. Wilcox. *The contribution of global aviation to anthropogenic climate forcing for 2000 to 2018.* Atmospheric Environment Vol. 244, 2021.

[8] Airports Council International and International Civil Aviation Organization. *Joint ACI World-ICAO Passenger Traffic Report, Trends, and Outlook.* https://aci.aero/2025/01/28/joint-aci-world-icao-passenger-traffic-report-trends-and-outlook/, 2025. Online, accessed 19.10.2025.

[9] W. Wright, O. Wright, and M. McFarland. *The papers of Wilbur and Orville Wright, including the Chanute-Wright letters and other papers of Octave Chanute.* McGraw-Hill Book Company, 1953.

[10] I.E. Garrick and W.H. Reed. *Historical Development of Aircraft Flutter.* AIAA/ASME/ASCE/AHS 22nd Structures, Structural Dynamics and Materials Conference, 1981.

[11] A. Meldahl. *Selbsterregte Flügelschwingungen mit einem Freiheitsgrad.* Brown Boveri Mitteilunge 1946, 1946.

[12] H. Pearson. *The Aerodynamics of Compressor Blade Vibration.* The Engineer, 1953.

[13] F. Sisto. *Stall-Flutter in Cascades.* Flight Propulsion Session, Twenty-First Annual Meeting, 1953.

[14] A.A. Mikolajczak, R.A. Arnoldi, L.E. Snyder, and H. Stargardter. *Advances in Fan and Compressor Blade Flutter Analysis and Predictions.* Journal of Aircraft, 1975.

[15] K. Isomura and M.B. Giles. *A Numerical Study of Flutter in a Transonic Fan.* THE AMERICAN SOCIETY OF MECHANICAL ENG1NEEFtS, 1997.

[16] M. Vahdati, A.I. Sayma, J.G. Mashall, and M. Imregun. *Mechanisms and Prediction Methods for Fan Blade Stall Flutter.* JOURNAL OF PROPULSION AND POWER Vol. 17, 2001.

[17] R. Srivastava, M.A. Bakhle, T.G. Keith, and G.L. Stefko. *FLUTTER ANALYSIS OF A TRANSONIC FAN.* Proceedings of ASME Turbo Expo 2002, 2002.

[18] M. Aotsuka, Y. Horiguchi, and O. Nozaki. *Numerical Simulation of Transonic Fan Flutter with 3D N-S CFD Code.* Proceedings of ASME Turbo Expo 2008, 2008.

[19] X. Dong, Y. Zhang, Y. Zhang, Z. Zhang, and X. Lu. *Numerical simulations of flutter mechanism for high-speed wide-chord transonic fan.* Aerospace Science and Technology, 2020.

[20] X. Duan, J. Cong, Z. Dai, J. Cheng, X. Zhang, and J. Jing. *Influence mechanism and quantificational evaluation of key factors affecting flutter stability of a transonic fan.* Aerospace Science and Technology 138, 2023.

[21] X. Jia, X. Dong, Q. Zhang, Y. Zhang, and X. Lu. *Mechanisms and evolution of flutter stability for a transonic fan under linear reynolds number variations.* Aerospace Science and Technology 168, 2026.

[22] L.E. Snyder and D.W. Burns. *Forced Vibration and Flutter Design Methodology in AGARD Manual on Aeroelasticity in Axial-Flow Turbomachines*, volume 2. NATO Advisory Group for Aerospace Research & Development, 1988.

[23] S. Martin, P. Ferrand, and A. Mazeaux. *A Numerical Study of Mechanisms for Transonic Stall Flutter.* ISUAAAT13, 2012.

[24] M. Vahdati, G. Simpson, and M. Imregun. *Mechanisms for Wide-Chord Fan Blade Flutter.* Journal of Turbomachinery Vol. 133, 2011.

[25] E. Logan Jr. *Handbook of Turbomachinery*, volume 2. Eastern Hemisphere Distribution, 2003.

[26] G.B. Brayton. *Improvement in gas-engines.* United States Patent Office, 1872.

[27] T. Wollmann, N. Modler, M. Dannemann, A. Langkamp, S. Nitschke, and A. Filippatos. *Design and testing of composite compressor blades with focus on the vibration behaviour*, volume 92. Composites Part A: Applied Science and Manufacturing, 2017.

[28] K. Schlichting, H. und Gersten. *Grenzschicht-Theorie*, volume 9. Springer-Verlag Berlin Heidelberg New York, 1997.

[29] P.K. Kundu, I.M. Cohen, and D.R. Dowling. *Fluid Mechanics*, volume 6. Elsevier, 2016.

[30] A.R. Collar. *The Expanding Domain of Aeroelasticity.* The Royal Aeronautical Society, 1946.

[31] F. Lane. *System Mode Shapes in the Flutter of Compressor Blade Rows.* Journal of the Aeronautical Sciences, 1956.

[32] M. Blocher. *Investigations into Rapid Aeroelastic Stability Estimation in Turbomachines for Preliminary Design.* Technical Report, DLR Institute for Aeroelasticity, 2023.

[33] *TRACE User Guide.* https://www.trace-portal.de/userguide/trace/index.html, 2025. Online, accessed 25.06.2025.

[34] W. Sutherland. *The viscosity of gases and molecular force*, volume 5. Philosophical Magazine, 1893.

[35] L.F. Richardson. *Weather Prediction by Numerical Process*, volume 2. Cambridge University Press, 2007.

[36] A.N. Kolmogorov. *Local structure of turbulence in an incompressible fluid at very high Reynolds numbers.* Dokl. Akad. Nauk SSSR., 1941.

[37] J. Boussinesq. *Essai sur la thťeorie des eaux courantes.* Mťemoires prťesentťes par divers savants ‘a lAcadťemie des Sciences XXIII, 1877.

[38] D.C. Wilcox. *Reassessment of the scale-determining equation for advanced turbulence models.* AIAA Journal, Vol. 26, 1988.

[39] H.P. Kersken, G. Ashcroft, and C. Frey. *On the Development of a Harmonic Balance Method for Aeroelatic Analysis.* 11th World Congress on Computational Mechanics, 2014.

[40] H.P. Kersken, C. Frey, C. Voigt, and G. Ashcroft. *Time-Linearized and Time-Accurate 3D RANS Methods for Aeroelastic Analysis in Turbomachinery.* Journal of Turbomachinery Vol. 134, 2012.

[41] W.S. Clark and K.C. Hall. *Numerical Model of the Onset of Stall Flutter in Cascades.* ASME, 1995.

[42] J.G. Marshall and M. Impregun. *A Review of Aeroelasticity Methods with Emphasis on Turbomachinery Applications.* Journal of Fluids and Structures, 1996.

[43] M. Schuff and V. Chenaux. *Coupled Mode Flutter Analysis of Turbomachinery Blades Using an Adaptation of the pk Method.* Journal of Engineering for Gas Turbines and Power, 2021.

[44] F.O. Carta. *Coupled Blade-Disk-Shroud Flutter Instabilities in Turbojet Engine Rotors.* Journal of Engineering for Power, 1967.

[45] A. Weber and M. Sauer. *PyMeshTemplate Documentation.* Technical Report, DLR Institute of Propulsion Technology, 2016.

[46] H. Hennings and J. Belz. *Experimental Investigation of the Aerodynamic Stability of an Annular Compressor Cascade Performing Tuned Pitching Oscillations in Transonic Flow.* ASME 1999 International Gas Turbine and Aeroengine Congress and Exhibition, 1999.

[47] M. Sadeghi and F. Liu. *Investigation of Non-Linear Flutter by a Coupled Aerodynamics and Structural Dynamics Method.* 39th Aerospace Sciences Meeting and Exhibit, Aerospace Sciences Meetings, 2001.

[48] M. Blocher, M. May, and H. Schoenenborn. *Dependency of Unsteady Time-Linearized Flutter Investigations on the Steady State Flow Field.* ASME Turbo Expo 2011, Vancouver, BC, Canada, 2011.

[49] D.C. Wilcox. *Dilatation-dissipation corrections for advanced turbulence models.* AIAA Journal, Vol. 30, 1992.

[50] J. Bardina, J.H. Ferziger, and R.S. Rogallo. *Effect of rotation on isotropic turbulence: computation and modelling*, volume 154. Journal of Fluid Mechanics, 1985.

[51] M. Kato and B. Launder. *The Modelling of Turbulent Flow Around Stationary and Vibrating Square Cylinders.* Proceedings of the 9th Symposium on Turbulent Shear Flow, 1993.

[52] M. Müller, H.P. Kersken, and C. Frey. *A Log-w Turbulence Model Formulation for Flutter Analysis with Harmonic Balance.* 16th International Symposium on Unsteady Aerodynamics, Aeroacoustics & Aeroelasticity of Turbomachines (ISUAAAT16), 2022.

[53] H.P. Kersken, G. Ashcroft, C. Frey, N. Wolfrum, and D. Korte. *onreflecting Boundary Conditions for Aeroelastic Analysis in Time and Frequency Domain 3D RANS Solvers.* ASME Turbo Expo 2014, 2014.

[54] V. Carstens and J. Belz. *Numerical Investigation of Nonlinear Fluid-Structure Interaction in Vibrating Compressor Blades.* Journal of Turbomachinery Vol. 123, 1999.

[55] V. Chenaux, M. Schuff, and D. Quero. *Applicability of Harmonic Balance for the Determination of Blade Stability within the Prescribed Motion Approach.* ASME Turbo Expo 2020: Turbomachinery Technical Conference and Exposition, 2020.

A. Appendix

A.1. Mesh settings

```
#!/usr/bin/env PyMesh.x
template            =                 "Compressor"
input_dir           =                      'input'
output_dir          =                     'output'
######################################################################
###############         Global Settings          ##############
######################################################################
O_TYPE              =                      otype_1
CLEARANCE_h         =                         None
CLEARANCE_t         =                         None
SMOOTHING           =                    smooth_3d
#=====================================================================
#==============            Meta Data             ==============
#=====================================================================
###############             General              ##############
COMPONENT           =                            1
ROW_NUMBER          =                            1
ROW_TYPE            =                rowtype_Rotor
RPM                 =                        153.6
INLET_TYPE          =                    BC_Inflow
EXIT_TYPE           =                   BC_Outflow
###############       Defining Blade Pitch       ##############
NO_BLADES           =                         2000
PITCH               =                       0.0565
###############        Multi Passage Data        ##############
PITCH_NUMBER        =                            1
NO_PITCHES          =                            1
SEGMENT_ANGLE       =                          0.0
SEGMENT_SHIFT       =                          0.0
######################################################################
###############              Input               ##############
######################################################################
#=====================================================================
#==============           S2m settings           ==============
#=====================================================================
S2m_input.file      =                    's2m.dat'
S2m_input.format    =                  fmt_asciiTec
S2m_input.dimI      =                          131
S2m_input.dimK      =                            2
S2m_input.dimK_cl_h =                            0
S2m_input.dimK_cl_t =                            0
S2m_input.I_inlet   =                            1
S2m_input.I_exit    =                          131
S2m_input.scale     =                          1.0
S2m_input.kinks_h   =                           []
S2m_input.kinks_t   =                           []
```

```
#=====================================================================
#==============          BLADE settings          ==============
#=====================================================================
B_input.file        =                 'naca3506.dat'
B_input.format      =                 fmt_asciiTec
B_input.system      =                       cs_XYZ
B_input.dimI        =                          260
B_input.dimK        =                            2
B_input.mirror      =                        False
B_input.iDirOk      =                        False
B_input.iShift      =                            0
B_input.I_LE        =                          131
B_input.scale       =                          1.0
######################################################################
###############    Projection onto HUB and TIP   ##############
######################################################################
Proj_h          =       proj_y ; Proj_t           =       proj_y
np_proj_h       =            0 ; np_proj_t        =            0
#=====================================================================
#==============   CAD data - Sidewall contouring  ==============
#=====================================================================
###############   Files describing HUB geometry  ##############
contourFiles_h      =                         None
###############   Files describing TIP geometry  ##############
contourFiles_t      =                         None
######################################################################
###############         Grid Parameters          ##############
######################################################################
#=====================================================================
#==============    Set Major Block Dimensions    ==============
#=====================================================================
multigrid_factor =           2
O_dimJ          =           49
C_dimJ          =            9
HI_dimI         =           41
HP_dimI         =           65 ; HP_dimJ          =           21
HE_dimI         =           65
np_LE_LS        =            8 ; np_LE_US         =           53
np_OSTE_LS      =           11 ; np_OSTE_US       =            7
np_Offset       =           39
#=====================================================================
#==============       Final blade settings       ==============
#=====================================================================
B_ik_mode       = blademod_newIK
###############        K-wise distribution       ##############
B_k.hRel_is_h   =          0.0 ; B_k.hRel_is_t    =          1.0
B_k.hRel_rm_h   =          0.0 ; B_k.hRel_rm_t    =          0.0
B_k.f_LE_h      =          1.0 ; B_k.f_LE_t       =          1.0
B_k.f_TE_h      =          1.0 ; B_k.f_TE_t       =          1.0
B_k.fit_h       =        False ; B_k.fit_t        =        False
```

```
###############          I-wise distribution          ##############
#..............      Spanwise Reference location      ..............
B_i_h.hRel_ref   =          0.0 ; B_i_t.hRel_ref   =         1.0
B_i_h.np_TE      =          25   ; B_i_t.np_TE      =         25
B_i_h.sr         =          1.4 ; B_i_t.sr         =         1.4
#.............     Relative positions around blade     .............
B_i_h.sRel_TE    =        0.007  ; B_i_t.sRel_TE    =       0.007
B_i_h.sRel_IP_LS =        0.005  ; B_i_t.sRel_IP_LS =       0.005
B_i_h.sRel_IP_US =        0.36   ; B_i_t.sRel_IP_US =       0.36
B_i_h.sRel_OS    =        0.3    ; B_i_t.sRel_OS    =       0.3
#.............          first/last Distances          .............
B_i_h.d_TE       =       0.0005  ; B_i_t.d_TE       =      0.0005
B_i_h.d_LE       =       0.00032 ; B_i_t.d_LE       =      0.00032
B_i_h.d_IP_LS    =       0.0     ; B_i_t.d_IP_LS    =      0.0
B_i_h.d_IP_US    =       0.006   ; B_i_t.d_IP_US    =      0.006
B_i_h.d_OS       =       0.01    ; B_i_t.d_OS       =      0.01
#........... Point distribution for main part of blade ...........
B_i_h.FactS_P_LS =         0.38 ; B_i_t.FactS_P_LS =        0.38
B_i_h.FactS_I_US =         0.45 ; B_i_t.FactS_I_US =        0.45
B_i_h.FactS_P_US =         0.45 ; B_i_t.FactS_P_US =        0.45
#......... FILLET root adaption - shift points at k=1/O_dimK ........
B_i_h.sShift_LELS=          0.0 ; B_i_t.sShift_LELS=         0.0
B_i_h.sShift_LEUS=          0.0 ; B_i_t.sShift_LEUS=         0.0
B_i_h.sShift_TELS=          0.0 ; B_i_t.sShift_TELS=         0.0
B_i_h.sShift_TEUS=          0.0 ; B_i_t.sShift_TEUS=         0.0
#.............          Clearance resolution          .............
B_i_h.cl_np_LE   =            0 ; B_i_t.cl_np_LE   =           0
B_i_h.cl_np_TE   =            0 ; B_i_t.cl_np_TE   =           0
B_i_h.cl_sRel_LE =          0.0 ; B_i_t.cl_sRel_LE =         0.0
B_i_h.cl_sRel_TE =          0.0 ; B_i_t.cl_sRel_TE =         0.0
B_i_h.cl_d_LE    =          0.0 ; B_i_t.cl_d_LE    =         0.0
B_i_h.cl_d_TE    =          0.0 ; B_i_t.cl_d_TE    =         0.0
#====================================================================
#==============        O-Block: S1 Parameters        ==============
#====================================================================
O_h.r_LE         =       0.0475; O_t.r_LE         =       0.0475
O_h.r_TE         =       0.0475; O_t.r_TE         =       0.0475
O_h.f_TE_red     =          1.0 ; O_t.f_TE_red     =         1.0
O_h.sr_LE        =         1.20 ; O_t.sr_LE        =        1.20
O_h.sr_TE        =         1.20 ; O_t.sr_TE        =        1.20
#====================================================================
#==============        C-Block: S1 Parameters        ==============
#====================================================================
C_h.r_TELS       =        0.08  ; C_t.r_TELS       =       0.08
C_h.r_LE         =        0.085 ; C_t.r_LE         =       0.085
C_h.r_TEUS       =        0.08  ; C_t.r_TEUS       =       0.08
C_h.sShift_TELS  =       -0.075 ; C_t.sShift_TELS  =      -0.075
C_h.sShift_TEUS  =        0.175 ; C_t.sShift_TEUS  =       0.175
C_h.f_TELS       =         0.8  ; C_t.f_TELS       =        0.8
C_h.f_OS         =         1.25 ; C_t.f_OS         =        1.25
C_h.f_TEUS       =         1.1  ; C_t.f_TEUS       =        1.1
C_h.f_IP_LS      =         1.25 ; C_t.f_IP_LS      =        1.25
C_h.f_IP_US      =         1.2  ; C_t.f_IP_US      =        1.2
C_h.f_redj_TELS  =         0.75 ; C_t.f_redj_TELS  =        0.75
C_h.wf_HI        =          0.5 ; C_t.wf_HI        =         0.5
#====================================================================
#==============    Passage H-Block: S1 Parameters    ==============
#====================================================================
HP_h.sr_iMin     =          1.6 ; HP_t.sr_iMin     =         1.6
HP_h.sr_iMax     =         1.05; HP_t.sr_iMax     =         1.05
```

```
#====================================================================
#==============     Inlet H-Block : S1 Parameters     ==============
#====================================================================
HI_h.I_SD        =       15     ; HI_t.I_SD        =       15
HI_h.sRel_SD     =        0.45  ; HI_t.sRel_SD     =        0.45
HI_h.zShift      =       -0.1   ; HI_t.zShift      =       -0.1
HI_h.zShift_IF   =        0.0   ; HI_t.zShift_IF   =        0.0
HI_h.alfa_iSD    =        0.0   ; HI_t.alfa_iSD    =        0.0
HI_h.alfa_iMax   =       40.0   ; HI_t.alfa_iMax   =       40.0
HI_h.wf_DistOne  =        0.9   ; HI_t.wf_DistOne  =        0.9
HI_h.d_iSD       =        0.044 ; HI_t.d_iSD       =        0.044
HI_h.dAlfa_iMaxC =        0.0   ; HI_t.dAlfa_iMaxC =        0.0
HI_h.zRel_iSDC   =        0.5   ; HI_t.zRel_iSDC   =        0.5
HI_h.match_j     = matchj_equi ; HI_t.match_j     = matchj_equi
HI_h.Shape       =         0.15 ; HI_t.Shape       =         0.15
#====================================================================
#==============      Exit H-Block: S1 Parameters      ==============
#====================================================================
HE_h.I_SD        =       36     ; HE_t.I_SD        =       36
HE_h.sRel_SD     =        0.4   ; HE_t.sRel_SD     =        0.4
HE_h.zShift      =        0.0   ; HE_t.zShift      =        0.0
HE_h.zShift_OF   =        0.0   ; HE_t.zShift_OF   =        0.0
HE_h.alfa_iMin   =        0.0   ; HE_t.alfa_iMin   =        0.0
HE_h.alfa_iSD    =        0.0   ; HE_t.alfa_iSD    =        0.0
HE_h.wf_DistOne  =        0.9   ; HE_t.wf_DistOne  =        0.9
HE_h.d_iSD       =        0.03  ; HE_t.d_iSD       =        0.03
HE_h.zRel_jw1    =        0.085 ; HE_t.zRel_jw1    =        0.085
HE_h.zRel_jw2    =        0.30  ; HE_t.zRel_jw2    =        0.30
HE_h.dAlfa_jw1   =          0.0 ; HE_t.dAlfa_jw1   =          0.0
HE_h.dAlfa_jw2   =          0.0 ; HE_t.dAlfa_jw2   =          0.0
HE_h.dAlfa_jOS   =          0.0 ; HE_t.dAlfa_jOS   =          0.0
HE_h.match_j     = matchj_equi ; HE_t.match_j     = matchj_equi
HE_h.Shape       =         0.15 ; HE_t.Shape       =         0.15
#=====================================================================
#=== Parameters for Simple fillet outer O-block correction (OTYPE = 1) ===
#=====================================================================
hRel_Fillet_h    =          0.0 ; hRel_Fillet_t    =          1.0
#=====================================================================
#================ Parameters for Exact fillet (OTYPE = 2) ==============
#=====================================================================
O2_h.hRel_LELS   =          0.0 ; O2_t.hRel_LELS   =          0.0
O2_h.hRel_LEUS   =          0.0 ; O2_t.hRel_LEUS   =          0.0
O2_h.hRel_TELS   =          0.0 ; O2_t.hRel_TELS   =          0.0
O2_h.hRel_TEUS   =          0.0 ; O2_t.hRel_TEUS   =          0.0
#=====================================================================
#============== Parameters for building 3D Clearance blocks ============
#=====================================================================
#################    Settings for H2-type Clearance    ###############
Cl_H2_h.set1To1  =        False ; Cl_H2_t.set1To1  =        False
Cl_H2_h.dimJ     =            0 ; Cl_H2_t.dimJ     =            0
Cl_H2_h.sRel_LE  =          0.0 ; Cl_H2_t.sRel_LE  =          0.0
Cl_H2_h.sRel_TE  =          0.0 ; Cl_H2_t.sRel_TE  =          0.0
#################    Settings for OH-type Clearance    ###############
Cl_OH_h.set1To1  =        False ; Cl_OH_t.set1To1  =        False
Cl_OH_h.O_dimJ   =            0 ; Cl_OH_t.O_dimJ   =            0
Cl_OH_h.H_dimJ   =            0 ; Cl_OH_t.H_dimJ   =            0
Cl_OH_h.V_pos    =         None ; Cl_OH_t.V_pos    =         None
Cl_OH_h.V_red    =         None ; Cl_OH_t.V_red    =         None
```

Table A.1.: Grid refinement levels and mesh properties

Refinement Level	G_{-1}	G_0	G_{+1}	G_{+2}
Total Cell Count	8992	23568	71280	273804
		O-Grid		
First Cell Height		$1.2 \cdot 10^{-7}$ m		
Expansion Ratio	1.20	1.20	1.20	1.10
Total Thickness		$3.7 \cdot 10^{-3}$ m		
Last Cell Height	$6.0 \cdot 10^{-4}$ m	$6.0 \cdot 10^{-4}$ m	$6.0 \cdot 10^{-4}$ m	$3.1 \cdot 10^{-4}$ m
Number of Layers	48	48	48	84
Dim I	123	241	483	967
Cell Count	5904	11568	23184	81228
		C-Grid		
First Cell Height	$8.8 \cdot 10^{-4}$ m	$6.6 \cdot 10^{-4}$ m	$5.8 \cdot 10^{-4}$ m	$2.8 \cdot 10^{-4}$ m
Average Cell Size	$2.0 \cdot 10^{-3}$ m	$1.0 \cdot 10^{-3}$ m	$5.0 \cdot 10^{-4}$ m	$2.5 \cdot 10^{-4}$ m
Dim I	113	225	451	903
Dim J	4	8	16	32
Cell Count	452	1800	7216	28896
		H-Inlet		
Dim I	20	40	80	160
Dim J	39	79	159	319
Cell Count	780	3160	12720	51040
		H-Passage		
Dim I	32	64	128	256
Dim J	10	20	40	80
Cell Count	320	1280	5120	20480
		H-Outlet		
Dim I	32	64	128	256
Dim J	48	90	180	360
Cell Count	1536	5760	23040	92160

A.2. Mesh pictures

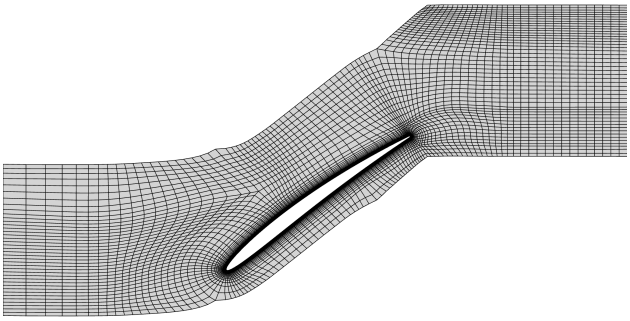

(a) Coarse mesh, G_{-1}.

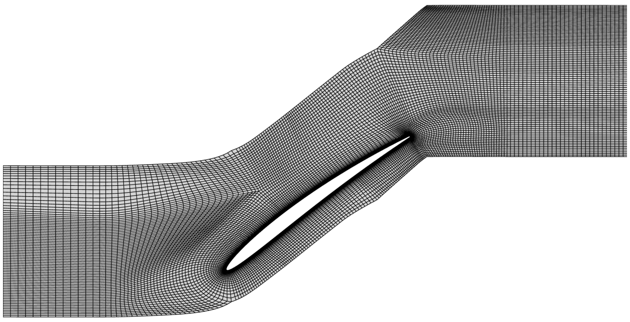

(b) Base mesh, G_0.

(c) Fine mesh, G_{+1}.

(d) Very fine mesh, G_{+2}.

Figure A.1.: Overview of meshes G_{-1}, G_0, G_{+1} and G_{+2}.

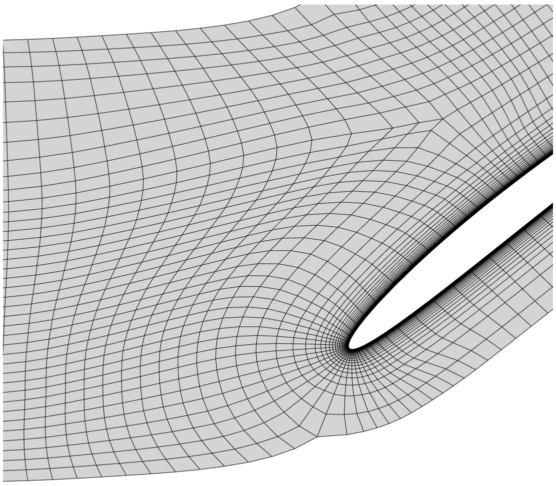

(a) Coarse mesh, G_{-1}.

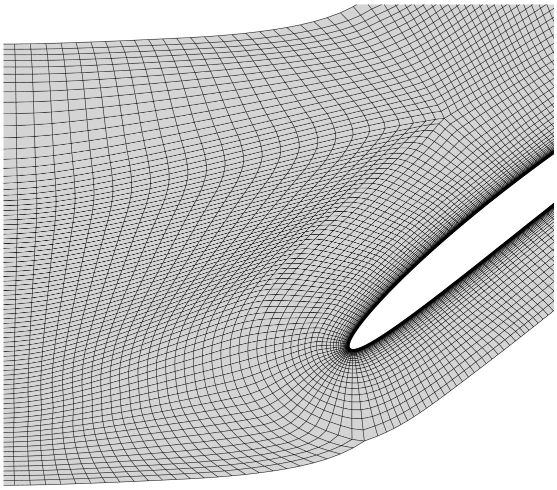

(b) Base mesh, G_0.

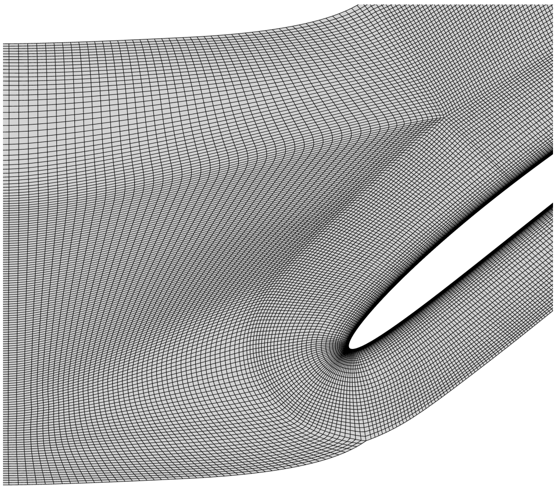

(c) Fine mesh, G_{+1}.

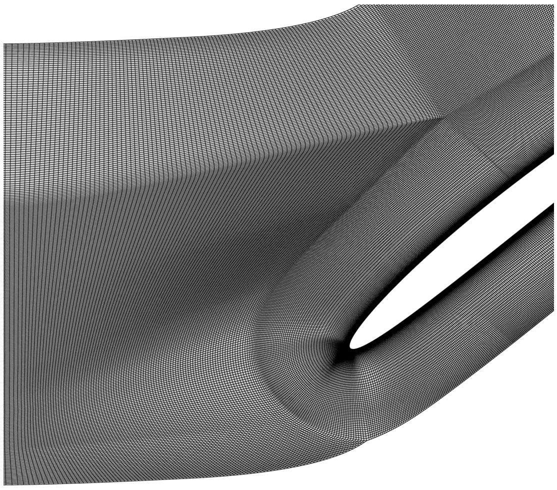

(d) Very fine mesh, G_{+2}.

Figure A.2.: Meshes around leading edges.

A.3. TRACE setup

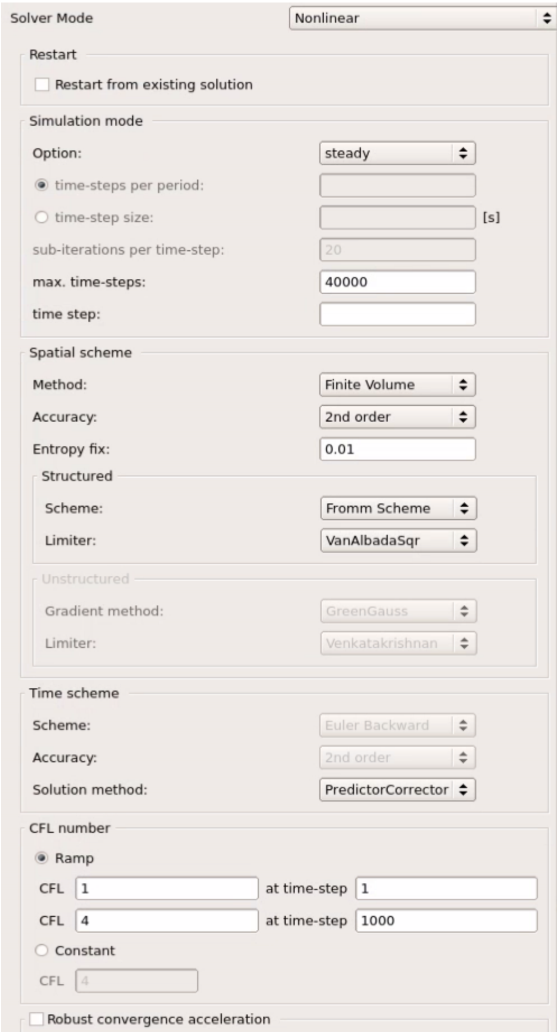

(a) Solver settings.

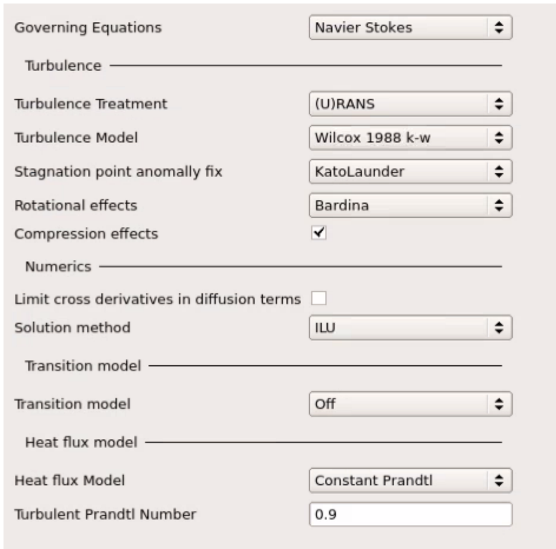

(b) Equation settings.

Figure A.3.: Solver settings of the steady-state solver.

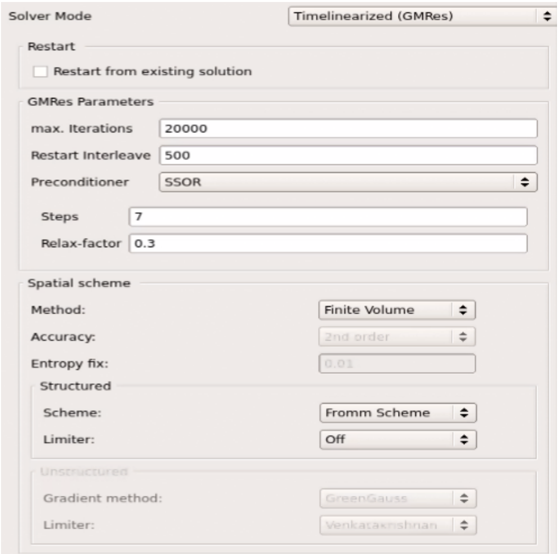

(a) Solver settings.

(b) Equation settings.

Figure A.4.: Solver settings of the linearized solver.

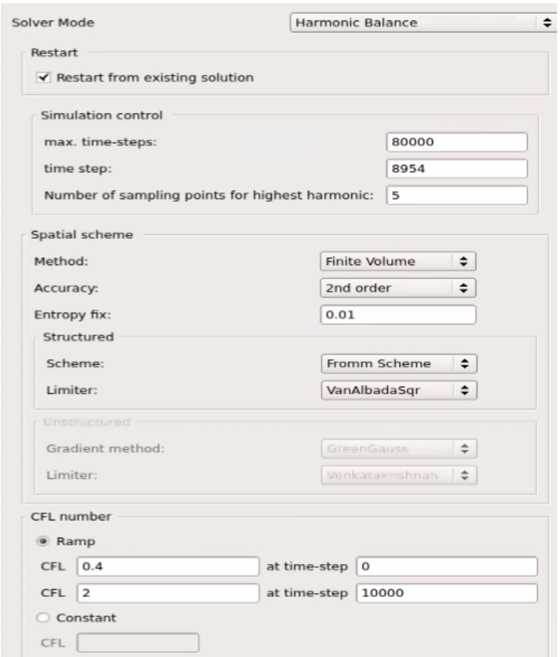

(a) Solver settings.

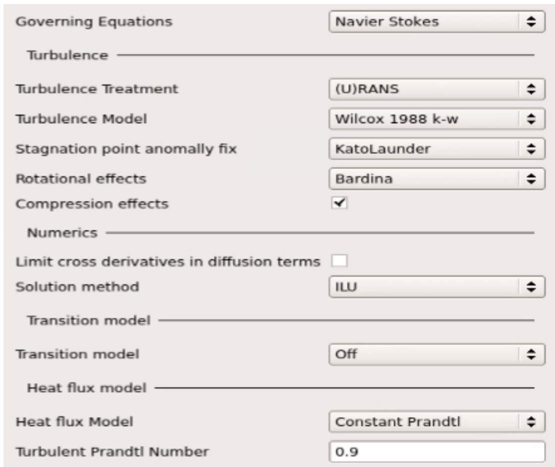

(b) Equation settings.

Figure A.5.: Solver settings of the Harmonic Balance solver.

A.4. Mesh sensitivity study

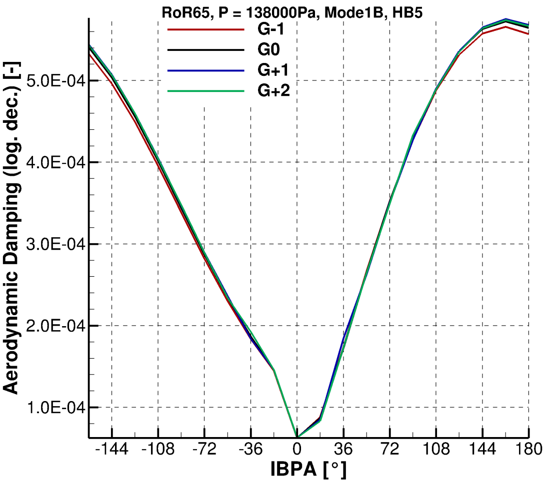

(a) Mode 1B, HB5 solver.

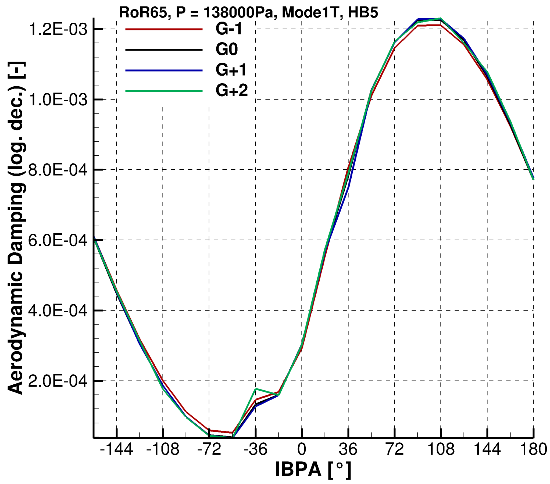

(b) Mode 1T, HB5 solver.

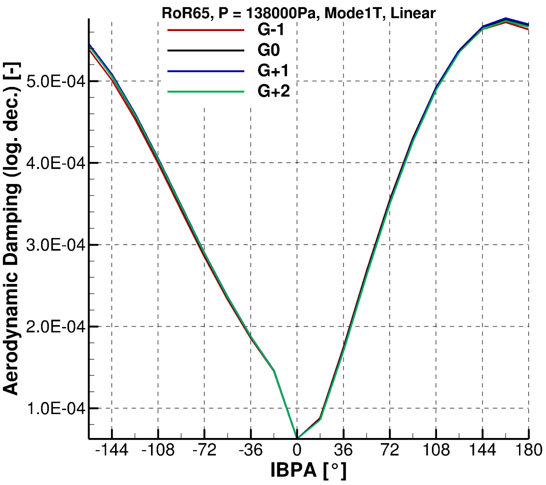

(c) Mode 1B, linear solver.

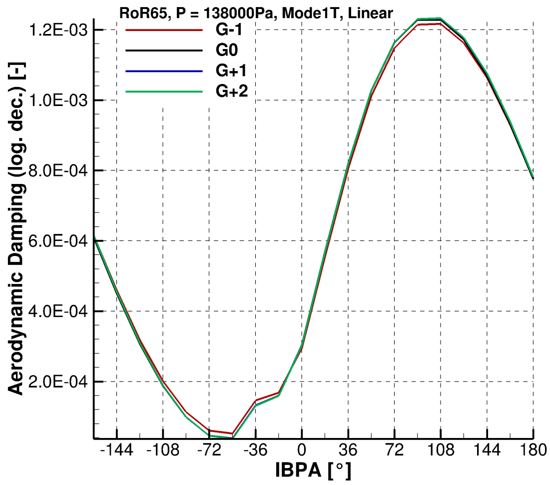

(d) Mode 1T, linear solver.

Figure A.6.: Mesh sensitivity of aerodynamic damping for unsteady flutter simulations; RoR 65 %, $p_2 = 138000\,\mathrm{Pa}$.

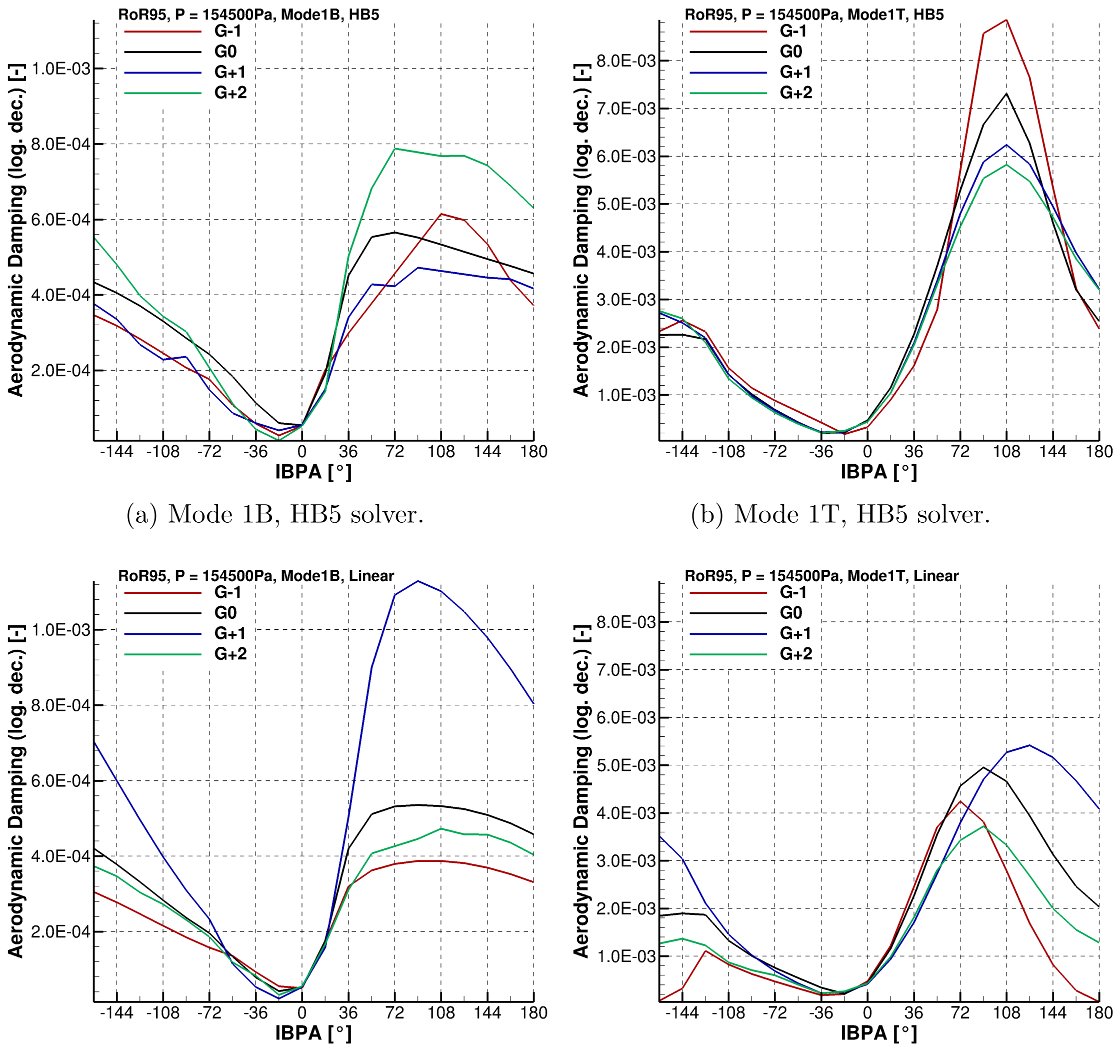

(a) Mode 1B, HB5 solver.

(b) Mode 1T, HB5 solver.

(c) Mode 1B, linear solver.

(d) Mode 1T, linear solver.

Figure A.7.: Mesh sensitivity of aerodynamic damping for unsteady flutter simulations; RoR 95 %, $p_2 = 154500\,\mathrm{Pa}$.

Erklärung Ich versichere hiermit, dass ich die vorliegende Arbeit ohne fremde Hilfe selbstständig verfasst und nur die von mir angegebenen Quellen und Hilfsmittel verwendet habe. Wörtlich oder sinngemäß aus anderen Werken entnommene Stellen habe ich unter Angabe der Quellen kenntlich gemacht. Die Richtlinien zur Sicherung der guten wissenschaftlichen Praxis an der Universität Göttingen wurden von mir beachtet. Eine gegebenenfalls eingereichte digitale Version stimmt mit der schriftlichen Fassung überein. Mir ist bewusst, dass bei Verstoß gegen diese Grundsätze die Prüfung mit nicht bestanden bewertet wird.

Göttingen, den 11. März 2026

(Florian Resech)